VEX-VMC-MPS Experimenter To Guest Storage Facility Data Deriviation and Interface Control Document for Near Infrared 2 Nightside Re-Calibrated Images and Sgmented map of relative Venus surface emissivity

prepared by Dr. E. Shalygin, Dr. O. Shalygina, and Dr. A.G. Straume

May 13, 2025

Table 1.: Document change record

Date	Document No., Issue	Affected Pages	Reason for change
13-May-2025	EGSF-DDICD, Issue 001	All	Initial version

Contents

1. Introduction

1.1. Purpose and scope

EGSF-DDICD-VEX-VMC-MPS-NIR2-NS-RCI-EMI_SGMNT document (Experimenter to Guest Storage Facility (EGSF) Data Derivation and Interface Control Document (DDICD) Venus Express (VEX), Venus Monitoring Camera (VMC), Max Planck Institute for Solar System Research (MPS), Near Infrared 2 (NIR2), Nightside (NS), Re-Calibrated Images (RCI), and segmented map (SGMNT) of relative Venus surface emissivity (EMI)) is the official interface between the VMC team and the Guest Storage Facility. It is related to the updated VMC nightside data and retrieved emissivity map stored on [7], and supplements the information about the data archive format (see VEX-VMC-MPS-NIR2-NS-RCI-EMI_SGMNT-GSF-PUG [30]) with the scientific details of the data derivation and describes the data format (*e.g.* image metadata).

For the convenience of the data user, to have all important information regarding the data format in one place, the Appendix sections of this document (chapter A, chapter B and chapter C) contain useful information about the VMC camera, data handling, metadata, *etc.* copied from VEX-VMC To Planetary Science Archive Interface Control Document (EAICD) [24] while preserving the structure of the original document.

1.2. Archiving Authorities

The Guest Storage Facility [7], developed in 2019 by ESA PSA, is an FTP file repository into which scientists from the planetary community can upload and share scientific products valuable for the community.

1.3. Intended Readership

The staff of the archiving authority (Planetary Science Archive, ESA, RSSD, design team) and any potential user of the VMC data.

1.4. Applicable Documents

- VEX-VMC-MPS-NIR2-NS-RCI-EMI_SGMNT-GSF-PUG [30]
- Experimenter to (Science) Archive Interface Control Document (EAICD) [24]
- VenusExpress - VMC Data Products Naming Convention [27]
- VenusExpress - VMC Level-1 Product Description [25]
- VenusExpress - VMC Level-2 Product Description [26]
- PDS3 Standards Reference [20]
- Planetary Science Data Dictionary [23]

1.5. Acronyms

Akatsuki *Akatsuki.* 7

EnVision *EnVision.* 7

MGN *Magellan Venus Radar Mapping Mission.* 7

AFF additional flat field. 11, 13, 15, 20, 24, 27, 31, 44, 48, 55

CCD A Charge-Coupled Device. 11

CDSD Carbon Dioxide Spectroscopic Database. 66

CoI Co-Investigator. 75, 78

DLR Deutsches Zentrum für Luft- und Raumfahrt (German Aerospace Center). 73, 75, 76, 81

ESA European Space Agency. 6, 76

ESOC European Space Operation Center. 75

ESTEC European Space Research and Technology Center. 76, 78

FoV field of view. 13

GSF Guest Storage Facility. 7, 50, 71

HITRAN high-resolution transmission molecular absorption database. 66

IDA Institute of Computer and Communication Network Engineering, Braunschweig, Germany. 75

JPL NASA Jet Propulsion Laboratory. 73

MPS Max-Planck-Institute for Solar System Research, Göttingen. 6

NIR Near Infra-red. 7, 66

PDS Planetary Data System. 75, 76

PI Principal Investigator. 75, 78

PSA Planetary Science Archive. 11, 75, 76, 79

PVV PSA Volume Verifier. 78, 79

RT radiative transfer. 66

SNR signal-to-noise ratio. 66

VEx *Venus Express.* 7, 8, 11, 13, 48, 65

VICAR Video Image Communication and Retrieval. 73, 75, 76, 83, 84

VIRA Venus International Reference Atmosphere. 68

VIRTIS Visible and Infra-Red Infra-Red Thermal Imaging Spectrometer. 7, 8, 66

VMC Venus Monitoring Camera. 3, 7, 8, 11, 12, 13, 14, 17, 19, 23, 26, 27, 48, 50, 56, 62, 63, 64, 65, 66, 67, 68, 69, 73, 74, 75, 76, 77, 79, 80, 81, 82, 83, 84, 90

1.6. Contact Names and Addresses

Eugene Shalygin (eugene.shalygin@gmail.com), Oksana Shalygina (o.s.shalygina@gmail.com), MPS
Anne Grete Straume (Anne.Straume@esa.int), ESA

2. Additional level of re-calibrated NIR2 surface images

For the surface images taken in the NIR2 filter (n22 filename suffix) an additional processing level is available. These data are obtained from data level 2 images (VMC data archive) applying a procedure to compensate for incorrect additional flat-fielding done in level 2.

All source images for this level were processed by DLR, and the information suitable for previous levels of processing is actual for the current data set.

New images that make up the VEX-V-VMC-3-RDR-SCP-V1.0 dataset are stored in Guest Storage Facility (GSF). The format of the retrieved data is described in [30].

2.1. Scientific background and motivation

Venus and Earth are thought to have formed in similar environments, but divergent evolutionary paths lead to extreme differences in conditions on these sister planets. Why and how did these planet-twins become “antipodes”? This question is one of the most fundamental in planetary science [1]. Evolution of planetary interiors and atmospheric conditions leave footprints on planetary surfaces. Conventional imaging of the Venus surface is hindered by the thick atmosphere and clouds. They block radiation emitted by the surface almost in the entire electromagnetic spectrum, leaving only radio and microwave ranges in which the atmosphere is completely transparent, and several narrow spectral transparency “windows” in the Near Infra-red (NIR) range, where atmospheric absorption is weak and radiation from the surface can leak to space. The NIR thermal emission bears information about the surface temperature and mineralogical composition of the top few hundreds of microns of the surface that are subject to strong changes due to evolutionary processes, e.g. weathering, cratering, etc. The emission measured from orbit also depends on the atmospheric properties and, in particular, cloud opacity.

2.1.1. Updating VMC data

The *Venus Express* (VEx) spacecraft [35] that operated in orbit around Venus from 2006 through 2014 carried two instruments capable of imaging in the NIR: the Visible and Infra-Red Infra-Red Thermal Imaging Spectrometer (VIRTIS) (Piccioni et al., 2006) and the VMC [15] (see fig. 2.1 and chapter A). Together they provided the first systematic thermal mapping of the Venus surface from orbit. VIRTIS mapped the southern hemisphere while VMC observed equatorial regions and the northern hemisphere fig. 2.2 thus delivering complimentary data sets. Spatial resolution on the surface of such observations is limited by the blurring effect of the atmosphere and is not better than $50\,\mathrm{km\,pix}^{-1}$.

VMC captured around 10,000 images of the Venus night side thus having delivered the most extensive data set to date. The first analysis focused on retrieval of the surface and atmospheric properties from individual orbits (*e.g.* [3, 32, 31]). This analysis led to the discovery of ongoing volcanic activity event on Venus in the Ganis Chasma. However, not all VMC data were used in those works due to calibration issues related to the detector damage during the cruise phase [33, 37]. So, it was realised that further refinement of the calibration is necessary in order to make the whole VMC surface data set suitable for photometric studies.

The gained experience in the image processing and analysis allowed us to create a high-level data set of relative surface emissivity, which would be complimentary to already published *Magellan Venus Radar Mapping Mission* (*MGN*) and VIRTIS data sets, and *Akatsuki* (*Akatsuki*) data and *EnVision* (*EnVision*) mission in the near future. The derived map of relative surface emissivity at $1\,\mu\mathrm{m}$ and its variance may be used for scientific analysis. The statistical component of the map would allow determination of significance level of the emissivity variations. Spatial distribution of these properties across geological units would provide insights in their mineralogical composition, evolution of the interiors (via properties of the extruded material), weathering processes, dust distribution and transport, and to identify possible active volcanic events. The topmost surface layer which is observable in the near-IR range is expected to evolve quickly enough due to chemical weathering. Thus the VMC emissivity map could also be used as a reference for comparison with future observations. This would prepare the VMC surface data for the comprehensive usage by the scientific community.

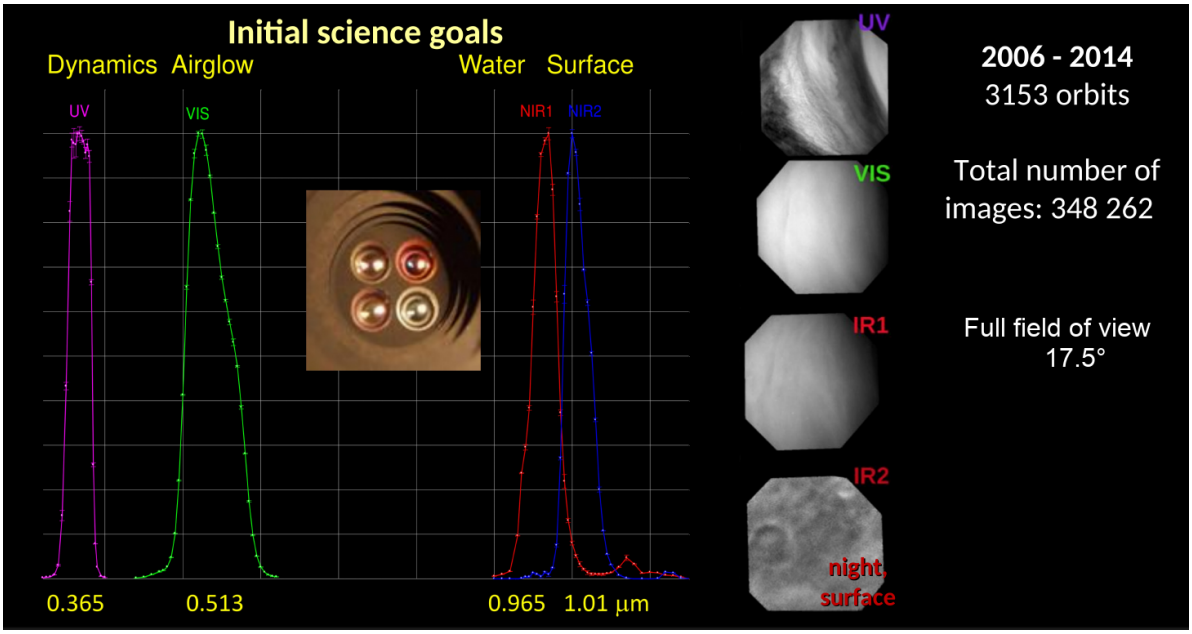

Figure 2.1.: Venus Monitoring Camera

2.1.2. VMC calibration

Radiometric calibration, focus and distortion tests have been performed in a laboratory as described in *VMC calibration report* [39]. During this calibration, sensitivity of the camera at various temperatures and exposures have been determined using integrating sphere. Unfortunately, all the images in NIR2 channel with $\sim$ 4 s and more exposures were saturated (signal level was more then 9300 DN). Thus, there is no reliable radiometric calibration for the night-side observations (30 s exposures).

In-flight recalibration of the VMC using stars has been performed by Ignatiev [12, 12] and Titov et al. [37] and updated in November, 2012 [13]. However, sensitivity of the NIR2 channels is not high enough to get precise enough results. Cross-calibration with VIRTIS also has been done by Ignatiev [13]. Unfortunately, there are no much overlapping between VMC and VIRTIS coverage. Re-calibration coefficients, obtained by these methods for NIR2 filter and 30 s exposures differ: $3.0(15)$ via stars method and $1.73(1)$ via comparison with VIRTIS-M (night-side).

Taking into account all the above, one can say that radiometric calibration of the VMC for night-side observations is rather uncertain. Because of that, this work does not rely on absolute calibration of the instrument, except for the time stability of the instrument response. All night-side images are taken with the same exposure of 30 s and at almost the same temperatures. This makes the calibration for night-side data self-consistent, even if it is not correct.

2.1.2.1. Additional Flat Fields problems

During the cruise phase, the camera, which does not have a shutter, was exposed to the direct Sun illumination for more then 500 h. With the start of the observations, it was discovered that there are numerous complicated artefacts in the field of view (fig. 2.7). Because of the intensive illumination, material of micro-lenses on top of the CCD was damaged and that resulted into appearance of a dark strip in UV (fig. 2.7a), and complicated irregular dark and bright features in all channels (figs. 2.7a and 2.7b). The dark strip is believed to be caused by yellowing of the micro-lenses, and it stays at the same position. The artefacts of the other kind are not stable but evolving and moving with the time scale of several days. Additional flat-fielding is used to remove these artefacts. As a source for flat-fields, images of clouds near the north pole are used. Images, taken from close distance, are featureless. However, if the plane of VEx orbit is close to the terminator plane, large brightness gradient is present. The linear part of this gradient is removed by fitting a plane to the brightness field. Since artefacts of the second kind change not significantly during one day, it is possible to use such flat-fields. When it is not possible to take images of the cloud near the pericentre, or when these images contain features, images from another neighbour orbit are

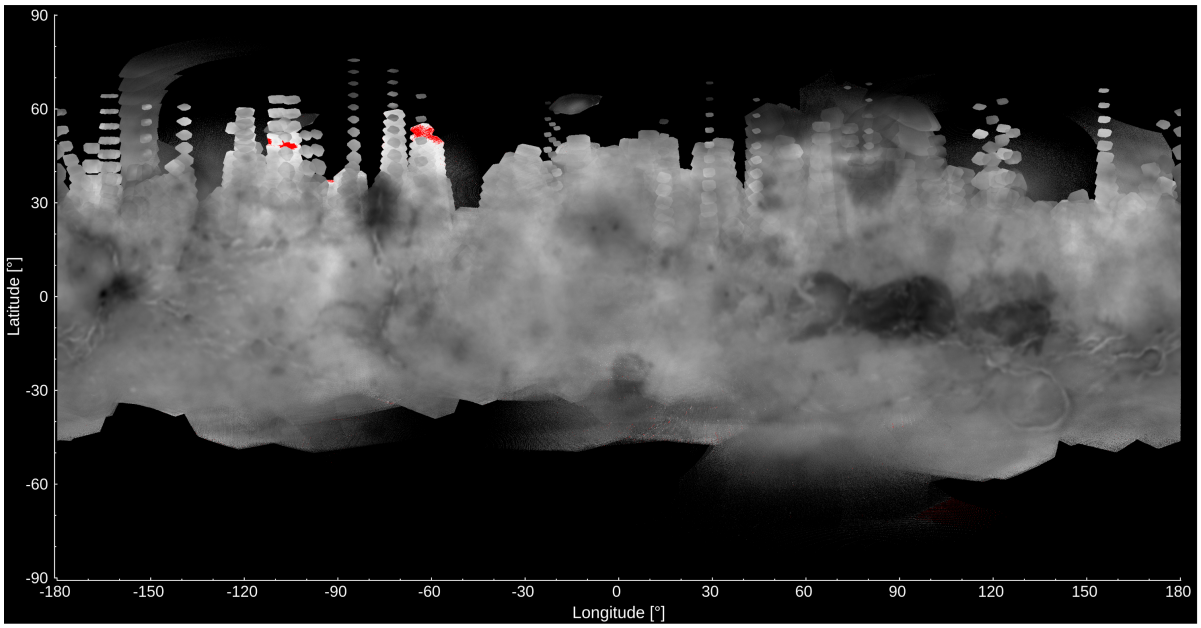

(a) Joined mosaic

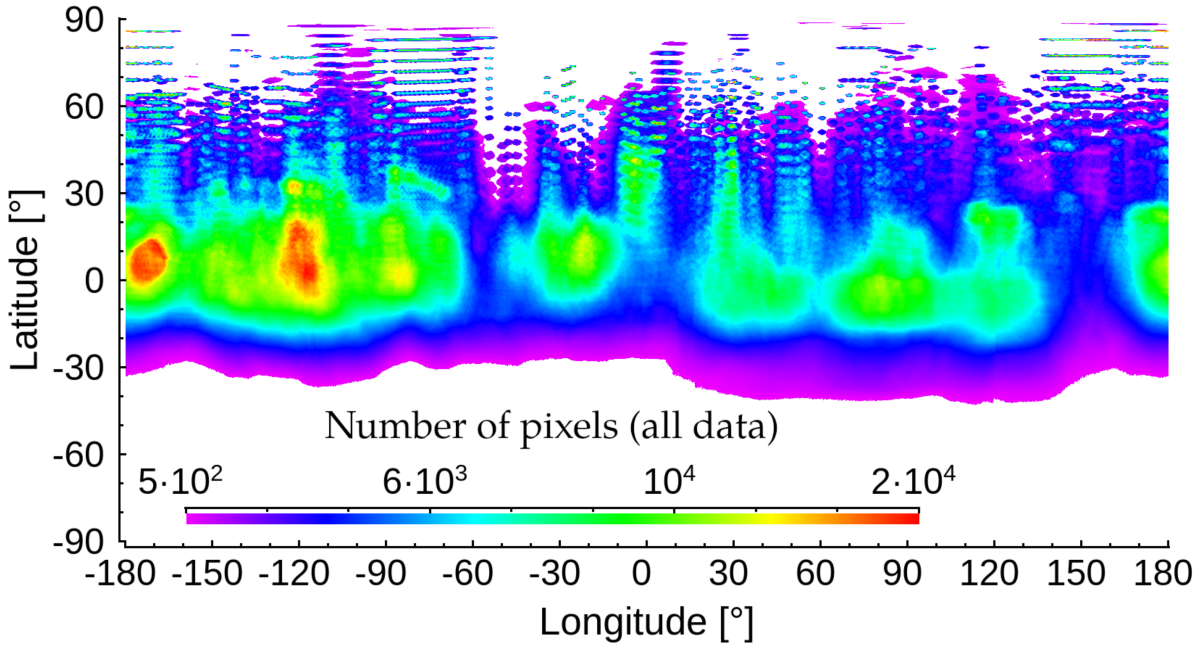

(b) Number of VMC pixels in 0.25° × 0.25° bins.

Figure 2.2.: Mosaic composed of all VMC near-IR images on the night side. Bright areas correspond to lowlands that have higher temperature than the mountain regions (dark spots). Circular structures, coronae, are well visible in the lower right of the mosaic below large dark region, Aphrodite Terra

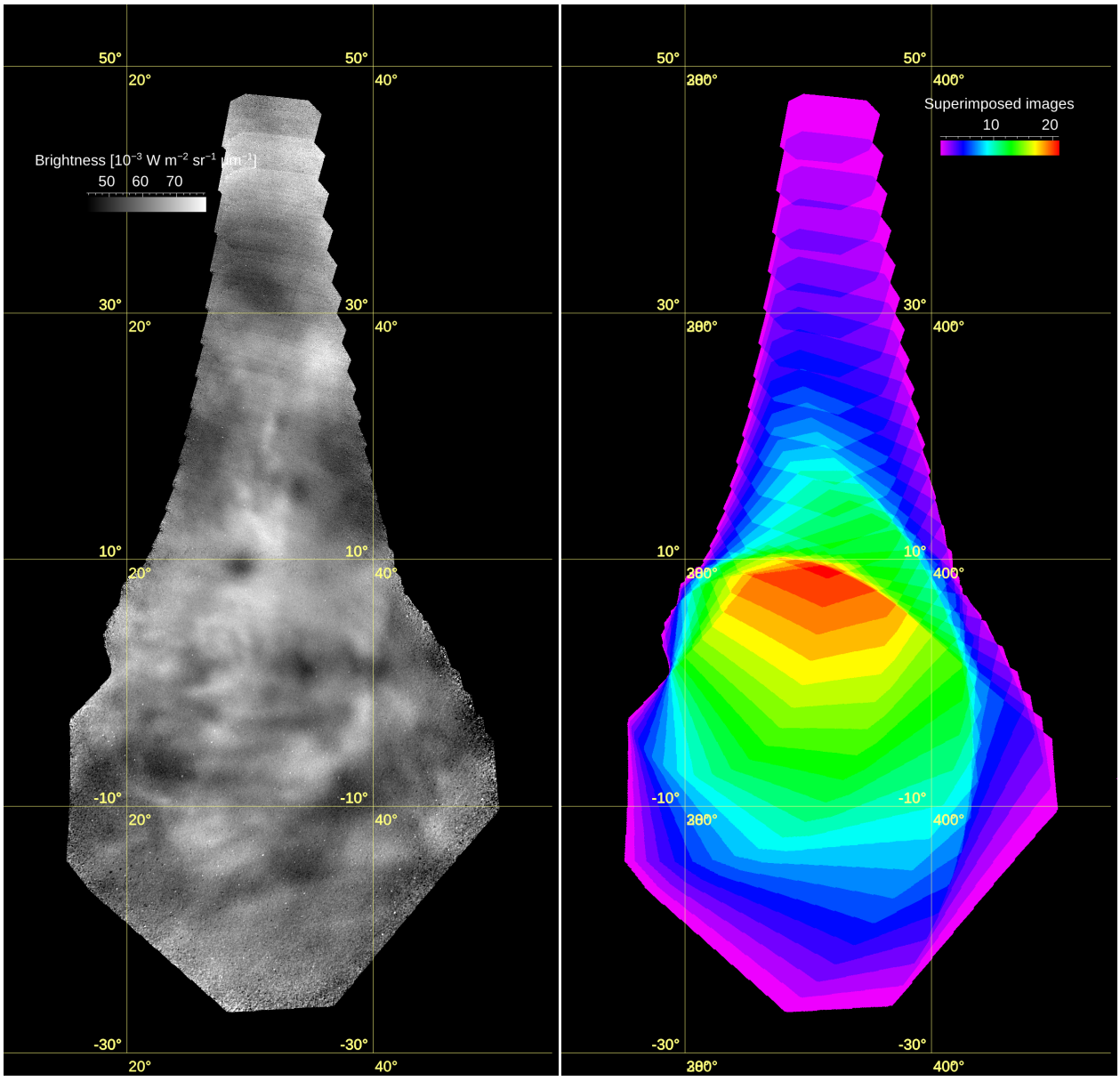

(a) Mosaic build from IR2 images from orbit #2253. Equirectangular projection

(b) Map for the number of overlapping images for a

Figure 2.3.: A typical look of a IR2 surface mosaic

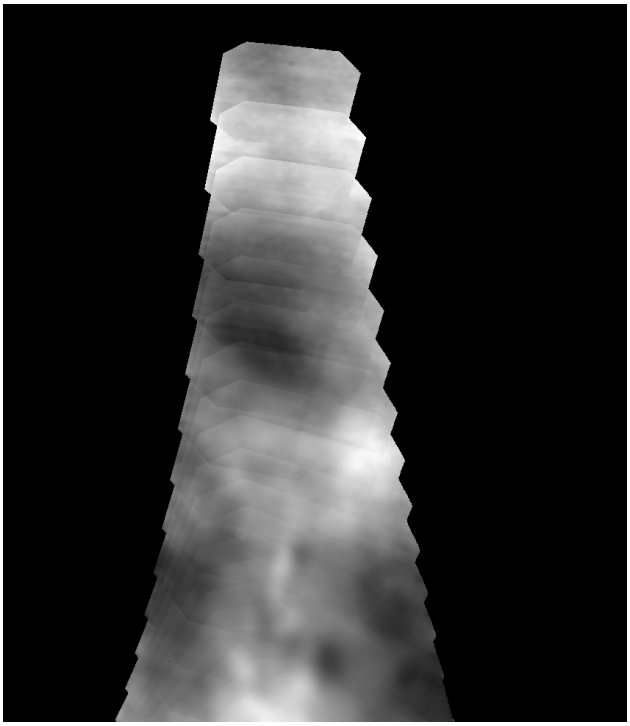

Figure 2.4.: North part of the mosaic for orbit #2253, composed of images processed by a low-pass filter

used.

The in-flight damage of the VMC A Charge-Coupled Device (CCD) required additional correction (flat fielding) of the images using featureless images of the Venus polar clouds assuming their uniform brightness. Another issue is that the VMC laboratory calibration is valid for exposures shorter than 4 s, while surface images were taken with the longest exposure of 30s. Both calibration uncertainties manifest themselves as inconsistent brightness values in overlapping images (fig. 2.6). Surface observations by the VMC were possible only when the VEx was in the planet shadow; this implies imaging starting from distance as close as ~ 500 km and up to a few thousand km. Together with the rotation of the spacecraft, this observational geometry results in the typical shape and overlapping, shown[1] in fig. 2.3. One can easily notice, looking at the top part of fig. 2.3a, uneven brightness discontinuities, which correlate with the individual VMC images (see fig. 2.3b). Figure 2.4 highlights these details.

2.2. Method of automatic image restoration

This work proposes an advanced image processing to minimizing brightness differences between overlapping images. The adjustment was done automatically by fitting the flat fields for each orbit by a smooth function minimising squared deviation between registered brightness in consecutive images for the same regions. The mismatch between individual images can be as high as $10\,\%$ to $12\,\%$ with the typical value being twice smaller. The goal of the first task is to improve the situation lowering the discontinuity steps down to $1\,\%$ and update the VMC data in the Planetary Science Archive (PSA) archive with the improved images.

The data preparation for the correction and further processing revealed some additional problems with the additional flat fields (AFFs). When additional flat-fielding was performed during the mission, two incorrect assumption were made:

1. The laboratory flat field for NIR2 with 30 s exposures correctly corrects for first-order gradient across the field of view.
2. The only purpose of the additional flat field is to correct for local artifacts.

[1] Hereinafter please zoom in the images to see the discussed details; the images contain ~ 3 Mpix.

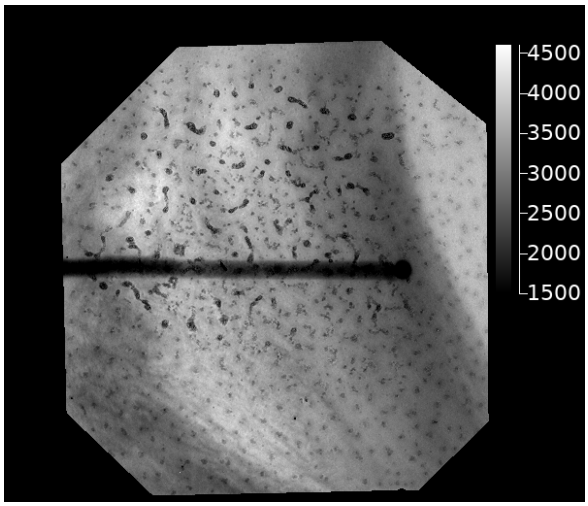

(a) Image # 44 from orbit # 2032, UV channel

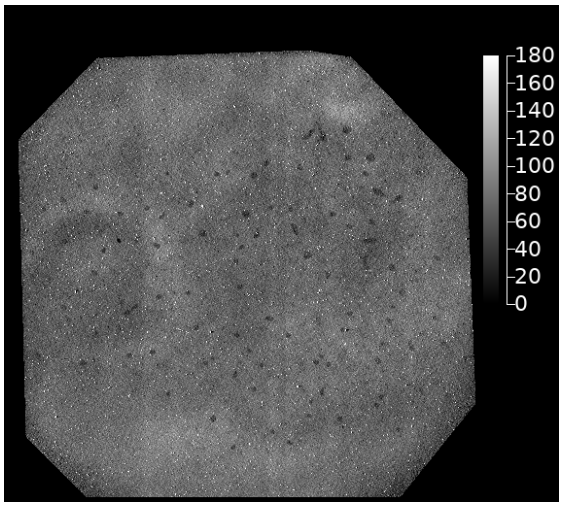

(b) Image # 66 from orbit # 1376, NIR2 channel

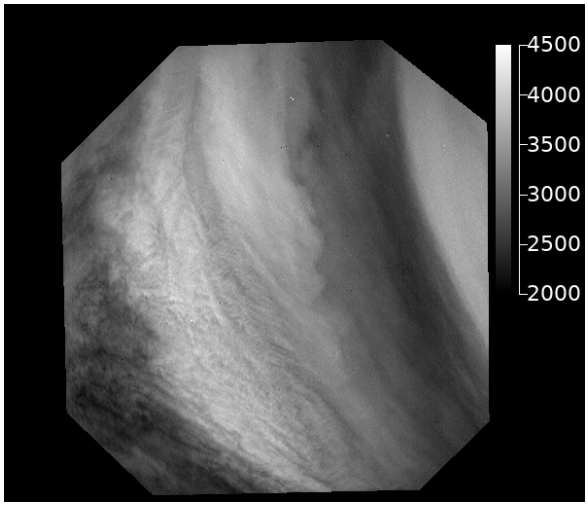

(c) Image # 44 from orbit # 2032, UV channel, additional flat field applied

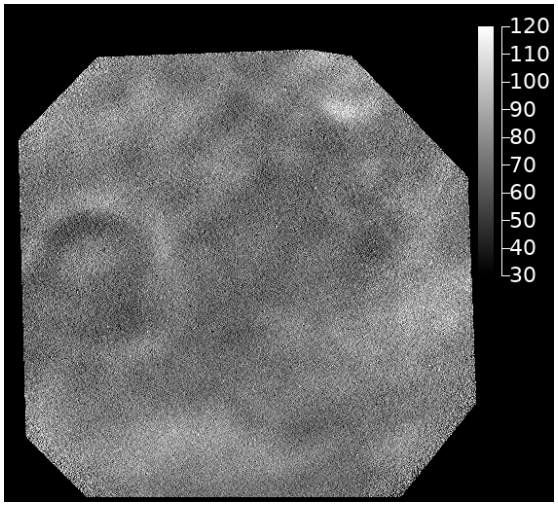

(d) Image # 66 from orbit # 1376, NIR2 channel, additional flat field applied

Figure 2.5.: Examples of artefacts in VMC images

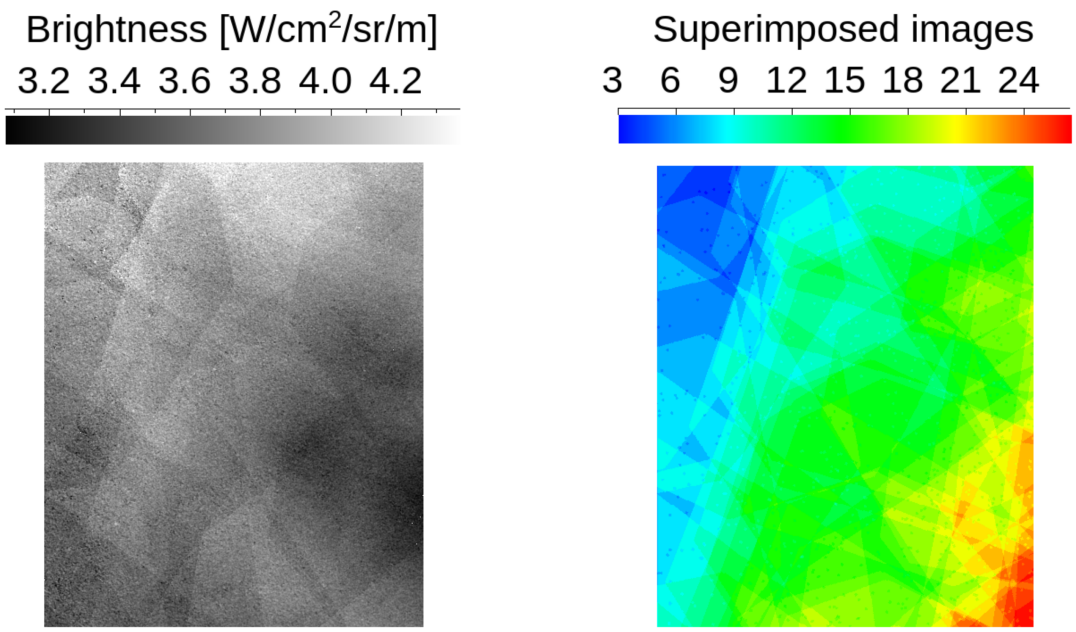

Figure 2.6.: VMC mosaic for region 31°N – 39°N and 21°E – 29°E. Straight lines are borders of the individual VMC images

However, the first assumption turned out to be incorrect and thus the second one made no sense anymore. To correct the images, yet another flat field was computed for each orbit. This second additional flat field is a first order gradient, computed to minimise image-to-image deviation in surface mosaics.

At this stage of the project we apply corrections to the individual images and produce second additional flat fields. Nevertheless, the discovered problems impose limitations on the data usage, which are important for the next stages of the project and may be of use for the community. Thus we summarise discovered problematic cases below.

The additional flat fields for the VMC night-side data were created from the very night-side images, taken close to the VEx pericentre where night clouds are seen with relatively high resolution (no surface detail variations are in the VMC field of view) and are, therefore, nearly featureless. A few of these images (usually around ten) had been manually selected and averaged to produce an AFF image for the given orbit. But, as it appears, finding suitable files had been impossible for certain orbits and produced AFFs either contain various artefacts or contain no target image.

The artefacts usually fall into one of the following categories, but in sometimes more than one damages is present:

stray light the AFF image contain the stray light pattern (reflection inside the camera optics);

border artefact corner parts of the AFF image are either too bright or too dark;

noise the AFF image is so noisy that it can be used for flat-fielding;

surface feature one or more surface features are visible in the AFF image.

The automatic correction is supposed to produce adjustments for the AFFs and apply it to the level 2 sub-level 1 IR2 night-side images. The AFF adjustment was modelled using a plane surface, a second order surface, and a polynomial surface with orders up to 4.

2.2.1. Results retrieved from the automatic correction

The automatic procedure was applied to a set of orbits and it revealed three typical cases, which will be illustrated below. The difference between the cases is created by differences in sequencing of more and less problematic images.

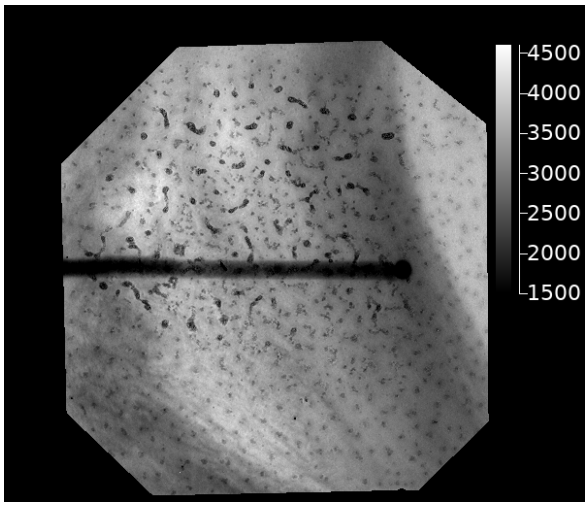

(a) Image # 44 from orbit # 2032, UV channel

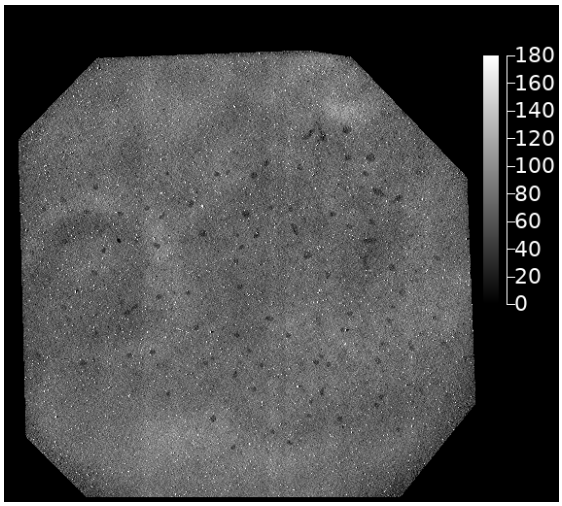

(b) Image # 66 from orbit # 1376, NIR2 channel

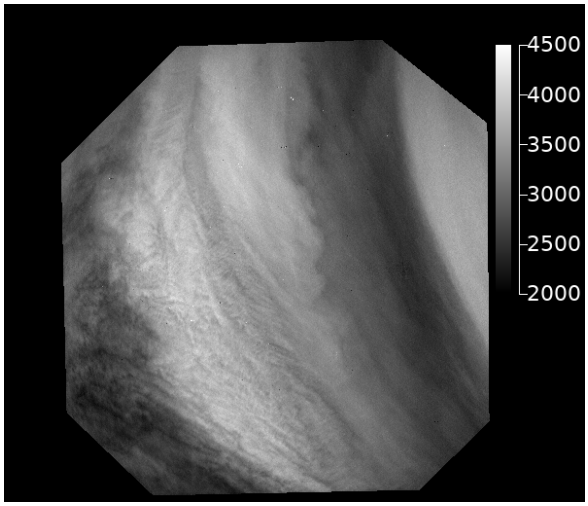

(c) Image # 44 from orbit # 2032, UV channel, additional flat field applied

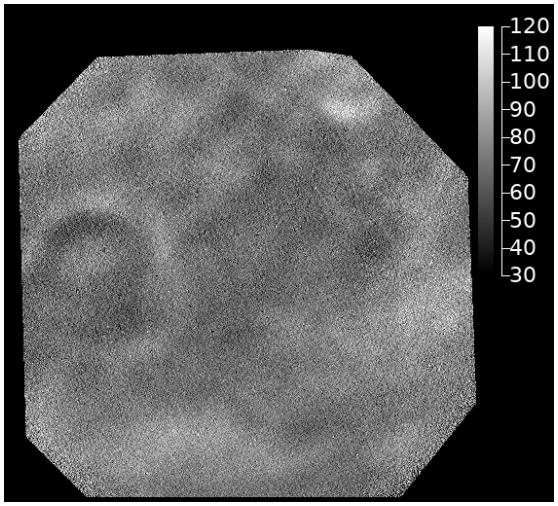

(d) Image # 66 from orbit # 1376, NIR2 channel, additional flat field applied

Figure 2.7.: Examples of artefacts in VMC images

2.2.1.1. Orbit images are equally bad

Let us consider the simplest case: all the orbit images are equally bad. This case is the most common one, encountered in roughly half the orbits. Orbit 0470 is an example of this behaviour (fig. 2.8). Mosaics from this orbit show stable difference between the overlapping images from north to south (fig. 2.8b), which visually decays in the southern part due to the increase in the number of averaged images, and appears again in the very southern part of the mosaic. Figure 2.9 visualises this differences via the standard deviation between the images that compose the mosaic. In this case correcting the AFF using a plane surface results in significant improvements. Let's compare standard deviation maps for the original filtered images and for the corrected filtered ones (fig. 2.11). The average discontinuity in the middle latitudes ($10°\text{N} - 30°\text{N}$) decreased from $\approx 6\,\%$ down to $\approx 1.5\,\%$, which correspond to the four times decrease in the standard deviations (fig. 2.11).

Note that the pattern in the map of the standard deviation changed and show correlation with something, which is not image edges, up to $18°\text{N}$. We will come to this in section 2.2.1.4.

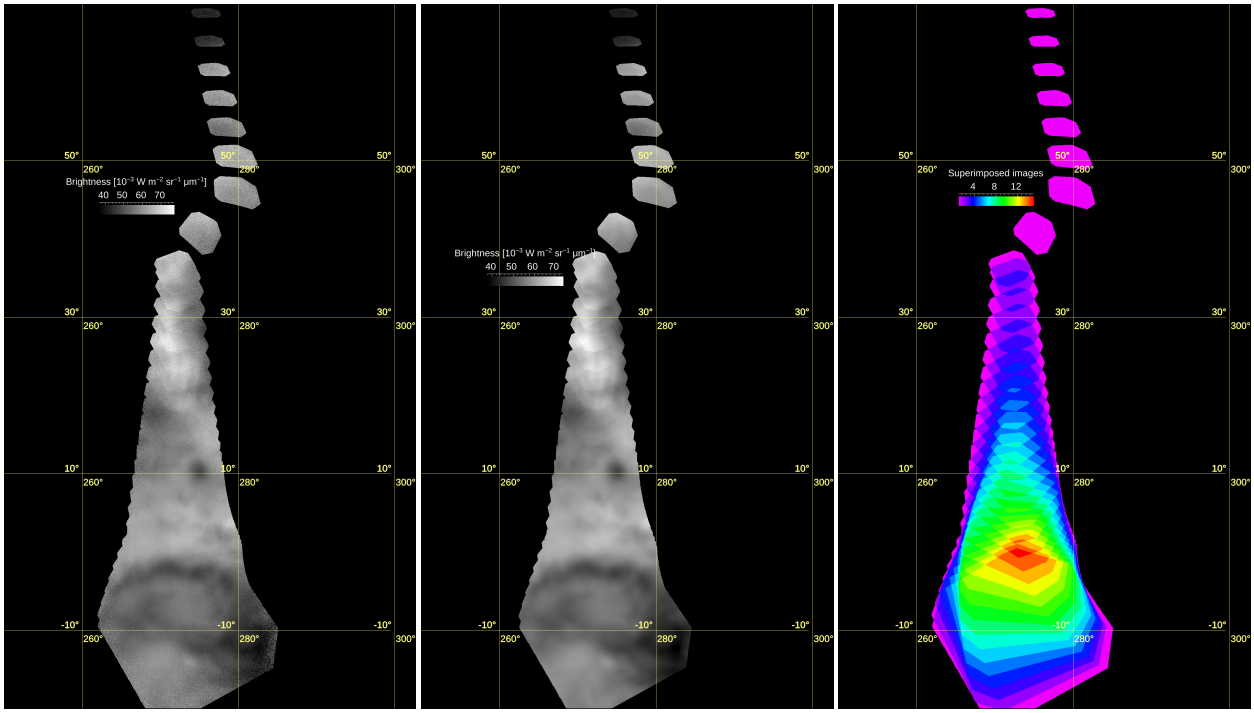

(a) Mosaic build from IR2 images from orbit #0470. Equirectangular projection

(b) Same as in a but after applying median and low-pass filter to the individual images

(c) Map of number of superposed images for orbit 0470

Figure 2.8.: Mosaics for orbit 0470. The mosaic in panel b contains less random noise and thus displays the systematic discontinuities between the tiles better

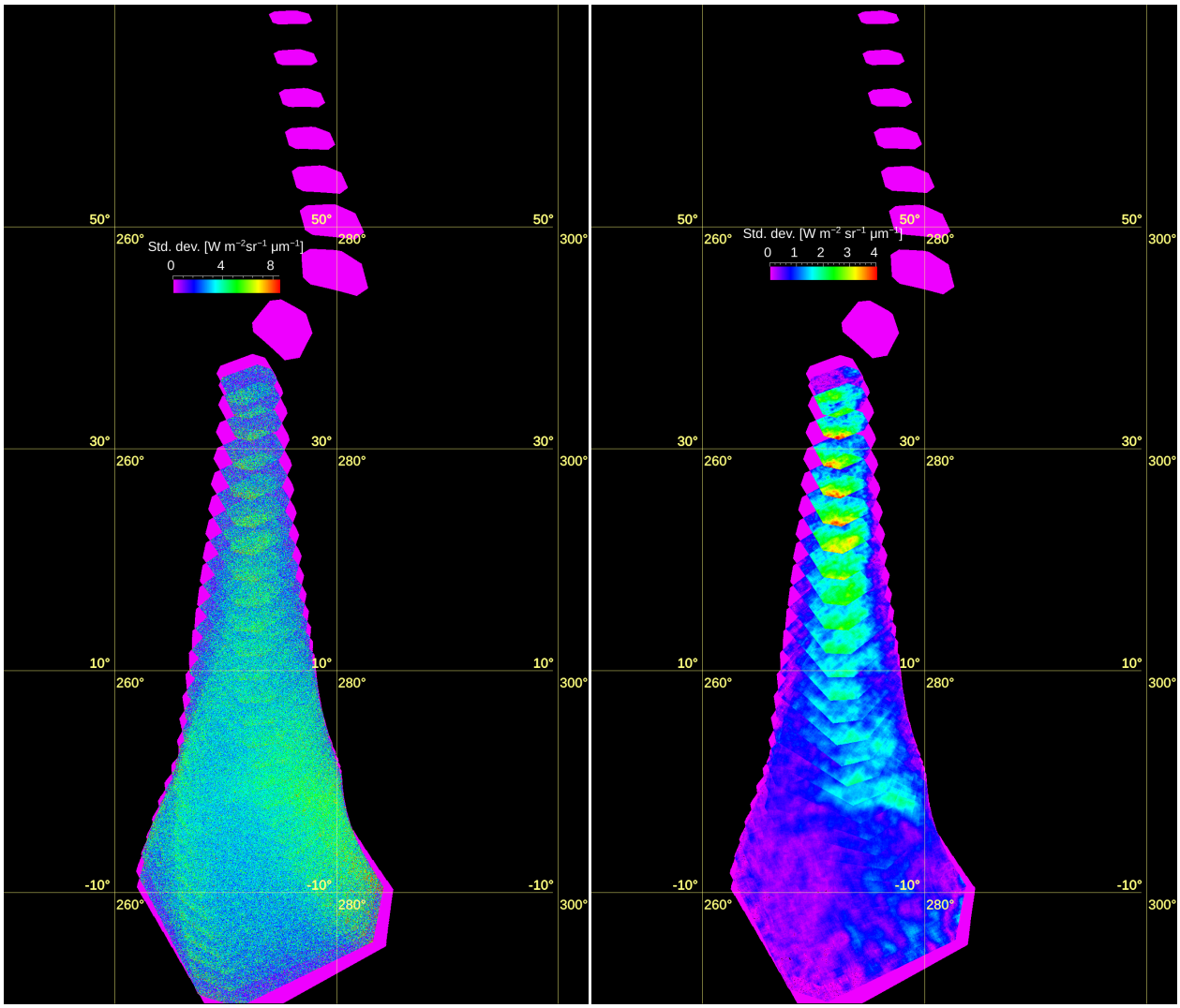

(a) Original VMC images

(b) Images after median and low-pass filters

Figure 2.9.: Standard deviations between tiles for orbit 0470. The map in panel b shows that almost all image overlapping regions show the similar discontinuity

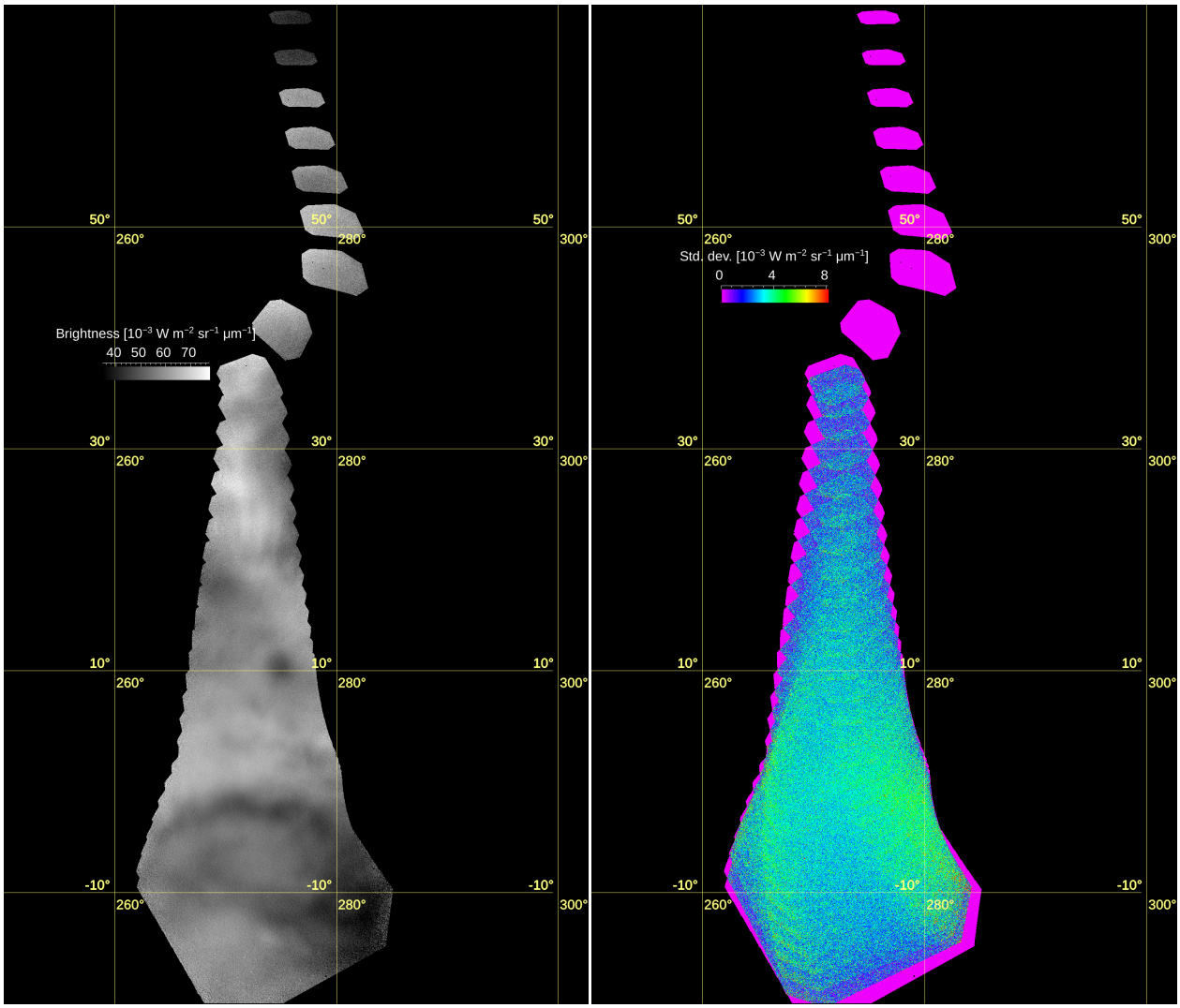

(a) Improved mosaic (b) Standard deviation map for a

Figure 2.10.: Corrected mosaic for orbit 0470 in a and its standard deviation in b

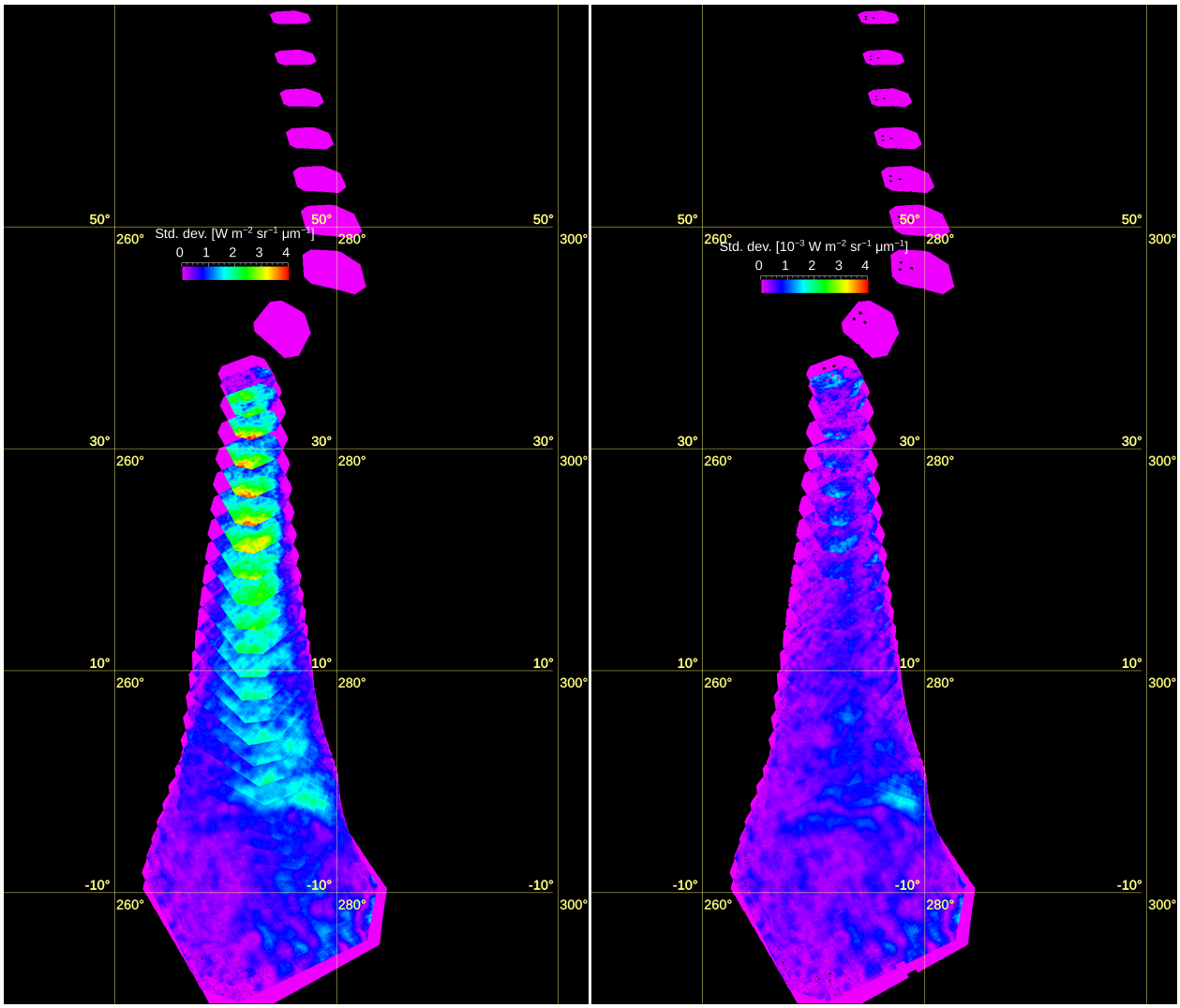

(a) Original images

(b) Corrected images

Figure 2.11.: Comparison between standard deviation maps for the filtered (median and low-pass filters) original VMC images a and the corrected and filtered ones b. Orbit 0470

2.2.1.2. Later orbits

Now let's consider another example, orbit 2253. These images (fig. 2.12) were obtained almost 5 years later and the camera signal to noise ration decreased due to aging. Therefore the mosaic (fig. 2.12a) is more noisy the that for orbit 470. Correction using a plane fit results in some improvements, shown in figs. 2.13 and 2.14. For this orbit we see that while the correction with the plane surface removed significant part of the discontinuity, but another pattern in the mosaic overlapping region was revealed (clearly visible in latitude $25°\text{N} – 40°\text{N}$). Additionally, an unknown details in the standard deviation maps in the southern part are observed. Part of them may be connected with surface features (*e.g.* the vertical structure north and south from the Salus tesera) while others may come from the AFF errors.

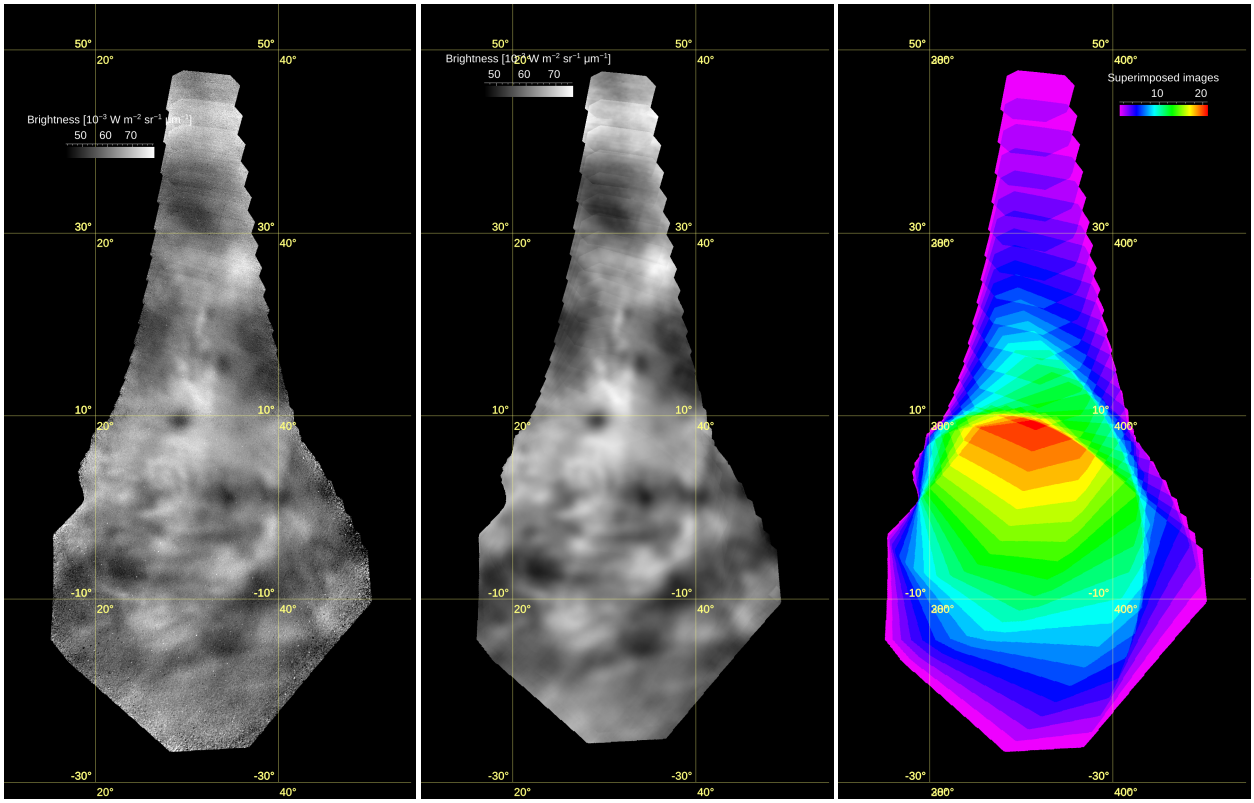

(a) Mosaic build from IR2 images from orbit #2253. Equirectangular projection

(b) Same as in a but after applying median and low-pass filter to the individual images

(c) Map of number of superposed images for orbit 2253

Figure 2.12.: Mosaics for orbit 2253. The mosaic in panel b contains less random noise and thus displays the systematic discontinuities between the tiles better

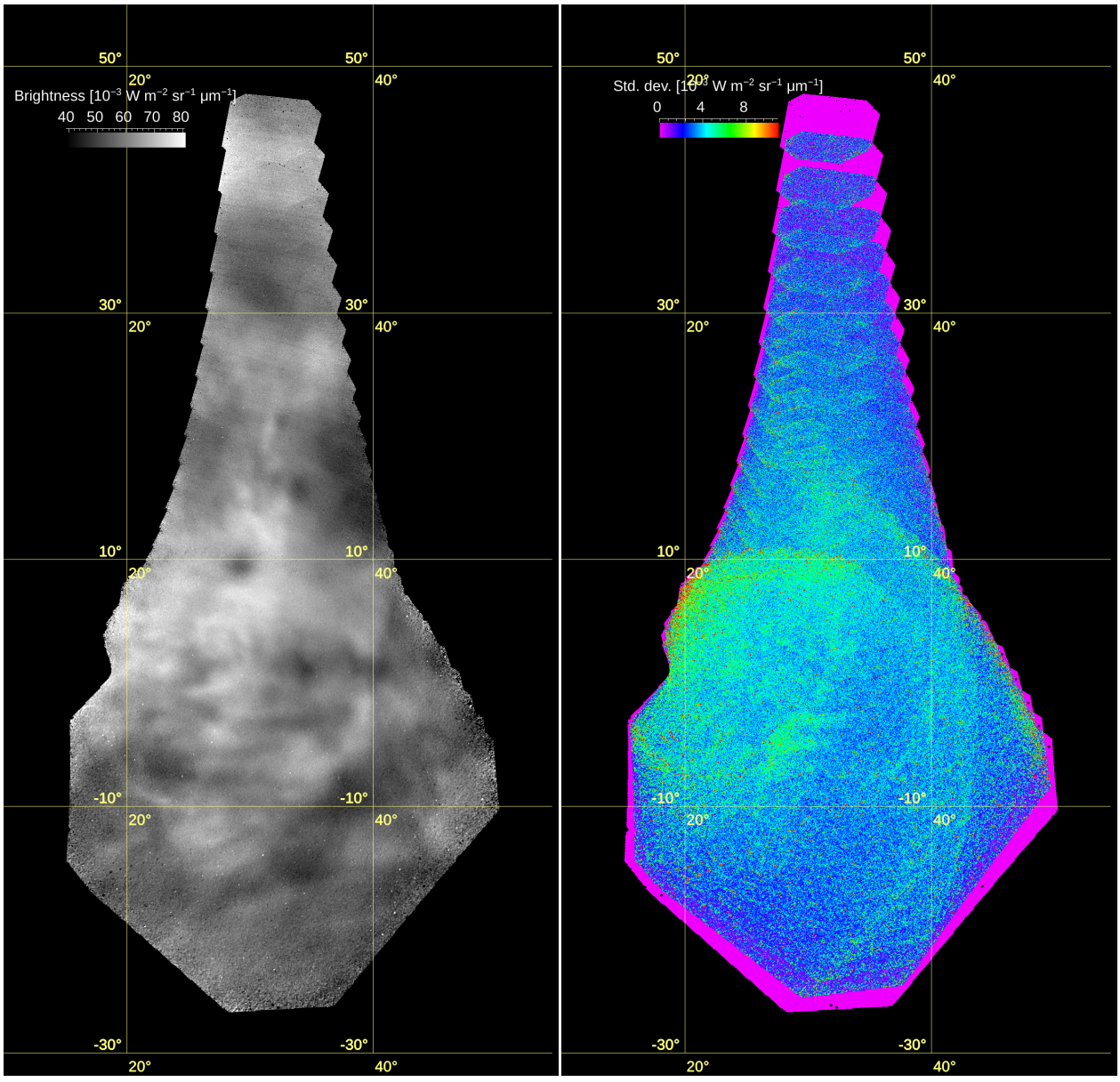

(a) Improved mosaic

(b) Standard deviation map for a

Figure 2.13.: Corrected mosaic for orbit 2253 in a and its standard deviation in b

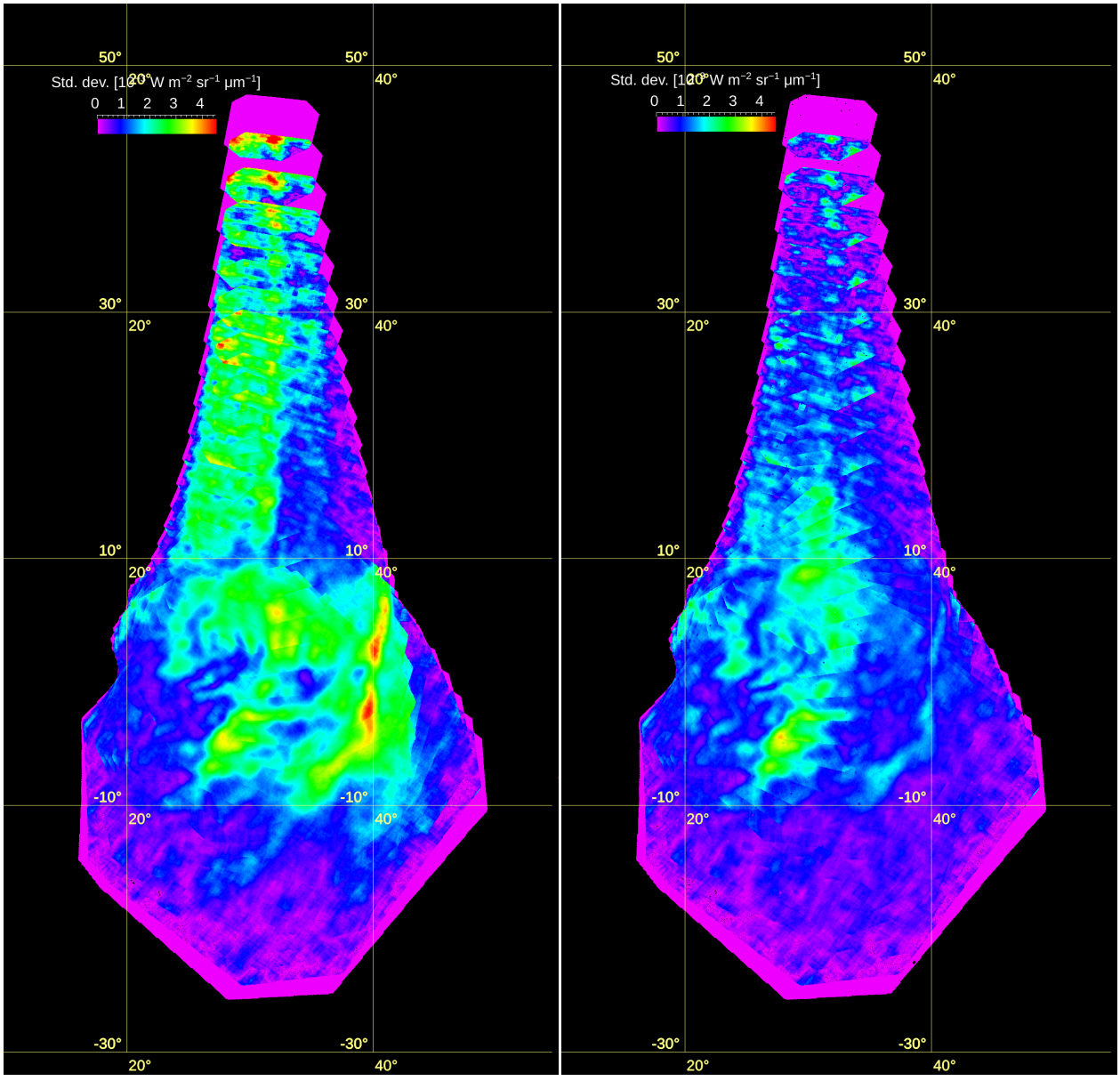

(a) Original images

(b) Corrected images

Figure 2.14.: Comparison between standard deviation maps for the filtered (median and low-pass filters) original VMC images a and the corrected and filtered ones b. Orbit 2253

2.2.1.3. Clusters of images

The last example is orbit 1148 (fig. 2.15). From one hand this example is interesting because here we clearly distinguish two parts of the mosaic: the wider and darker lower part and the bright tail in high latitudes. The strongest discontinuity is between these two parts (at $\approx 20°$N). The correction has improved the northern part of the mosaic (fig. 2.16), but also seems to induced distortions into the southern part (fig. 2.17). Notice the change of the pattern west of the Maat Mons and along the Ganis Chasma. Time separation between the consequent exposures is ≈ 1 min and the exposure time is 30 s. In the case of orbit 1148 the correction procedure can not distinguish between real brightness variation and the AFF error and tries to suppress the former too.

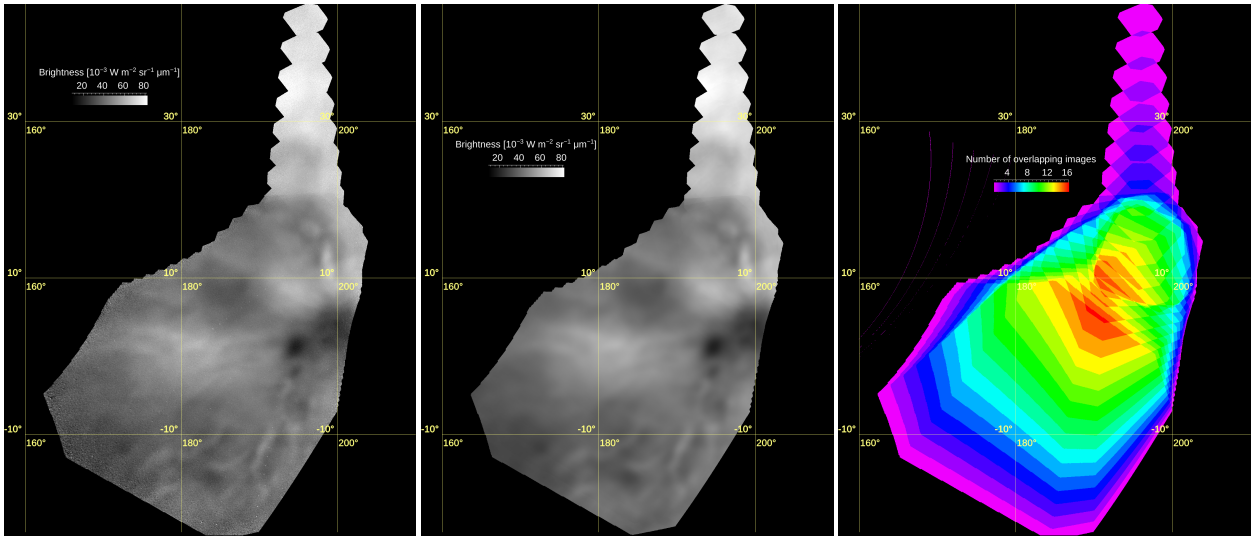

(a) Mosaic build from IR2 images from orbit #1148. Equirectangular projection

(b) Same as in a but after applying median and low-pass filter to the individual images

(c) Map of number of superposed images for orbit 1148

Figure 2.15.: Mosaics for orbit 1148. The mosaic in panel b contains less random noise and thus displays the systematic discontinuities between the tiles better

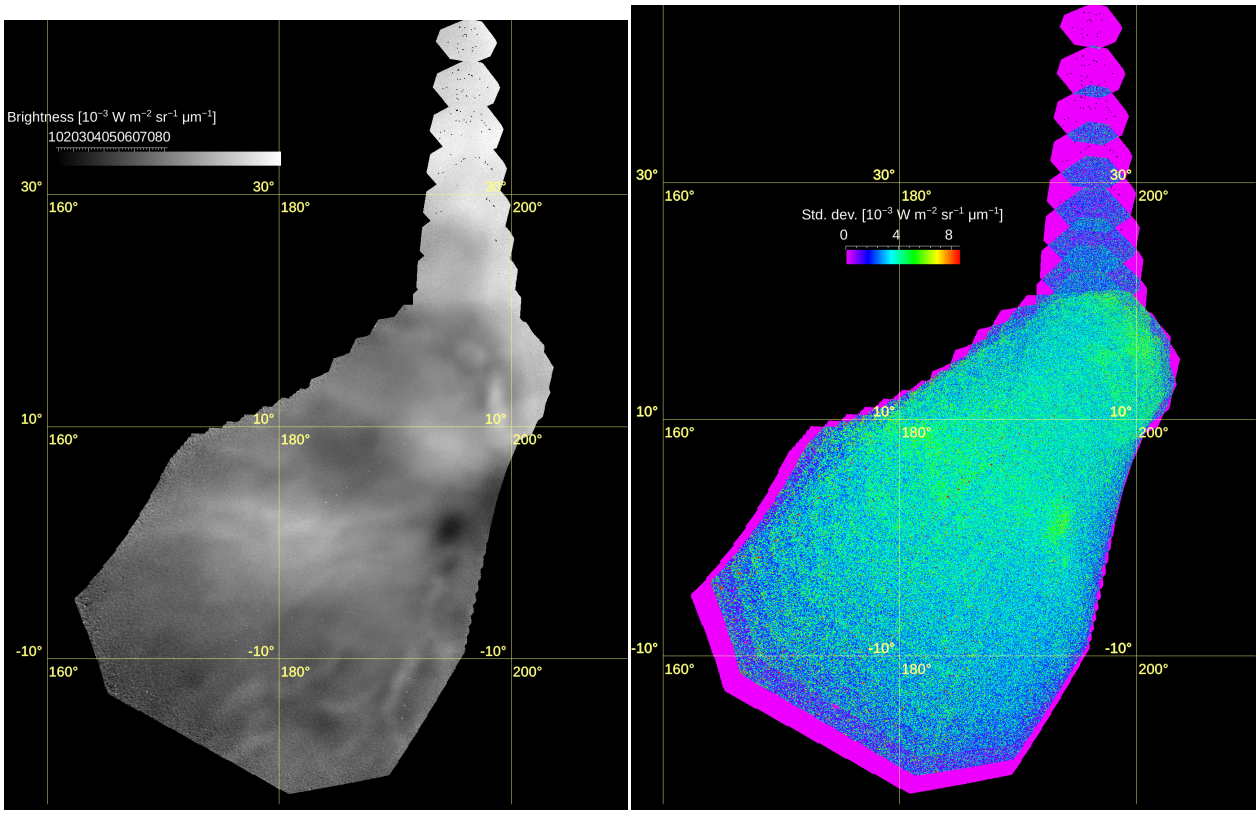

(a) Improved mosaic

(b) Standard deviation map for a

Figure 2.16.: Corrected mosaic for orbit 1148 in a and its standard deviation in b

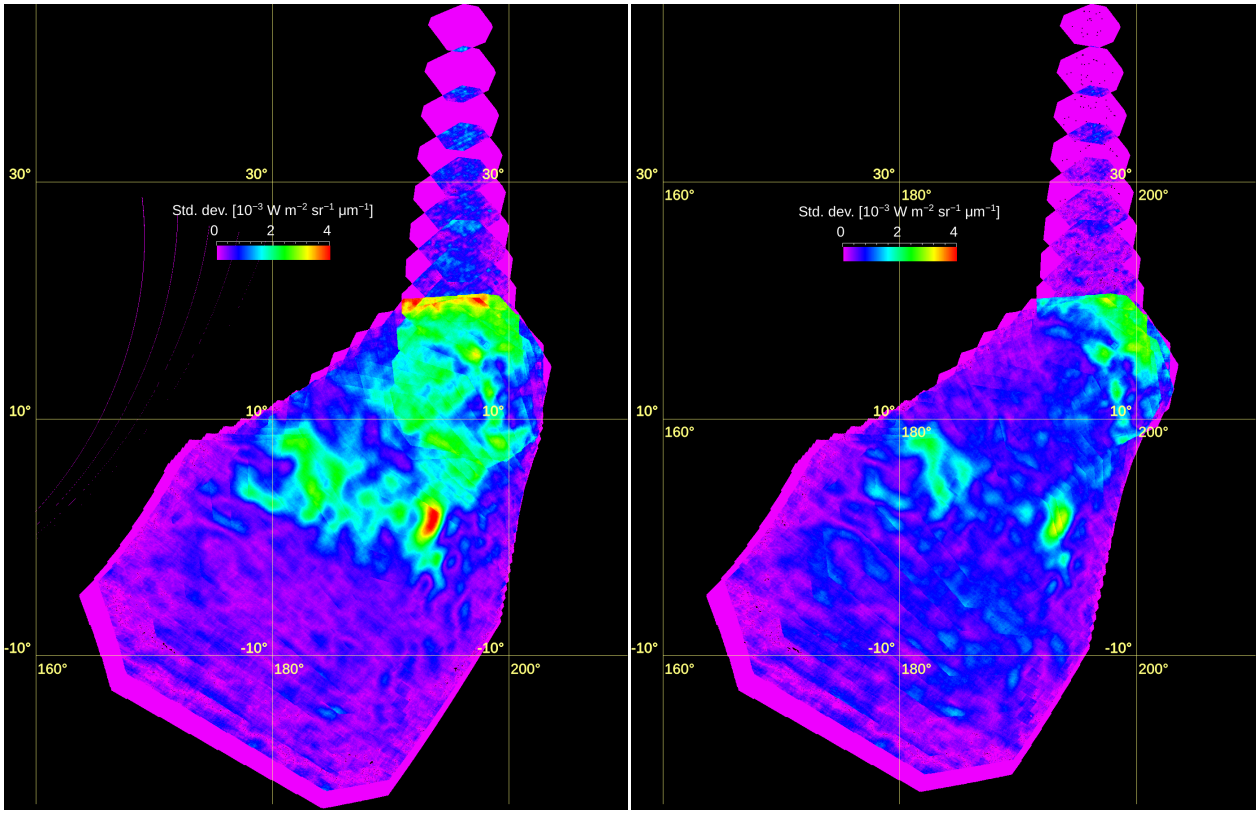

(a) Original images

(b) Corrected images

Figure 2.17.: Comparison between standard deviation maps for the filtered (median and low-pass filters) original VMC images a and the corrected and filtered ones b. Orbit 1148

2.2.1.4. The patterns in maps of the brightness standard deviations

Two considered cases, orbits 2253 and 1148, illustrate an observation that was never made before with the VMC surface data. In usual observation sequence VMC IR2 surface images were taken with exposure of $30\,\mathrm{s}$ every minute (with IR1 images in between). When we compute the image-to-image standard deviation, we see strong patterns in these mosaics fig. 2.18. The details we are interested in are the bright plume ($\sim 0.5°\mathrm{N}, 195°\mathrm{E}$) with a wavy "tail" to the west, and three or four yellow spots along the arc to the north-east from the plume in orbit 1148; two red spots along almost $40°\mathrm{E}$ meridian in orbit 2253. These details in images survive the correction (figs. 2.14 and 2.17) but the correction greatly reduced their visibility. However, these objects do not follow the regular pattern of the AFF errors, but they appear above surface details. In particular, for orbit 1148 the biggest detail is located above the Maat Mons, while the smaller spots are placed along the Ganis Chasma. In case of orbit 2253, the pattern extends to the north and south from the Salus tessera.

Since brightness in the surface images depends on the temperature of the surface, which in turn depends on altitude, the first idea was that these features are artifacts, created by pointing errors. However, in such the case all the artificial details must be accompanied by "ghost", located symmetrically around a topographic detail (a depression or a mount). In these cases no such "ghosts" are observed. Therefore these objects must be created by a yet unknown process in the atmosphere and need an investigation.

2.2.2. Intermediate summary

The goal for this part of work was to develop a software that is able to automatically adjust the additional flat field for the VMC surface images so that the systematic discontinuities between individual images can be lowered down to $\approx 1\,\%$ from the present level of $6\,\%$ (typically) to $10\,\%$ (extreme cases). The developed software adjusts the AFF by minimising variance in a orbital mosaic in regions where individual images overlap. The adjustment can be a plane or a polynomial surface with pre-defined or free order.

Applying the software to a selected set of VMC data, we found the following:

1. In most of the cases, the images in the given orbit are distorted in the same way, and a correction using a plane fit decreases the maximal discontinuity down to $1.25\,\%$ (at most).

2. There is a significant part of orbits, in which corrected images show residual systematic distortion, which can not be approximated by a 1-st order surface, at the level of $1.5\,\%$ to $1.8\,\%$. In these case this distortion pattern is clearly visible in an orbit-wise average VMC image. This distortion can be corrected by additional polynomial fit, but it is uncertain that we would remove only the flat-field imperfections.

3. There are orbits where the maps of image-to-image variances show details, correlated with objects on the surface, like mountains, rifts, or ridges. It is unclear now what do we observe in this case. The software can't distinguish between these features, when they appear in the region of images overlapping, and the flat-field imperfections, and tries to suppress them both.

4. No correlation between detector temperatures and the appearance of non-linear gradients was found.

Despite that it was not possible to reach the planned $1\,\%$ of discontinuities for all data (caused by two different pecularities, see above), the discontinuity decrease down to $1.25\,\%$ gives a reasonable improving for the data.

2.3. Improving the data correction method

Firstly, it was planned to perform a manual correction for the data where the automatic method fails. However, with the gained insight from the previous stage we reached the task goals in the following way:

1. Analyse maps of image-to-image variance for each orbit to separate the data set onto two groups: data with the additional detail and without ones.

2. Orbits without the details can be automatically processed right away.

3. For the orbits where additional details are observed, we:

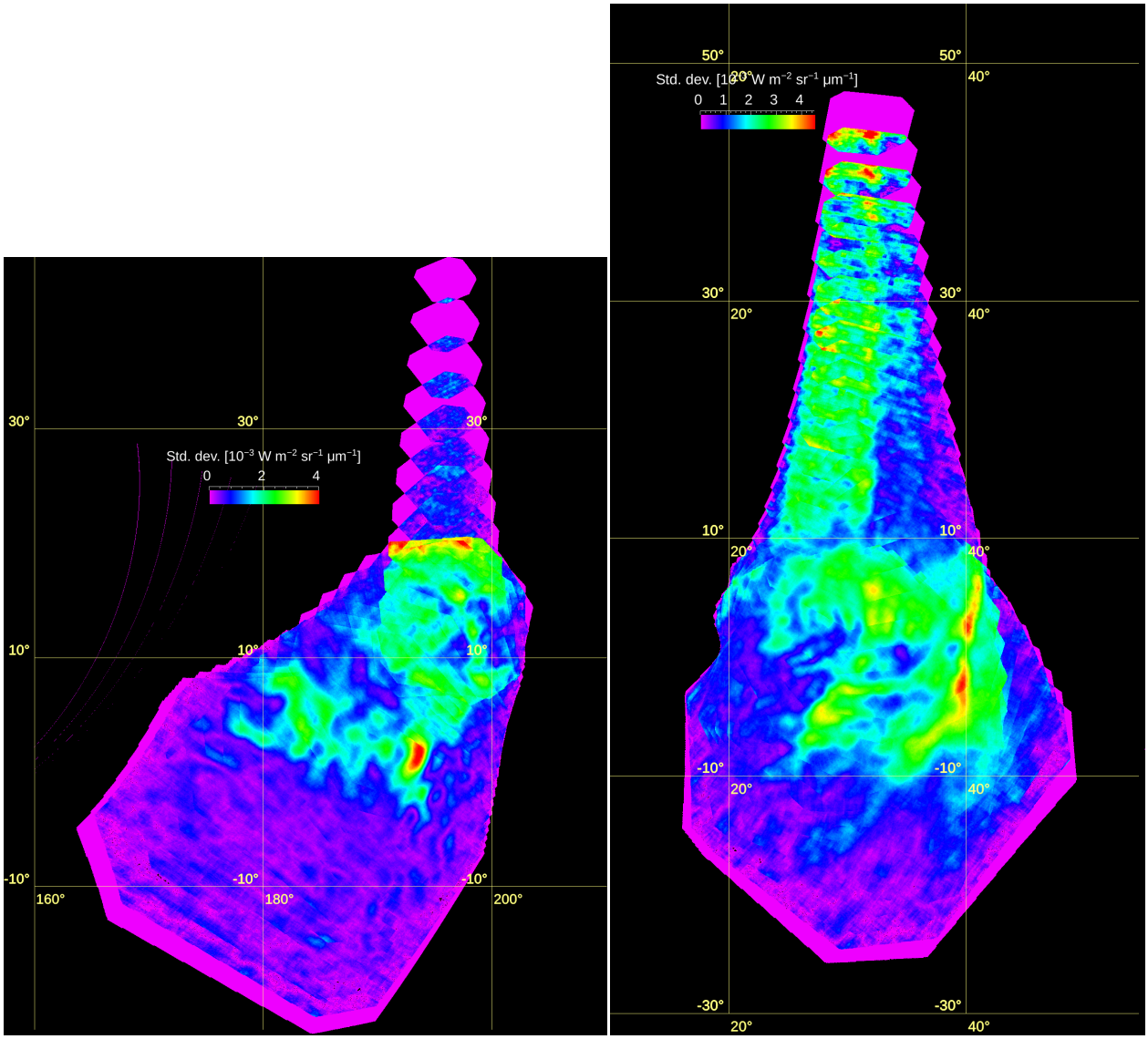

(a) Orbit 1198 (b) Orbit 2253

Figure 2.18.: Examples of the patterns in the maps of the image-to-image standard deviations. The details under interest are listed in the main text

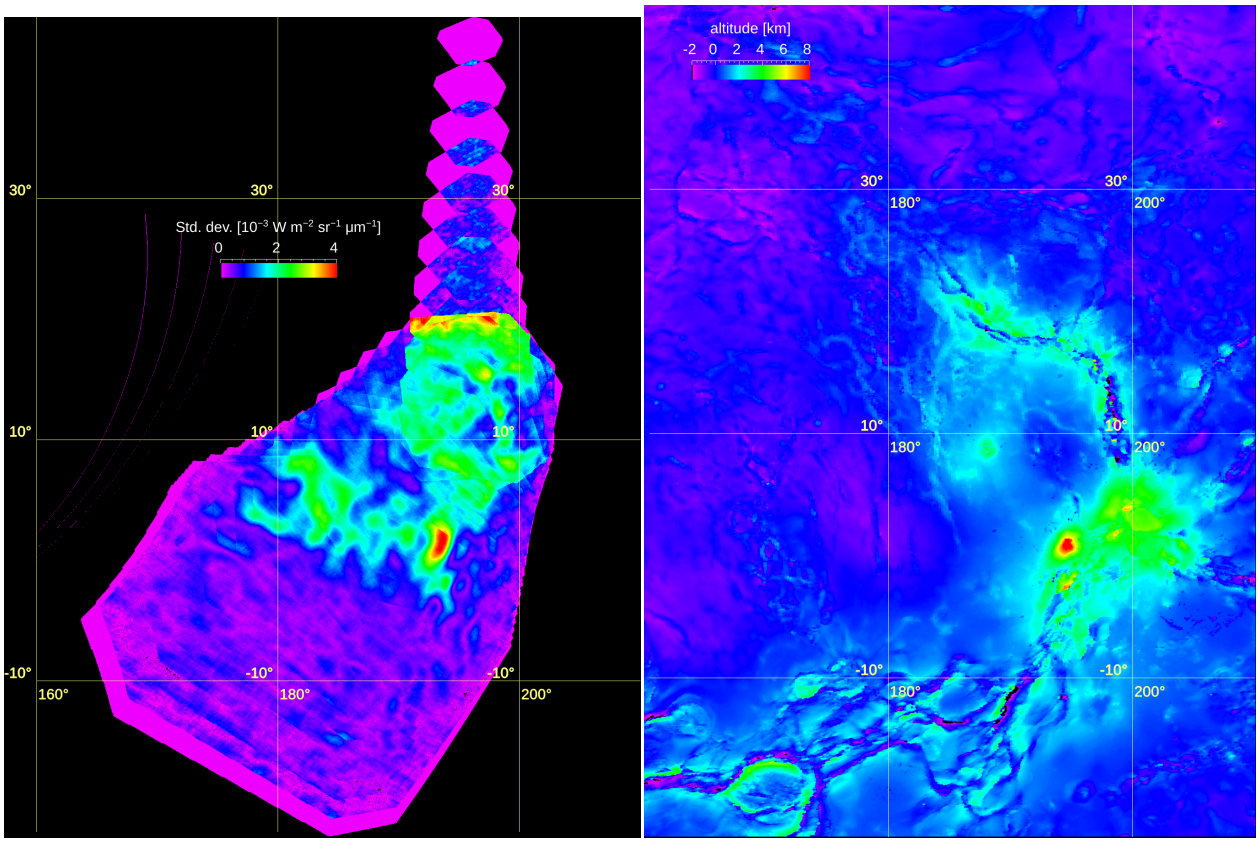

(a) Image-to-image standard deviation

(b) Magellan topography

Figure 2.19.: Comparison of the image-to-image standard deviation and topography maps for orbit 1148

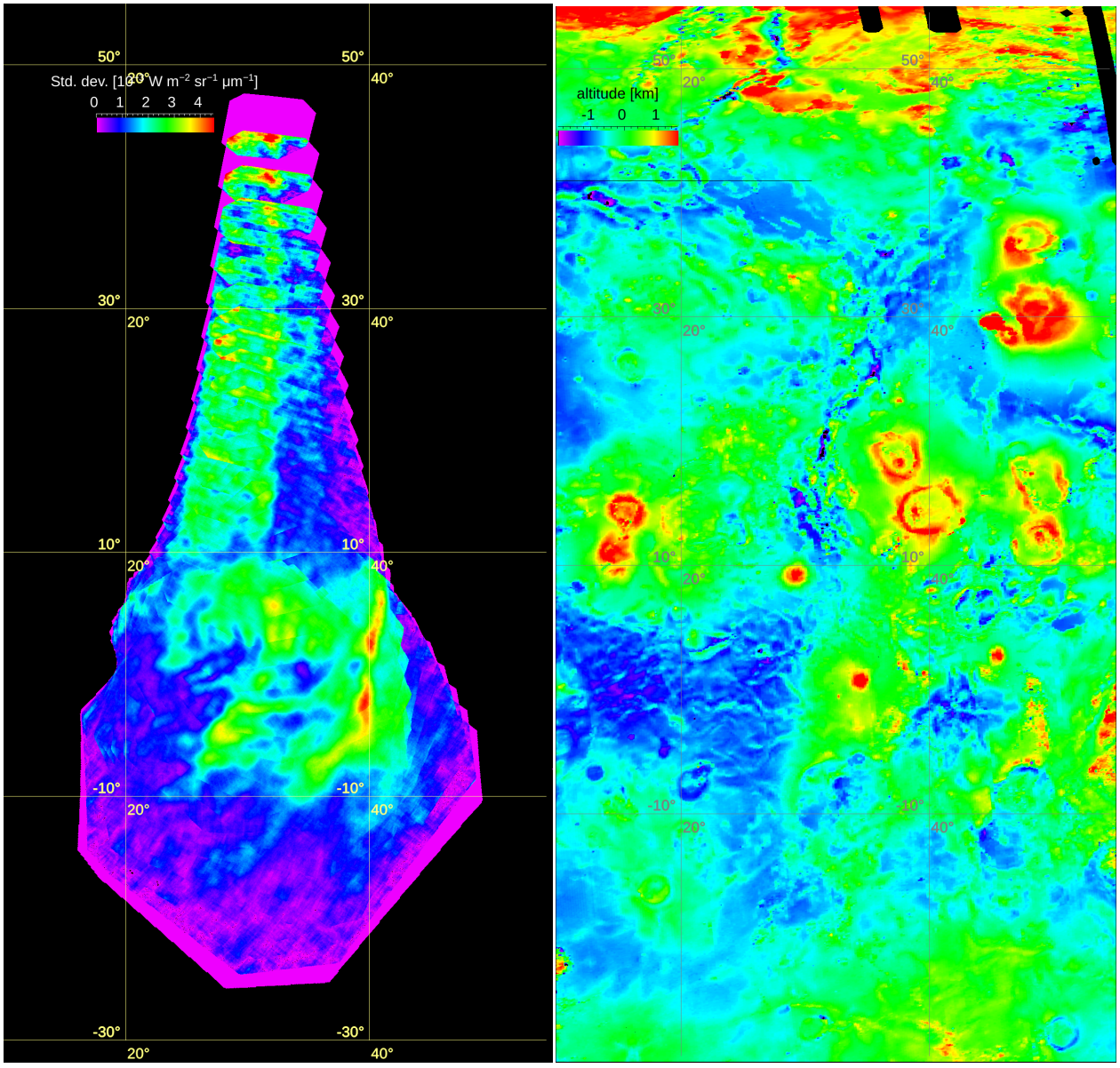

(a) Image-to-image standard deviation

(b) Magellan topography

Figure 2.20.: Comparison of the image-to-image standard deviation and topography maps for orbit 2253

Table 2.1.: Special cases

Case	Number of orbits	Orbits list
Clustered	60	0458, 0472, 0473, 0474, 0475, 0476, 0583, 0586, 0684, 0687, 0688, 0689, 0987, 0988, 0996, 0997, 0998, 1177, 1196, 1236, 1238, 1240, 1249, 1251, 1252, 1255, 1256, 1257, 1258, 1259, 1260, 1261, 1263, 1265, 1269, 1270, 1345, 1346, 1347, 1374, 1375, 1380, 1429, 1459, 1461, 1462, 1464, 1465, 1467, 1469, 1482, 1487, 1518, 1821, 1823, 1827, 2153, 2159, 2372, 2707
Excluded	80	0261, 0387, 0389, 0393, 0457, 0465, 0466, 0467, 0484, 0485, 0591, 0667, 0685, 0686, 0699, 0703, 0705, 0706, 0709, 0710, 0855, 0894, 0895, 1006, 1008, 1010, 1021, 1022, 1029, 1089, 1091, 1139, 1141, 1172, 1173, 1174, 1175, 1179, 1266, 1268, 1423, 1440, 1445, 1447, 1448, 1450, 1526, 1548, 1550, 1552, 1554, 1555, 1691, 1695, 1701, 1714, 1718, 1809, 1810, 1813, 1815, 1816, 1819, 1820, 1920, 2129, 2166, 2370, 2390, 2500, 2593, 2595, 2597, 2599, 2601, 2820, 2821, 2822, 2841, 2842, 2843

a) use only a subset of images for the regions without details to adjust the flat-fields;

b) for the orbits where the non-linear residuals were found, that are repeated in each image, find additional corrections by passing the images through rounds of averaging and low-pass filter.

Thus, instead of fitting the flat-field adjustment manually, we manually selected images for the automatic correction.

2.3.1. Per-orbit data classification

The total number of night-side orbits is 622 (and 12408 usable images). The data can be categorised into the several groups the description and examples for whose are given below (section 2.3.1 and see table 2.1). For different groups the different correction approaches were applied.

2.3.1.1. Typical

Approximately 450 orbits can be considered “typical” and are similar to each other in the way the automatic correction algorithm is able to handle the whole orbital mosaic, equally well (or bad) correcting each region of image overlapping. Figures 2.21 to 2.26 show examples of such orbits and in the original and corrected state. Notice how in the pairs of standard deviation images disappear artefacts, created by the image polygons in their southern parts, leaving soft shapes instead.

2.3.1.2. Excluded

80 orbits contain only a handful of images with only a single image intersection or images were significantly damaged and therefore the AFF gradient correction can not be applied to those orbits, neither in automatic nor in the manual mode. Those orbits were removed from the processing. The list of damaged orbits which are recommended to exclude from the scientific studies is in Appendix and figs. 2.27 to 2.30 show examples.

2.3.1.3. Clustered

60 orbits where image overlapping follows a complicated pattern due to a complex spacecraft rotations, so-called “clustered” orbits. Figures 2.31 to 2.34 show examples. Consider fig. 2.31, where a few darker images overlap the mosaic in its northern (top) part. In most of the cases there are two clusters of images: the bigger one that contains almost all the images from the orbit, and a small one with a few images. For such cases we put away the smaller image clusters and used only the bigger ones.

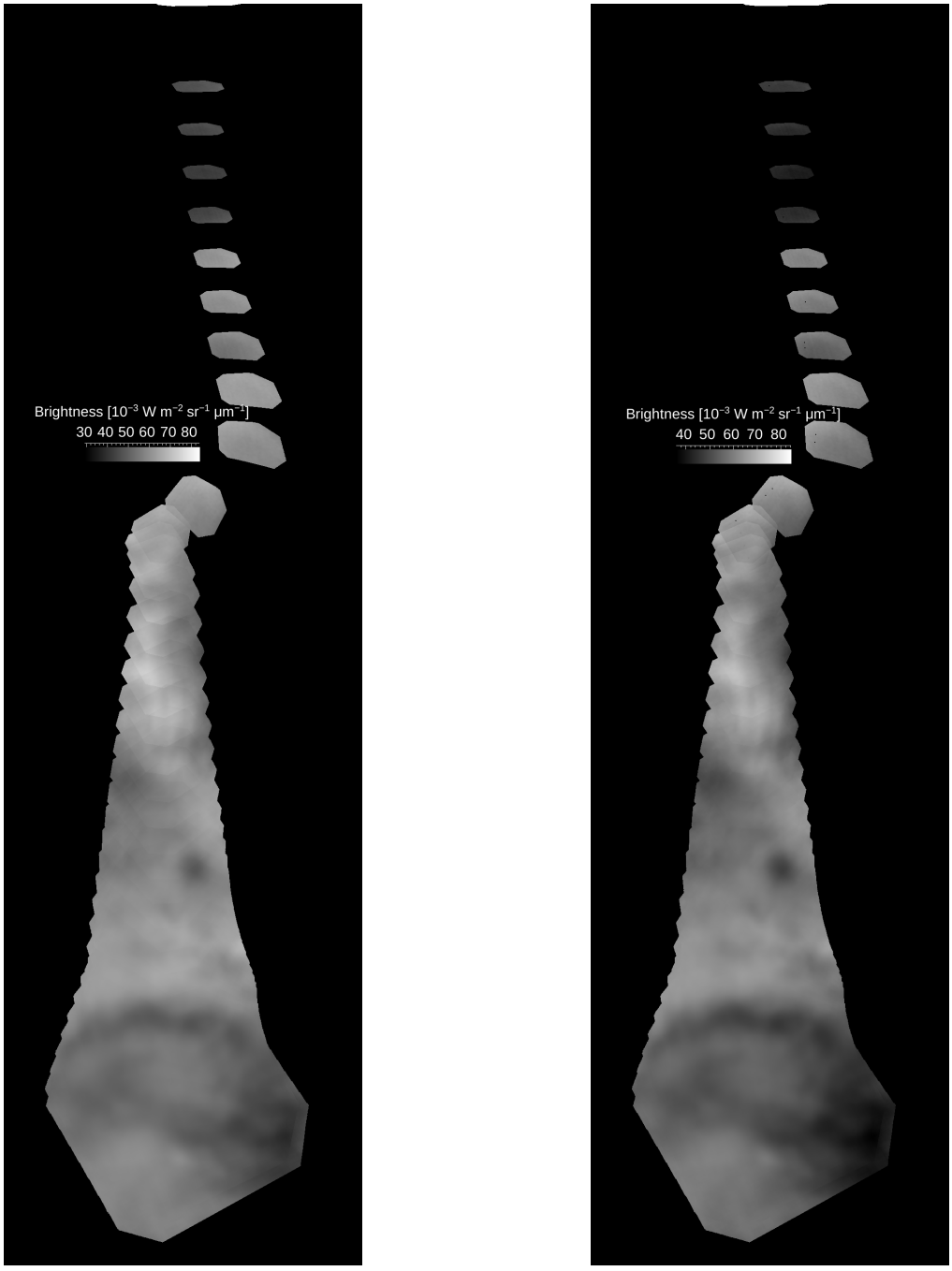

(a) Original (b) Corrected

Figure 2.21.: Original and corrected mosaics for orbit 0470

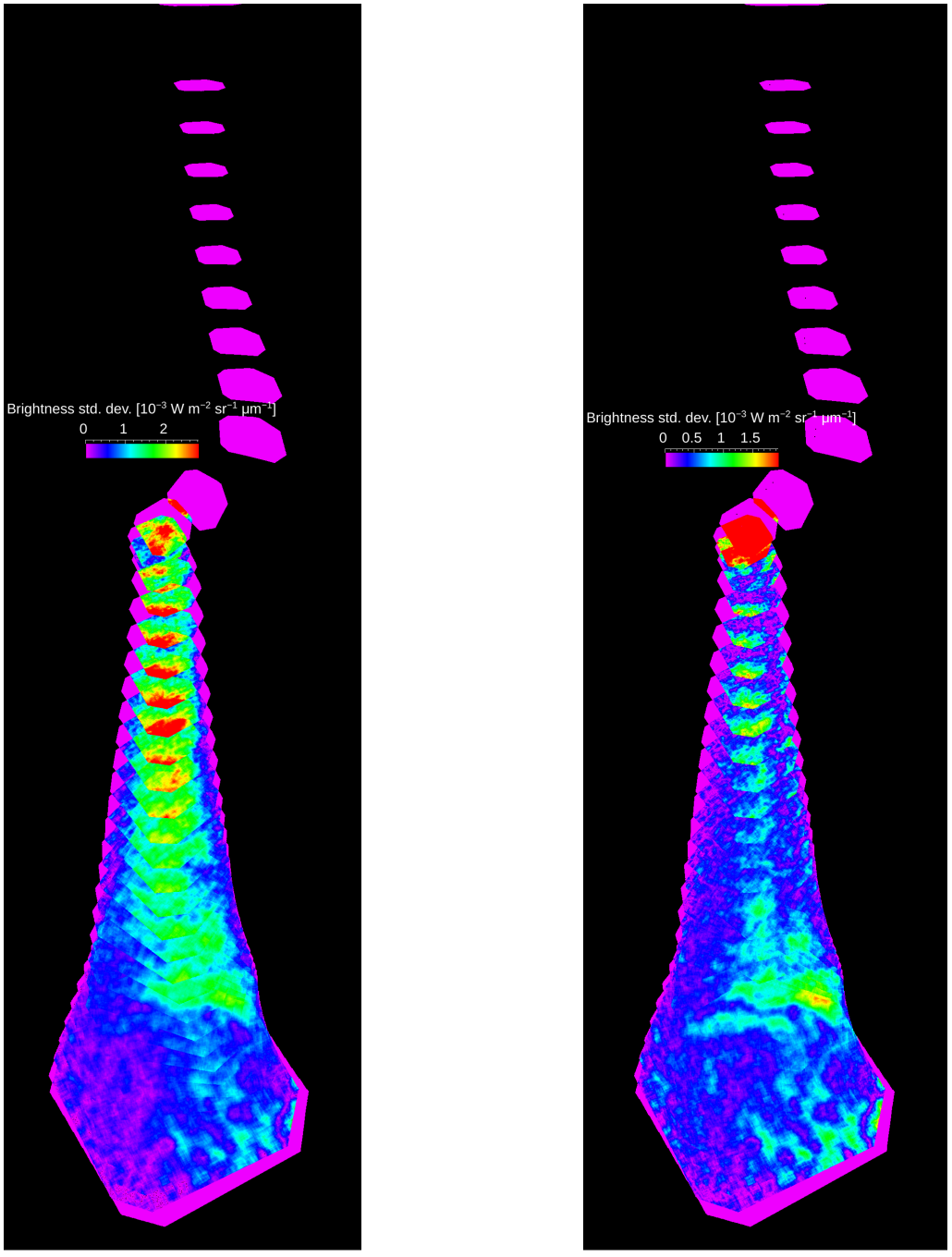

(a) Original (b) Corrected

Figure 2.22.: Maps of standard image to image deviation for orbit 0470

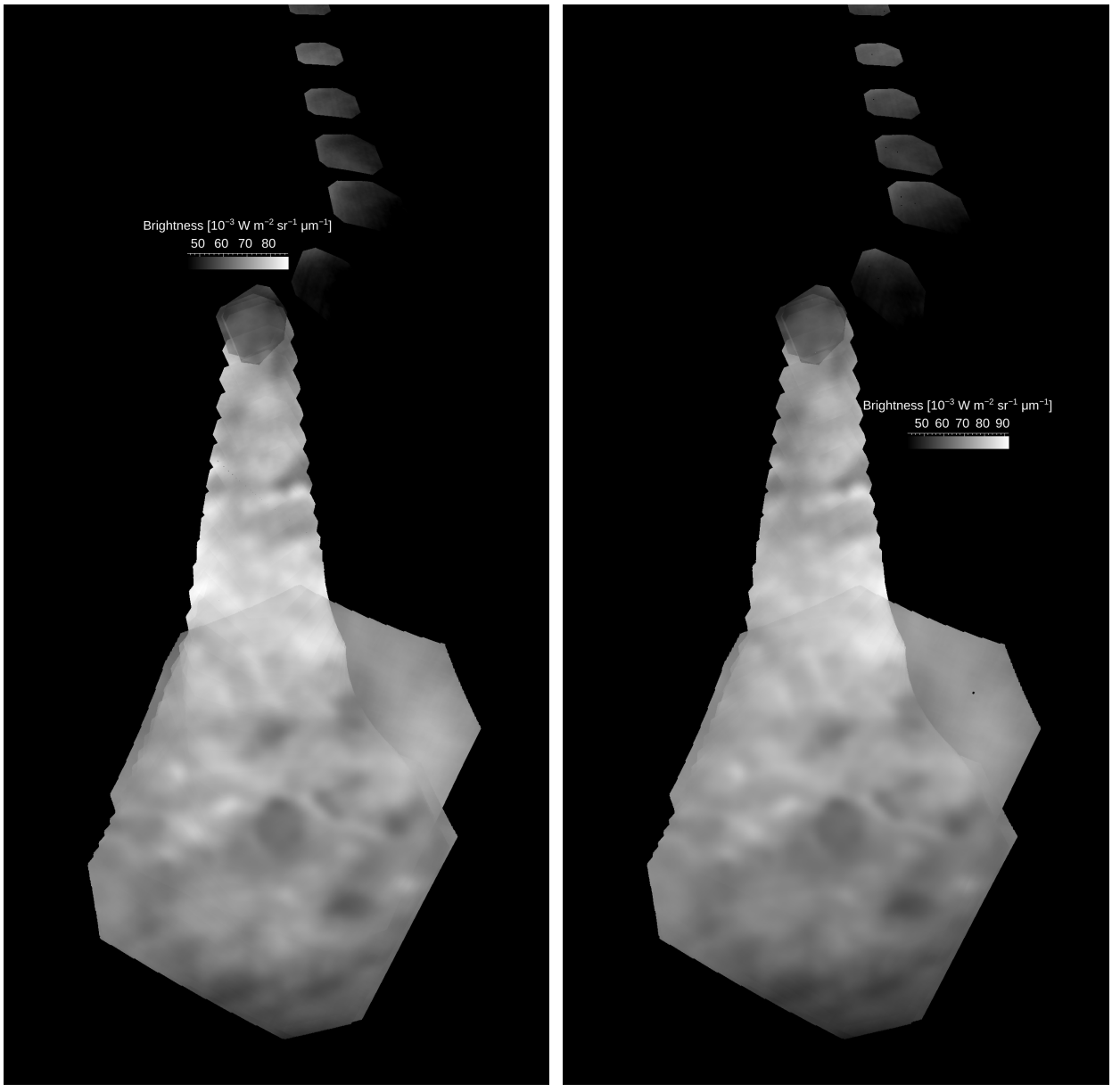

(a) Original (b) Corrected

Figure 2.23.: Original and corrected mosaics for orbit 0693

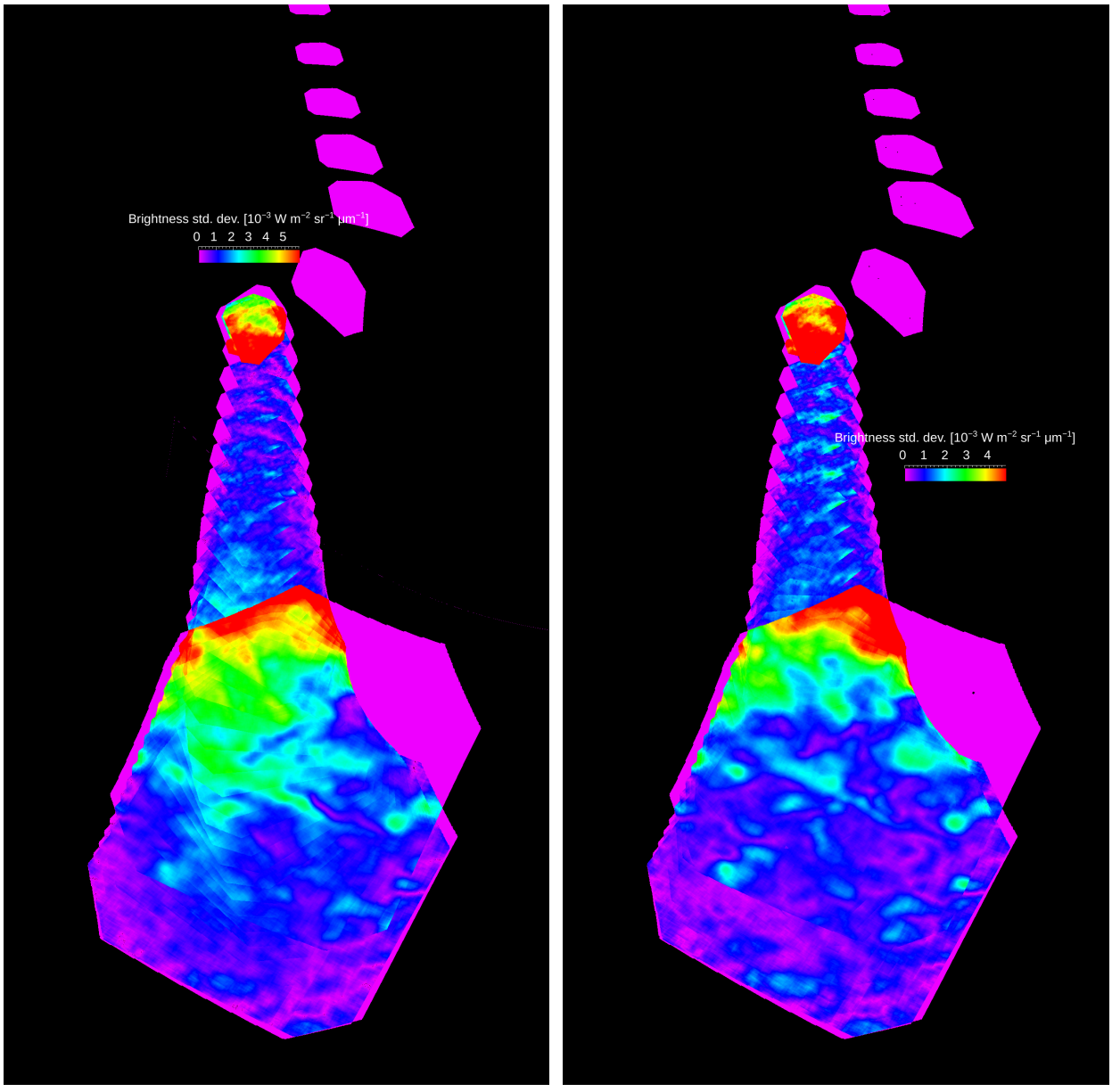

(a) Original (b) Corrected

Figure 2.24.: Maps of standard image to image deviation for orbit 0693

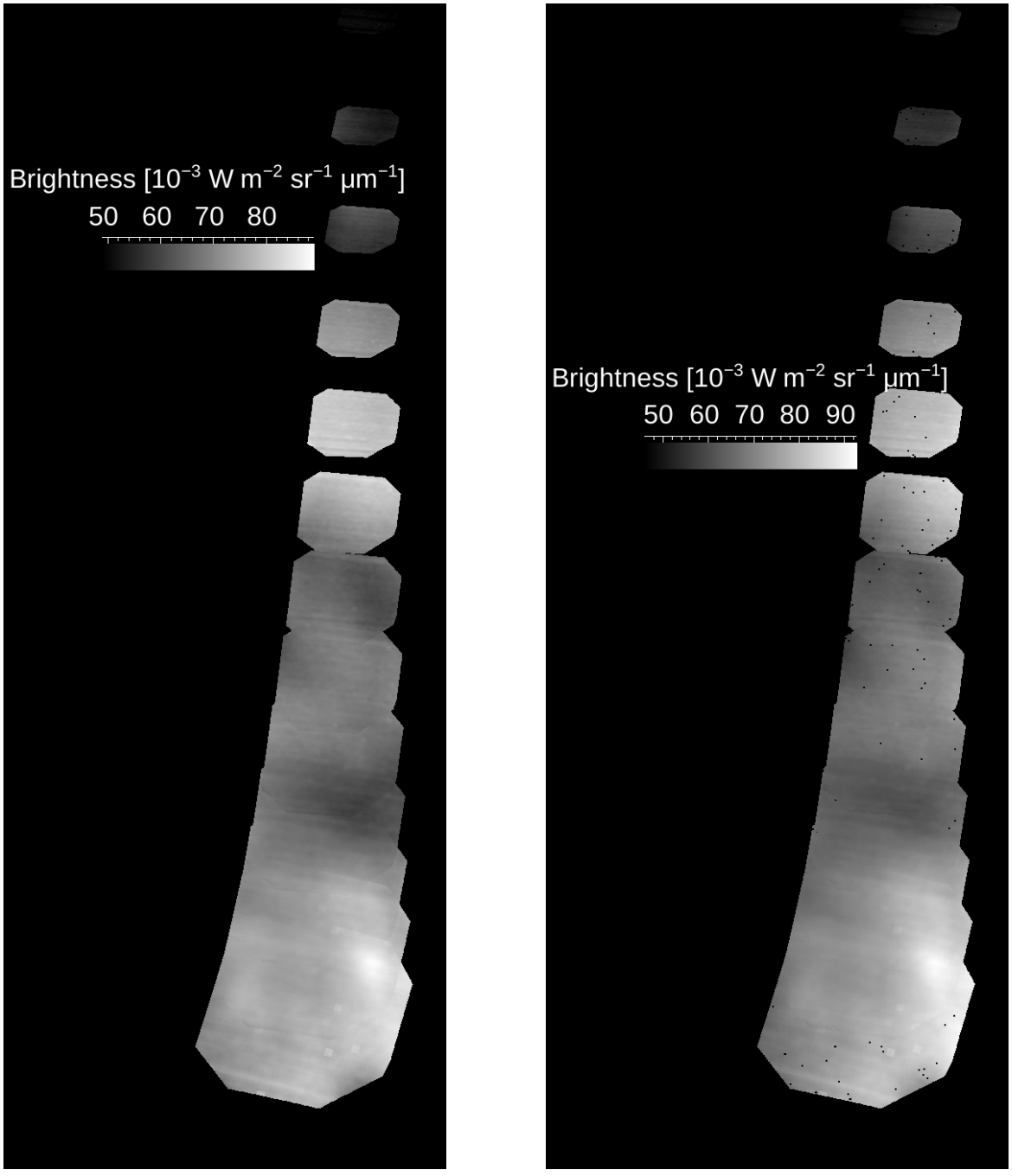

(a) Original

(b) Corrected

Figure 2.25.: Original and corrected mosaics for orbit 2374

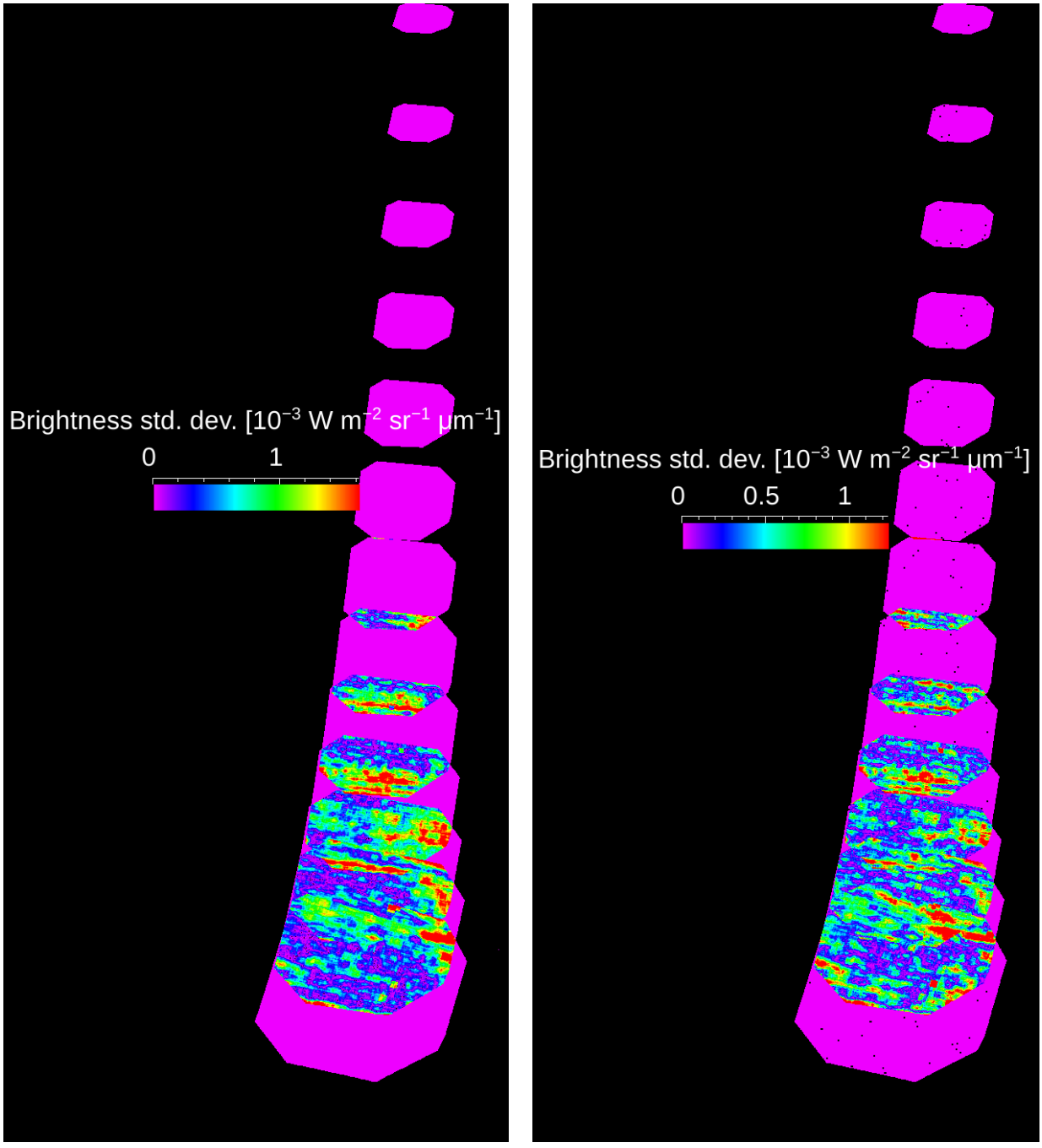

(a) Original

(b) Corrected

Figure 2.26.: Maps of standard image to image deviation for orbit 2374

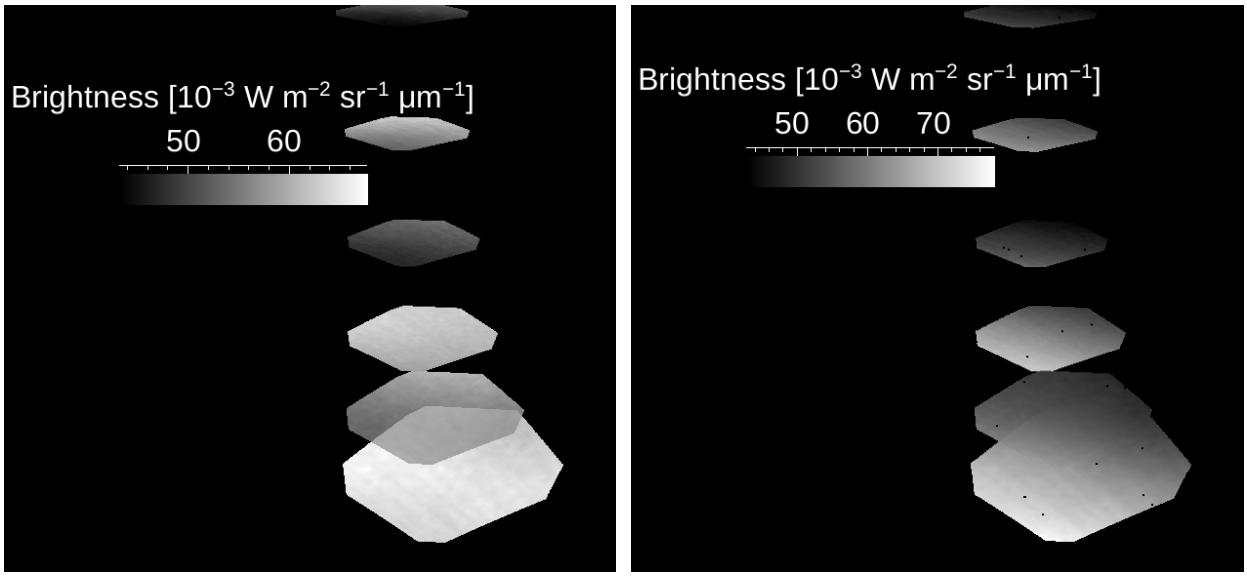

(a) Original (b) Corrected

Figure 2.27.: Original and corrected mosaics for orbit 0998

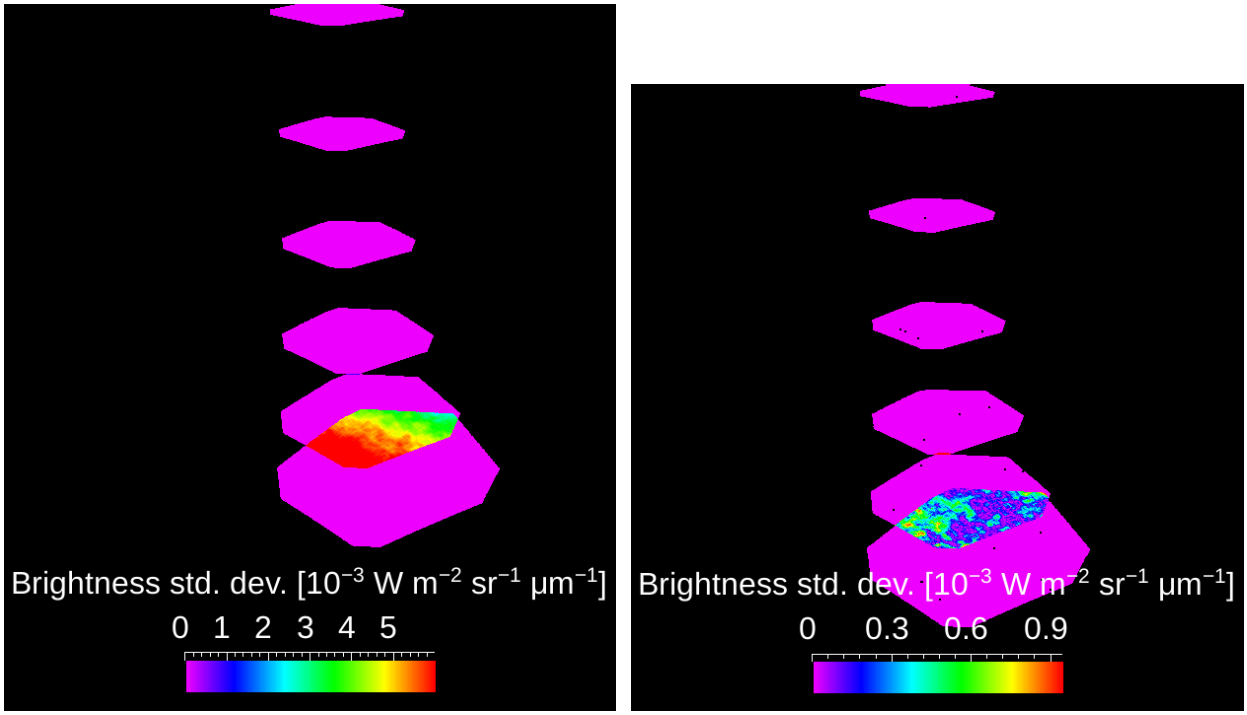

(a) Original (b) Corrected

Figure 2.28.: Maps of standard image to image deviation for orbit 0998

(a) Original (b) Corrected

Figure 2.29.: Original and corrected mosaics for orbit 2818

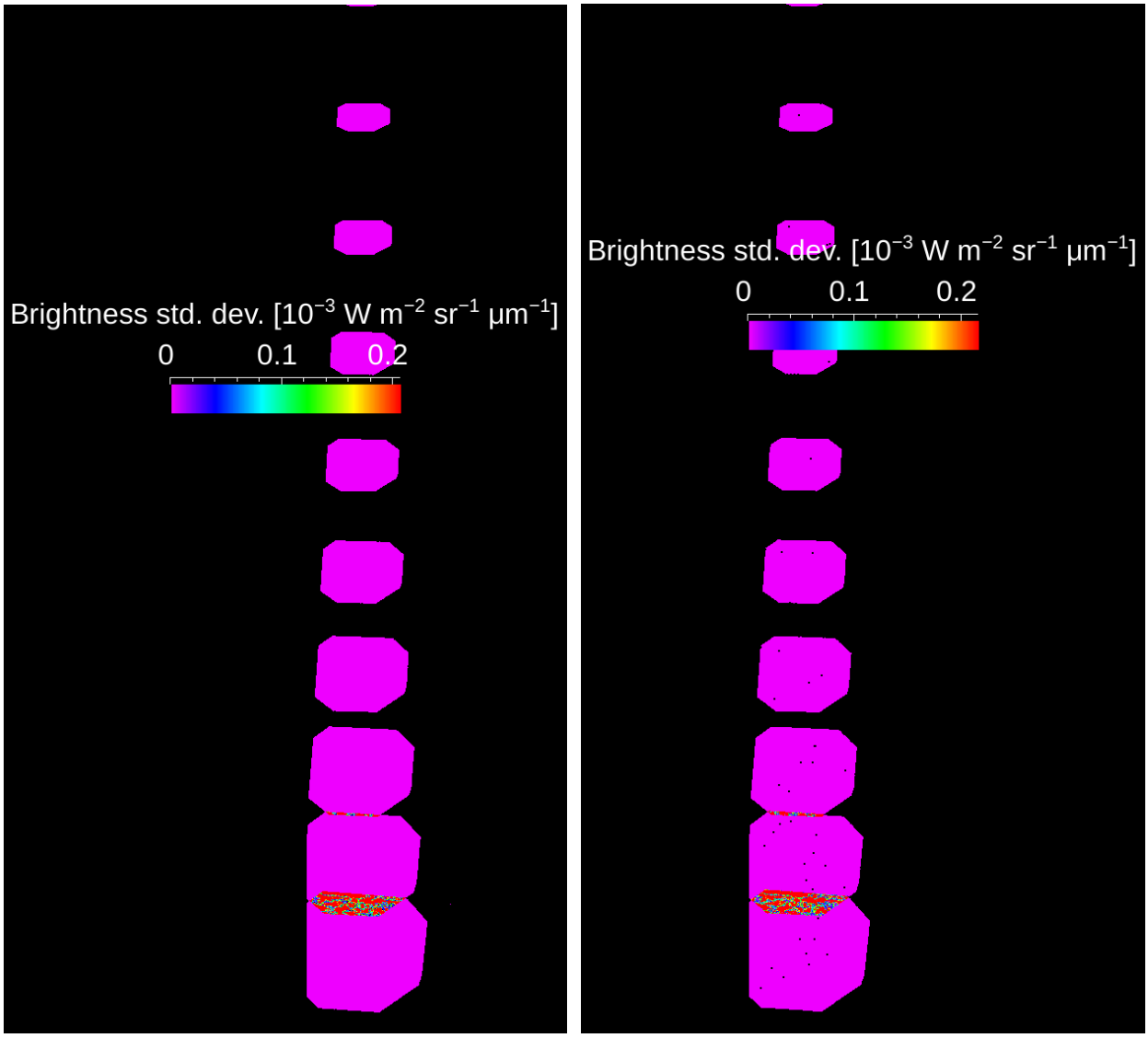

(a) Original (b) Corrected

Figure 2.30.: Maps of standard image to image deviation for orbit 2818

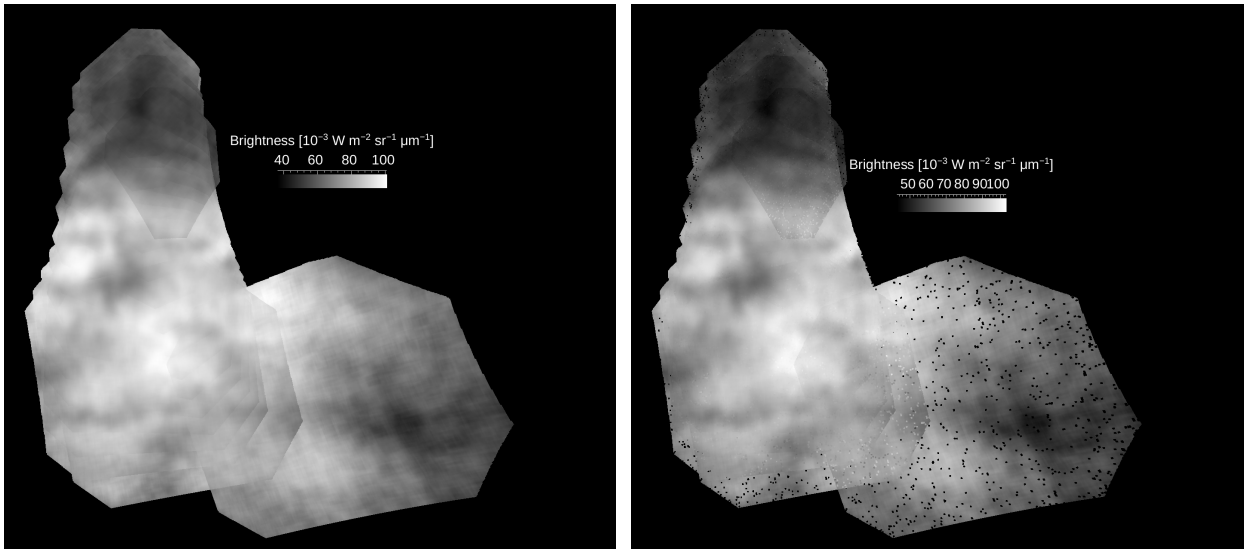

(a) Original (b) Corrected

Figure 2.31.: Original and corrected mosaics for orbit 0586

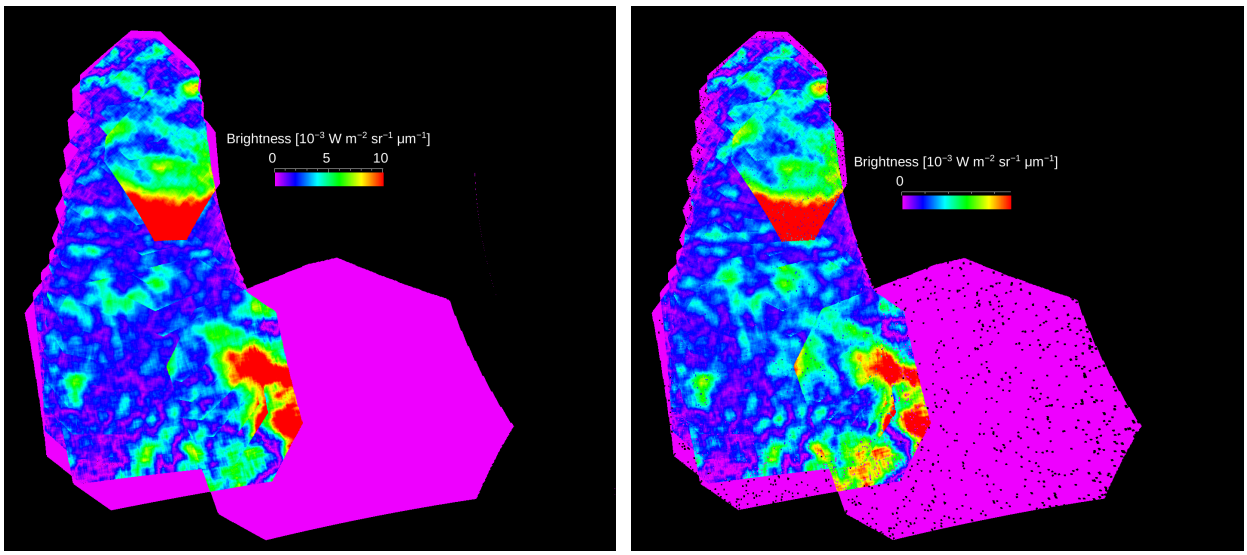

(a) Original (b) Corrected

Figure 2.32.: Maps of standard image to image deviation for orbit 0586

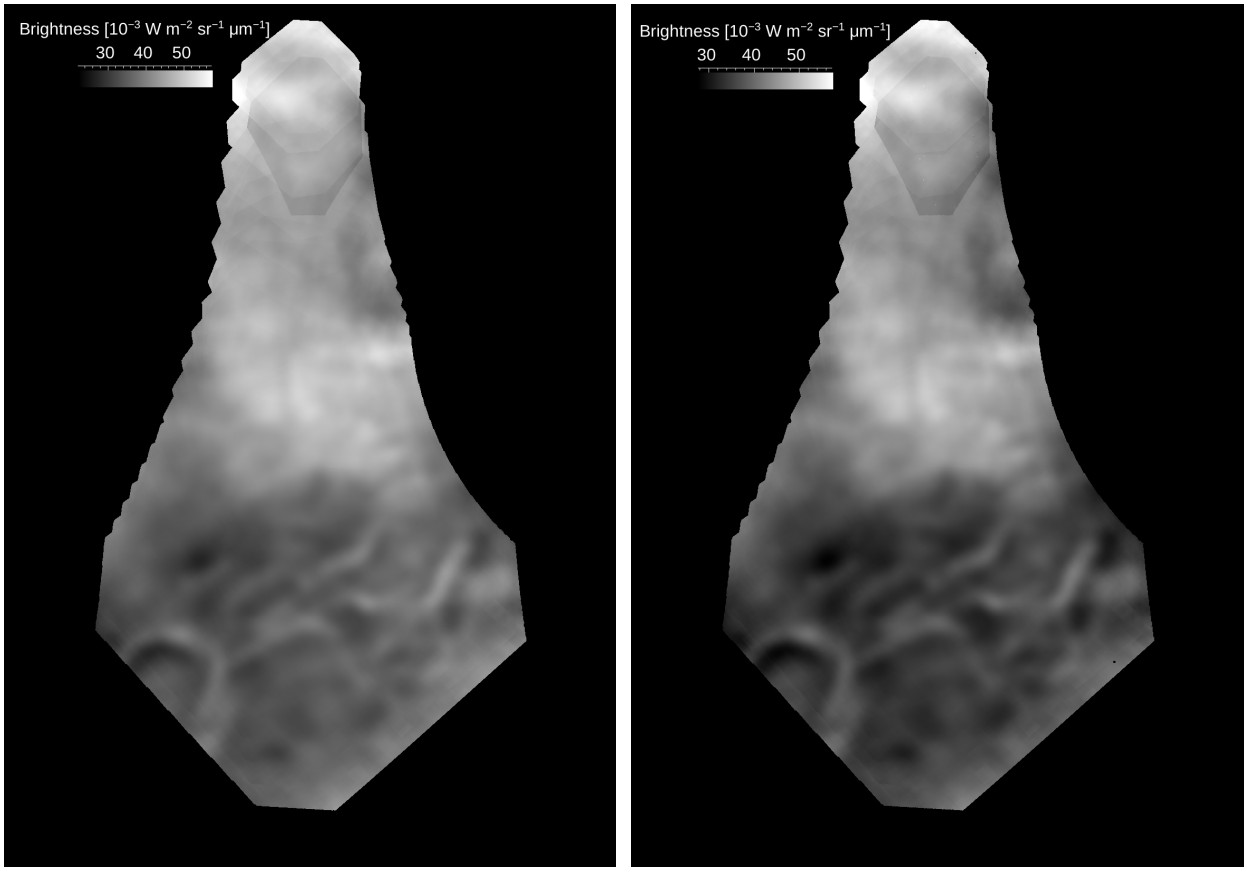

(a) Original (b) Corrected

Figure 2.33.: Original and corrected mosaics for orbit 1259

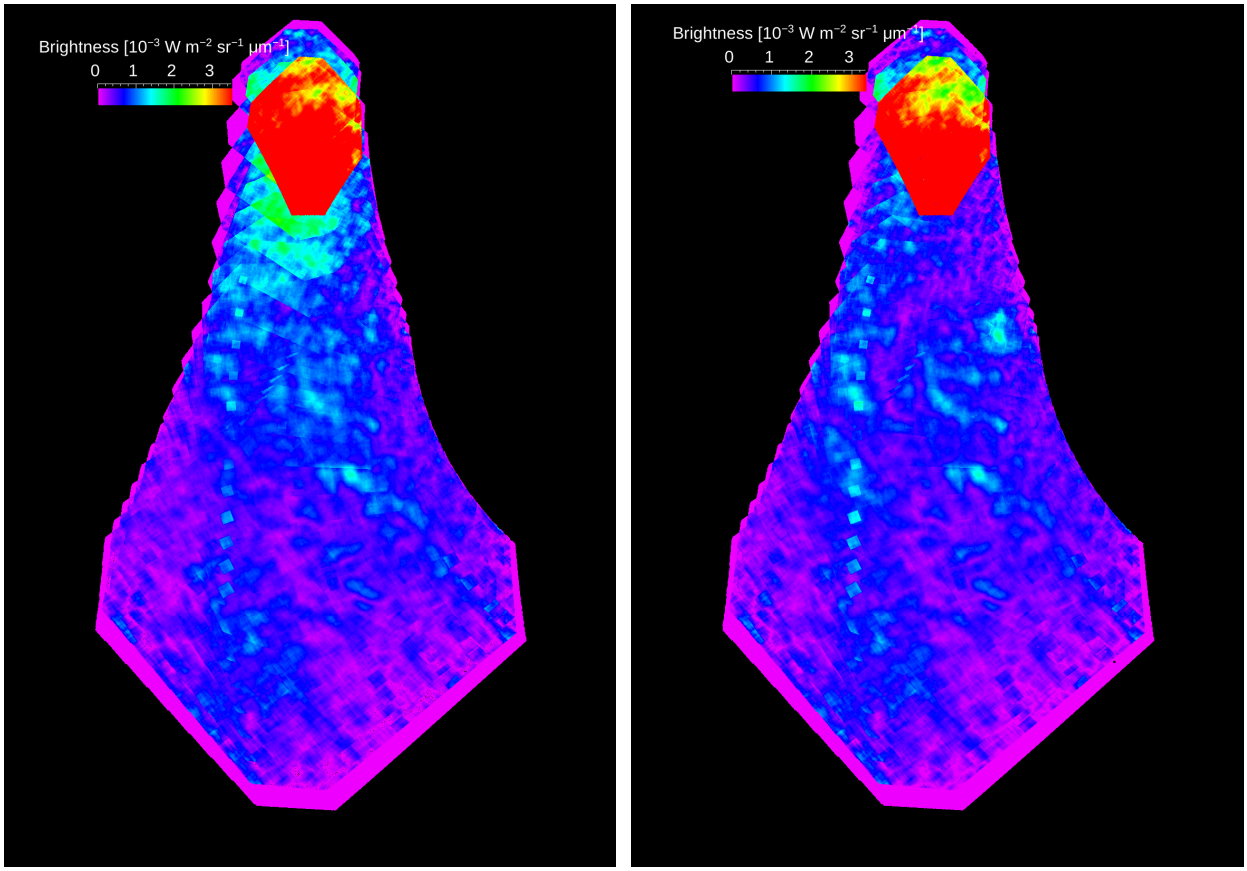

(a) Original (b) Corrected

Figure 2.34.: Maps of standard image to image deviation for orbit 1259

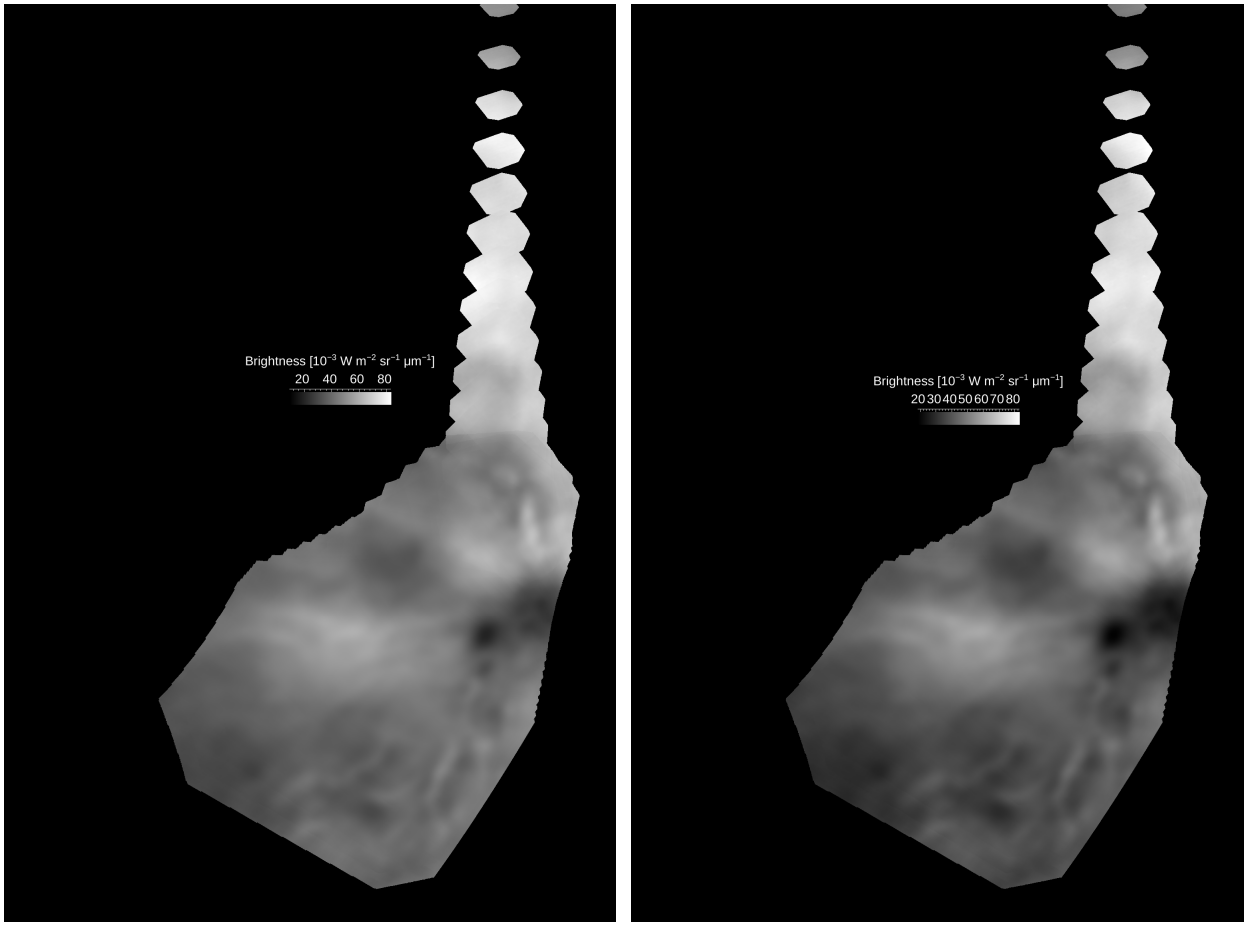

(a) Original (b) Corrected

Figure 2.35.: Original and corrected mosaics for orbit 1148

2.3.1.4. Artefacts of unknown nature

In 34 orbits we discovered strong image-to-image inconsistencies that are localised in the surface spatial co-ordinates. These phenomena could be caused by an unidentified processes on the surface or in the very low atmosphere, and in a few cases they coincide with detected volcanic activity event. These phenomena are actually an artefacts from the point of view of the automatic correction algorithm. The algorithm can't handle those images well, trying to eliminate the artefacts, which do not follow the pattern of the error in AFF. This results in the failures to wipe out the artefacts and to correct the AFF gradient. Likely, for all of such cases, the artefacts are localised and occupy less than ⅔ of the total mosaic, and we can perform correction using the remaining ⅓ or more (up to ½) of the mosaic. Therefore for each such case we set latitudinal ranges to omit the artefacts and used the rest of the mosaic surface in the regular way. That allowed to overcome the initial problem completely (figs. 2.37 and 2.38).

In this way we used only images that do not intersect the anomaly regions. That allowed us to achieve stable results in the anomaly-free regions and also make the anomalies more prominent.

2.3.2. Result of images correction

The correction was a linear surface with two parameters (gradients along the X and Y axes). The optimization was done using the Nelder–Mead algorithm, and the target function was the sum of image-to-image variances (*i.e.* the variance is computed only in the pixels where two or more images overlap). The target precision was set to $10^{-7} \times 512\,\mathrm{pix}^{-1}$. In most of the

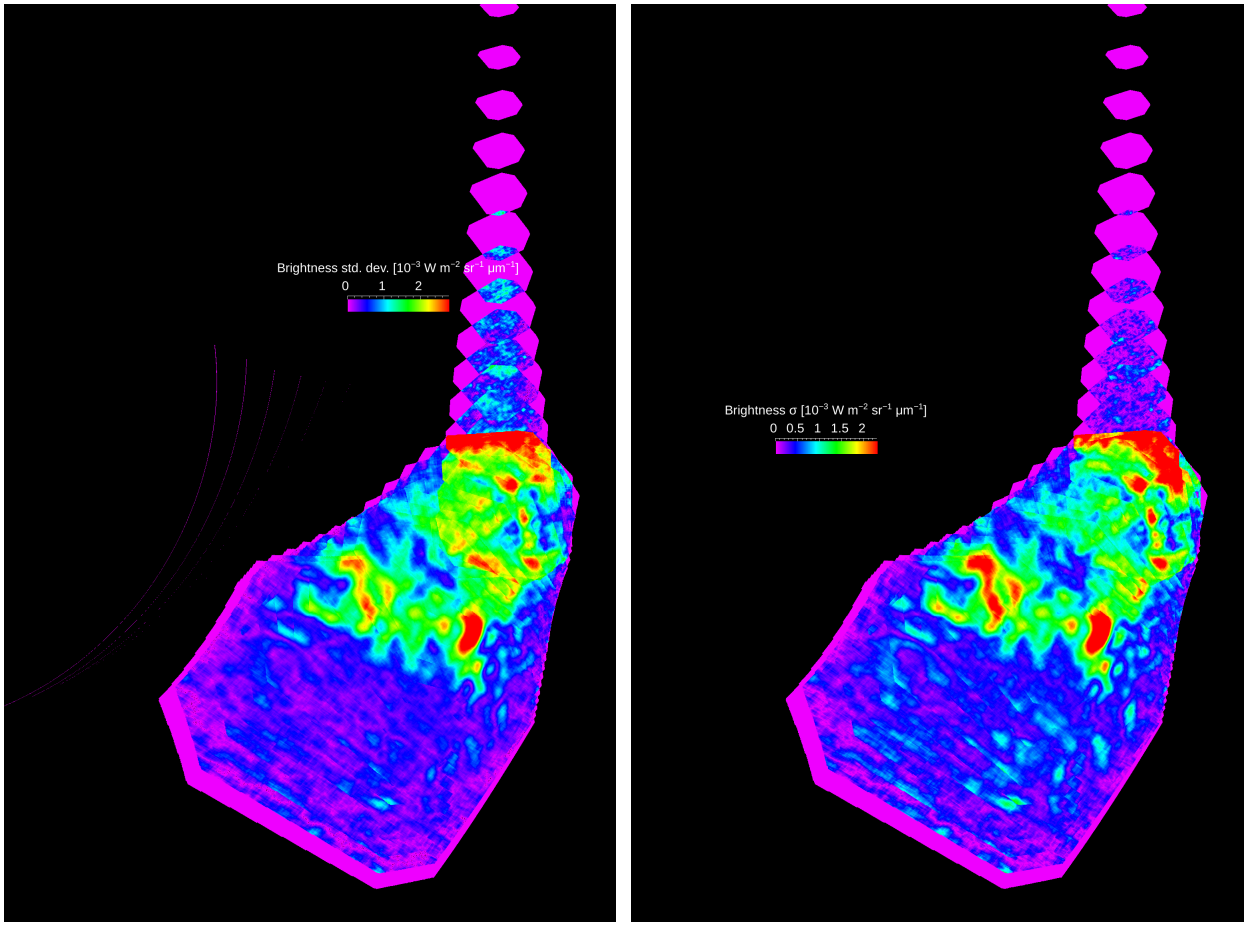

(a) Original (b) Corrected

Figure 2.36.: Maps of standard image to image deviation for orbit 1148

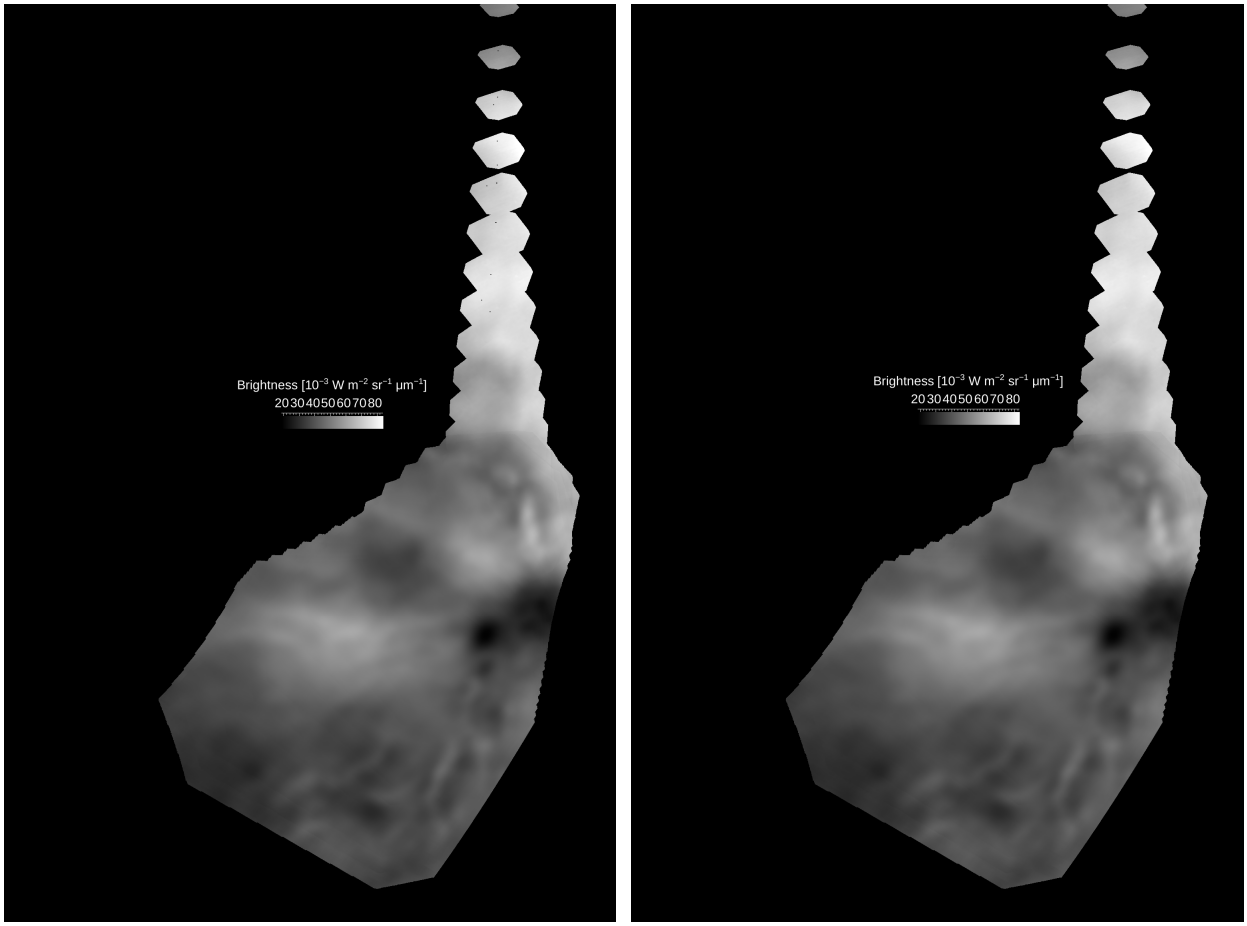

(a) Common correction

(b) Special correction

Figure 2.37.: Comparison for surface

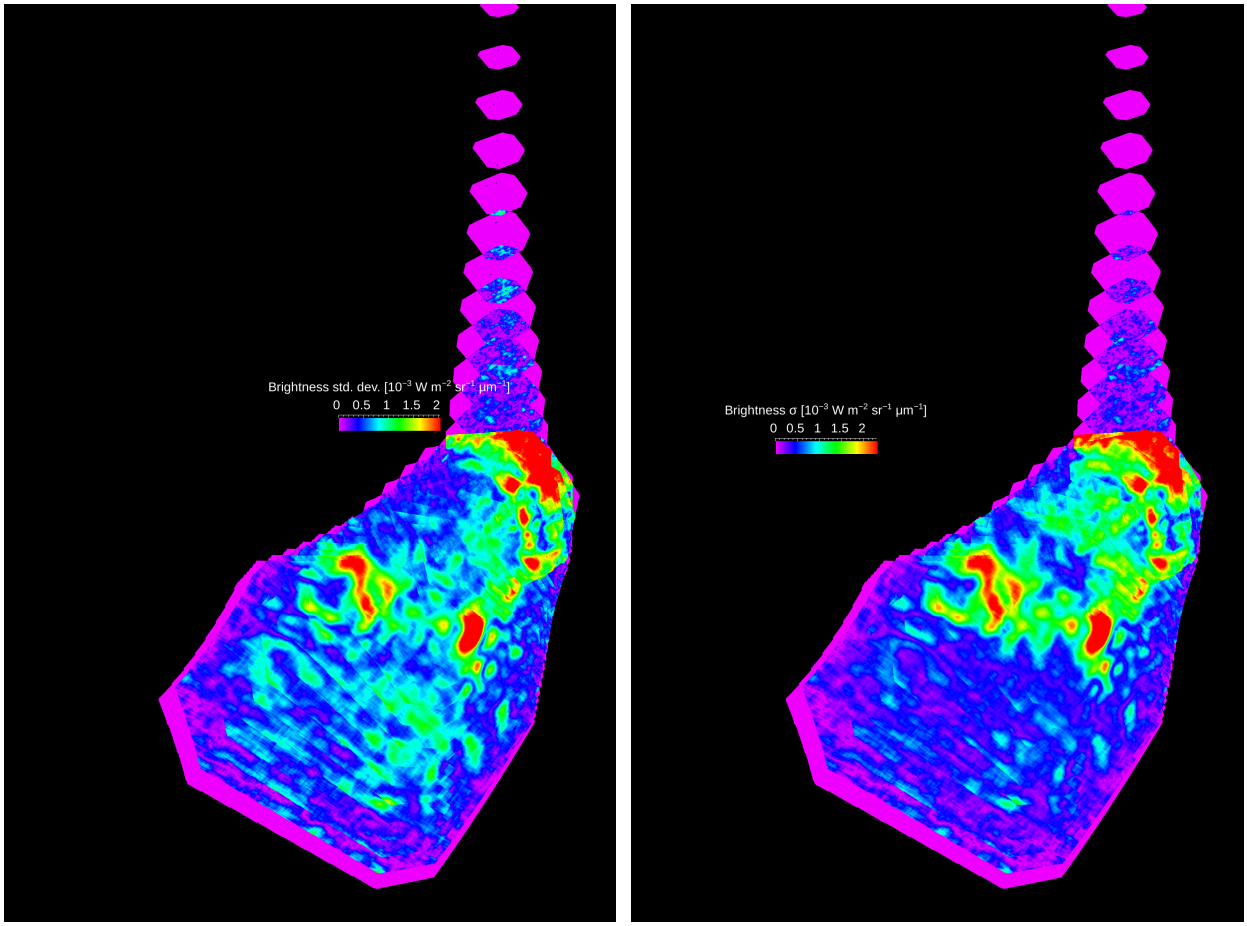

(a) Common correction

(b) Special correction

Figure 2.38.: Comparison for surface stddev

cases it took ~ 50 iterations to reach this precision (fig. 2.39).

The value under optimization (the sum of variances in overlapping pixels) hereinafter is called “inconsistency”, and the “inconsistency ration” if the ratio of initial to final (after the correction) inconsistencies. Maps of the variance are shown below and were used to identify some interesting cases.

For 450 orbits the automatic processing routine managed to decrease the inconsistency between the neighbouring images without introducing other problems described in section 2.3.1, see fig. 2.40.

For the rest of 93 orbits we used workarounds that allowed to put correction performance for them in line with the regular data. Figure 2.41 shows the distribution of the inconsistency ratios (a ratio between image-to-image inconsistency in the original data to the same inconsistency in the corrected ones) for the normal, clustered, and surface anomalies data. In terms of the inconsistency ratio, the semi-automatic procedure for the orbits with surface-related artefacts did not result in a ratio increase in all cases, but when the ratio improved, it improved greatly (fig. 2.42). In general, the correction quality seems not to be dependent on the initial inconsistency, that is illustrated by correlation diagrams in fig. 2.43. The inconsistencies themselves seem to be not tied to orbit numbers too: inconsistency on orbit dependence plots (fig. 2.44) show no strong patterns except the absence of high inconsistencies in orbits 2000 to 2800, which do not correlate with average temperatures.

The resulting correction gradients and their orientations are showed in fig. 2.45. The gradient value shows a hint of periodicity, but it is not connected to the Venus rotational period, which could be expected because of the repeatable observations configuration, but the gradient orientation (fig. 2.45b) shows a random distribution.

To further look into that we computed an average VMC night-side image and it is show in fig. 2.46 together with its standard deviation. The clear pattern in the image suggest that the actual flat field drifted from the laboratory one and it might had been stable enough during the mission to produce this kind of averaged image. This suggest that such an averaged image can be used to produce yet another additional flat field. Verification requires at least computing these averaged images for different parts of the data set in order to study its stability and is outside the scope of this project.

2.4. Summary

The goal was handle manually those cases (VEx orbits) where the automatic correction failed to improve the images. To achieve this goal we analysed images of the image-to-image deviation and mosaics themselves, selecting the orbits with non-standard observational conditions (*i.e.* that differ from a meridian-wise strips) and the orbits with unusual artefacts, localised in surface co-ordinates. For these special cases we found that

1. in the case of complex geometry observation for a given orbit, that results in overlapping clusters of images taken at significantly different emission angles, removing such images allowed to successfully apply the general correction algorithm to the rest of the data from the given orbit;

2. similarly, for the cases with surface-correlated artefacts selecting regions without said artefacts allowed to apply the correction, and, at the same time, retrieve much clearer picture of the artefacts themselves.

With that adjustments we were able to apply the software to the VMC night side data and obtain the following results:

1. 542 out of 622 VMC night side orbits were successfully corrected, decreasing the image-to-image discontinuity under normal conditions (as opposite to what is discussed below in item 3) to $1.5\,\%$ or less.

2. 80 orbits were not suitable for this type of processing because area of image intersections is too small or absent.

3. In 34 orbits we observed previously unknown artefacts, stable in surface co-oordinates, detectable as localised spikes in the maps of image-to-image deviations, reaching up to $5\,\%$ of brightness. This physical effect needs to be investigated in future, but is out of scope of this study.

4. We found that in a number of cases (roughly 50, but there is no a exact and precise classification criteria) the additional flat field were constructed from too noisy images and thus do not bear information to compensate for the camera damage, but instead they just add noise.

5. These noisy additional flat field not always associate with high CCD temperatures.

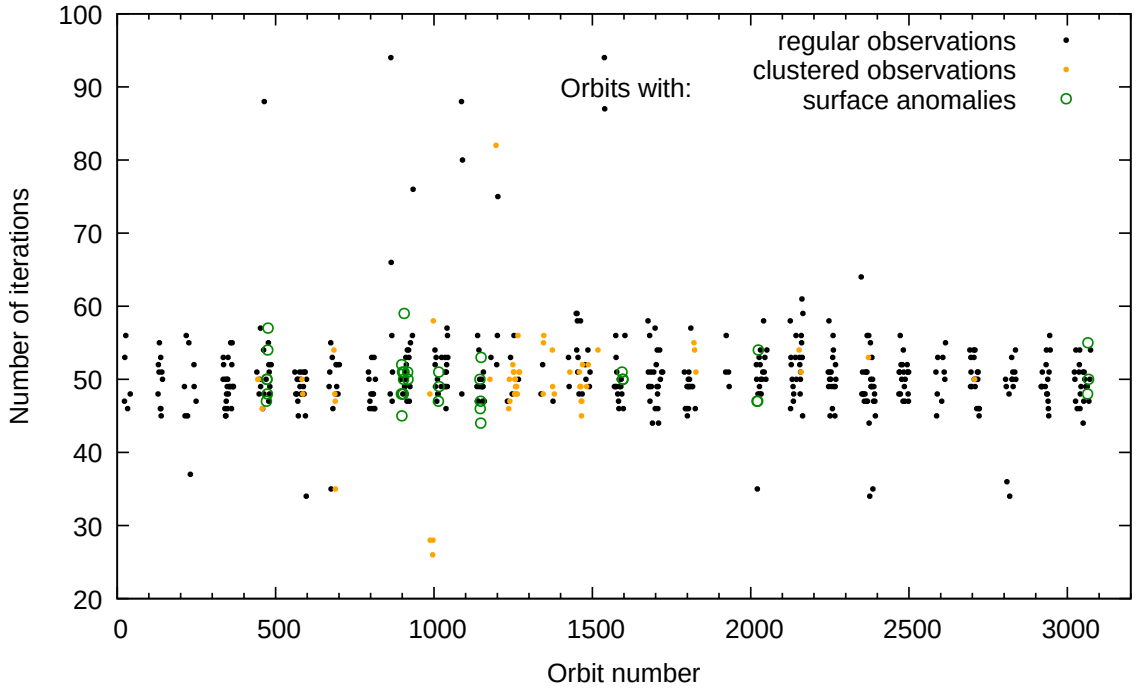

(a)

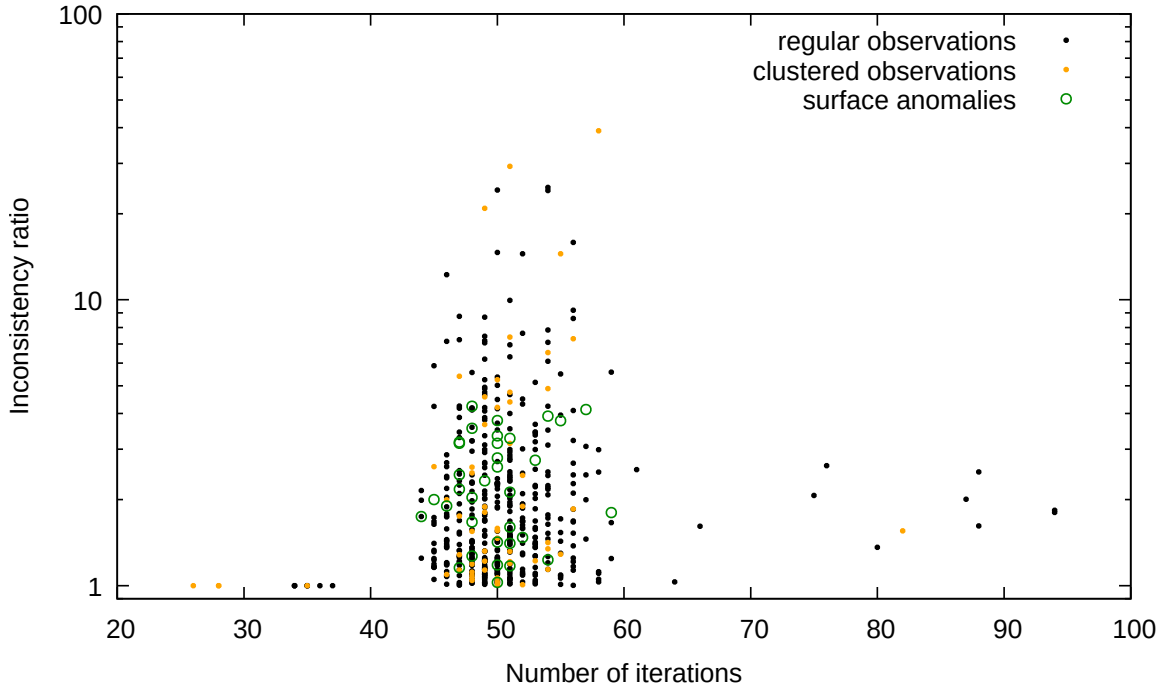

(b)

Figure 2.39.: Performance of the automatic correction procedure. Most of the orbits show consistent behaviour a, requiring about 50 iterations to reach the desired accuracy of the simple gradient fit. The similar can be said about the distribution of the final inconsistency ratios b

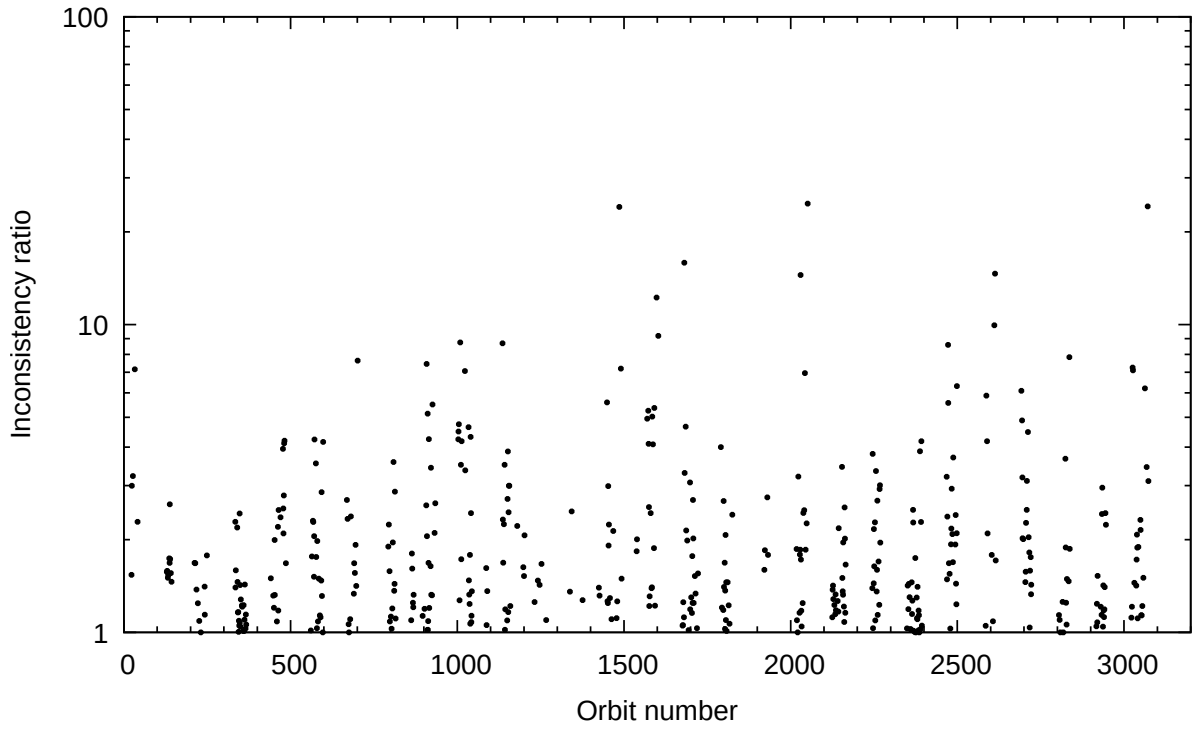

Figure 2.40.: Results from the the automatic correction procedure for 450 orbits that showed “normal” behaviour, visualised as the ratio between initial cross-image inconsistency and the inconsistency for the corrected images

6. There is no systematic trends found in the value and orientation of the linear gradient, which is the result of the correction procedure.

7. Average VMC night-side image show a picture of the CCD damage and might be used to correct images. That requires an additional careful investigation that is out of scope of this activity.

8. VMC re-calibrated night side data are stored on PSA Guest Storage Facilty GSF [7] and available for the download via FTP.

2.5. Data format and naming

The current ID of re-calibrated dataset is “VEX-V-VMC-3-RDR-SCP-V1.0”, where SCP = Surface and Cloud Properties (the name of the ESA granted project), 3 indicating the processing level of VMC data (3-RDR), and data stored on GSF [7]. The data set splitted to match the mission extensions, so the above dataset ID would be for the nominal mission phase, and, as example, “EX-V-VMC-3-RDR-SCP-EXT1-V1.0” is for mission extension 1 (see details in [30]). The format of the retrieved data archive is described in [30].

The data set consists of images in the PDS3 format (image files are uncompressed pixel arrays with attached labels in the PDS3 format) in files with the ”.img” extension, in-line with the format and naming of the historical Venus Express VMC data archive in the ESA Planetary Science Archive (PSA). The files can be read by any PDS3 compatible viewer (e.g. NASAView). Description of the metadata could be found in the standard documentation, *e.g.* the PDS objects and attributes used are fully compliant with the definitions given in the PDS3 reference (Appendices A and B in [20]) and the Planetary Science Data Dictionary [23]. Some details can also be found in this document in chapter B and chapter C.

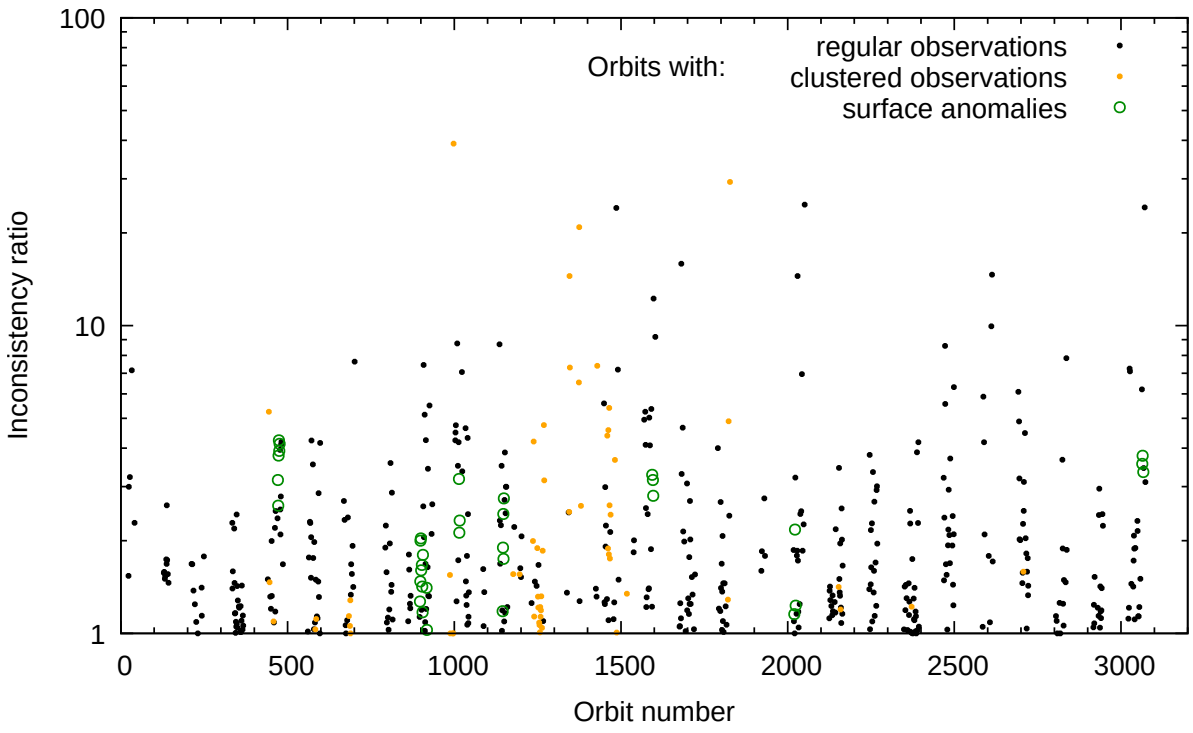

Figure 2.41.: Results from the the automatic and semi-automatic correction procedures for all the 622 orbits, visualised as the ratio between initial cross-image inconsistency to the inconsistency for the corrected images.

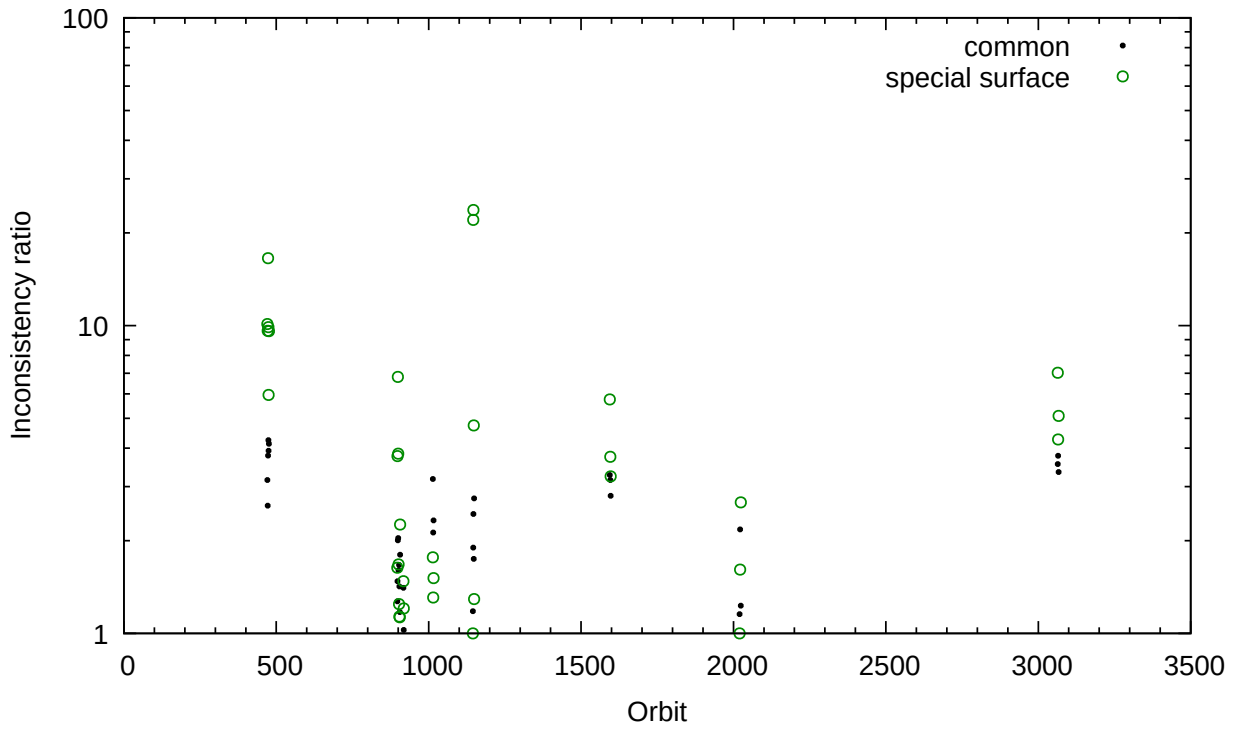

Figure 2.42.: Comparison of inconsistency ratios for orbits with surface-connected artefacts from the regular correction procedure and the correction in the artefact-free regions only

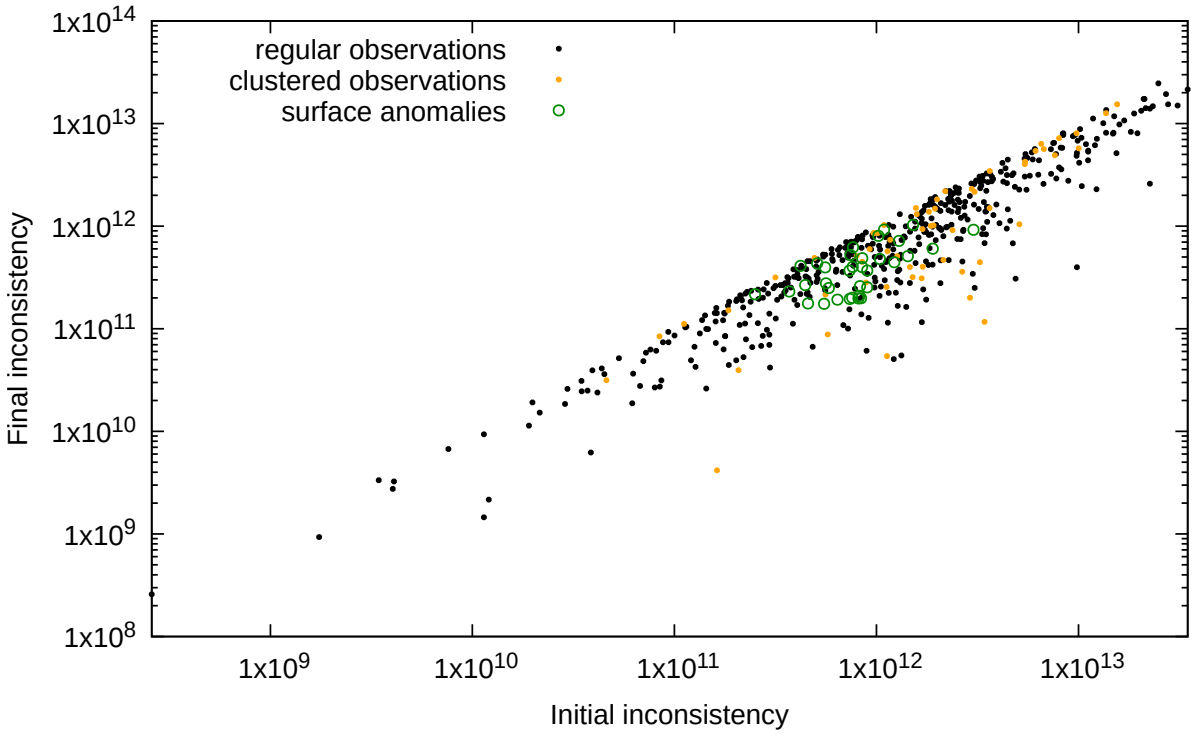

(a) Correlation diagram between the final and initial inconsistencies

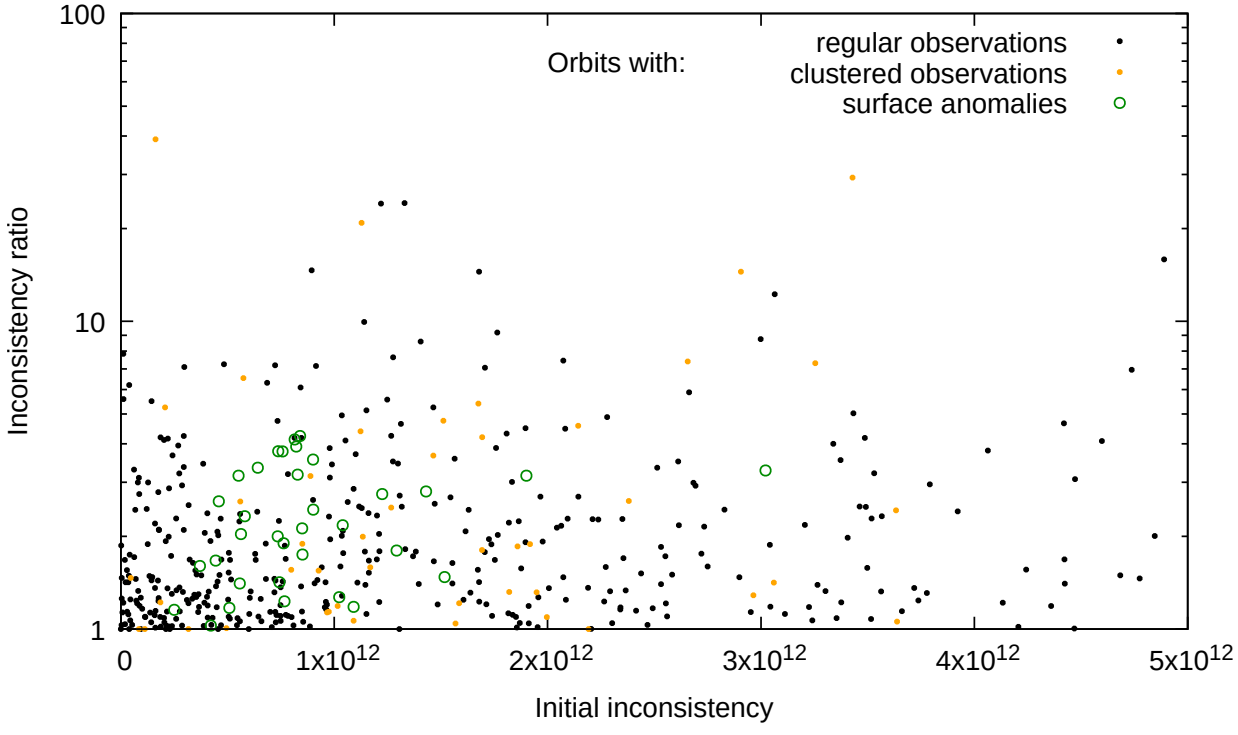

(b) Inconsistency ratio with respect to initial inconsistency

Figure 2.43.: Correlation diagram for the final inconsistency and inconsistency ratio with respect to the initial inconsistency. The diagrams show no correlation between the initial inconsistency value and the correction performance

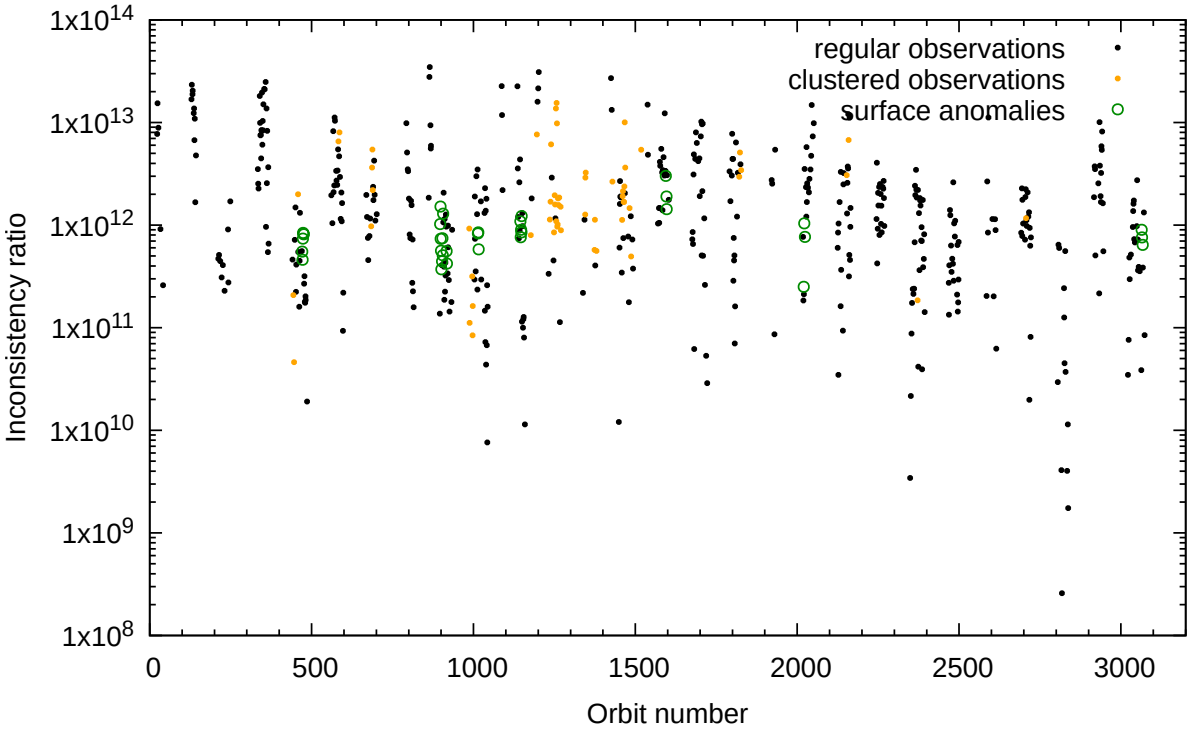

(a) Initial inconsistency for all orbits

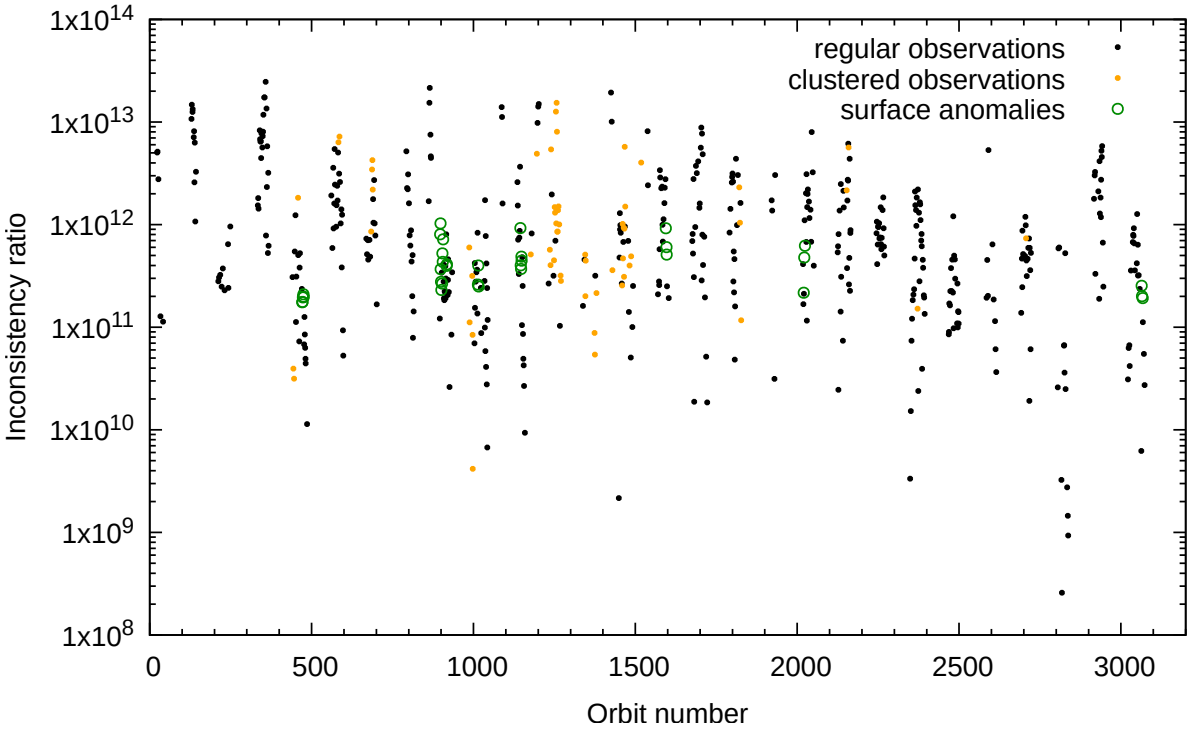

(b) Final inconsistency for all orbits

Figure 2.44.: Initial and final inconsistencies with respect to orbit number

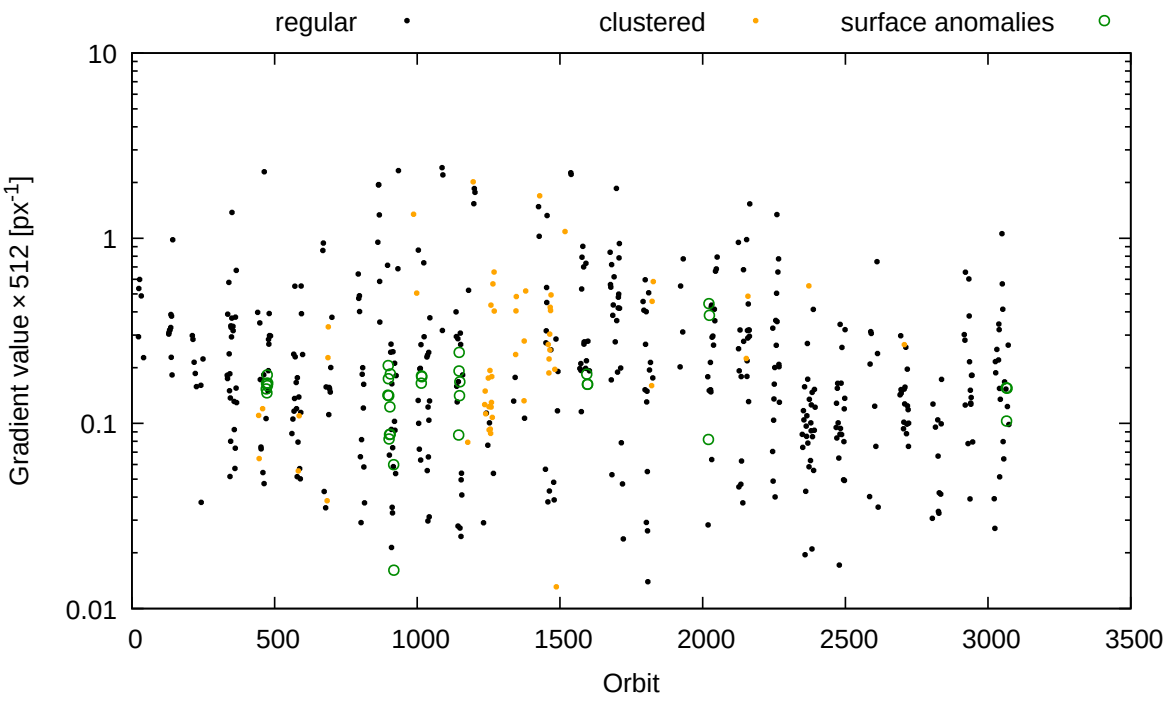

(a) Gradient value

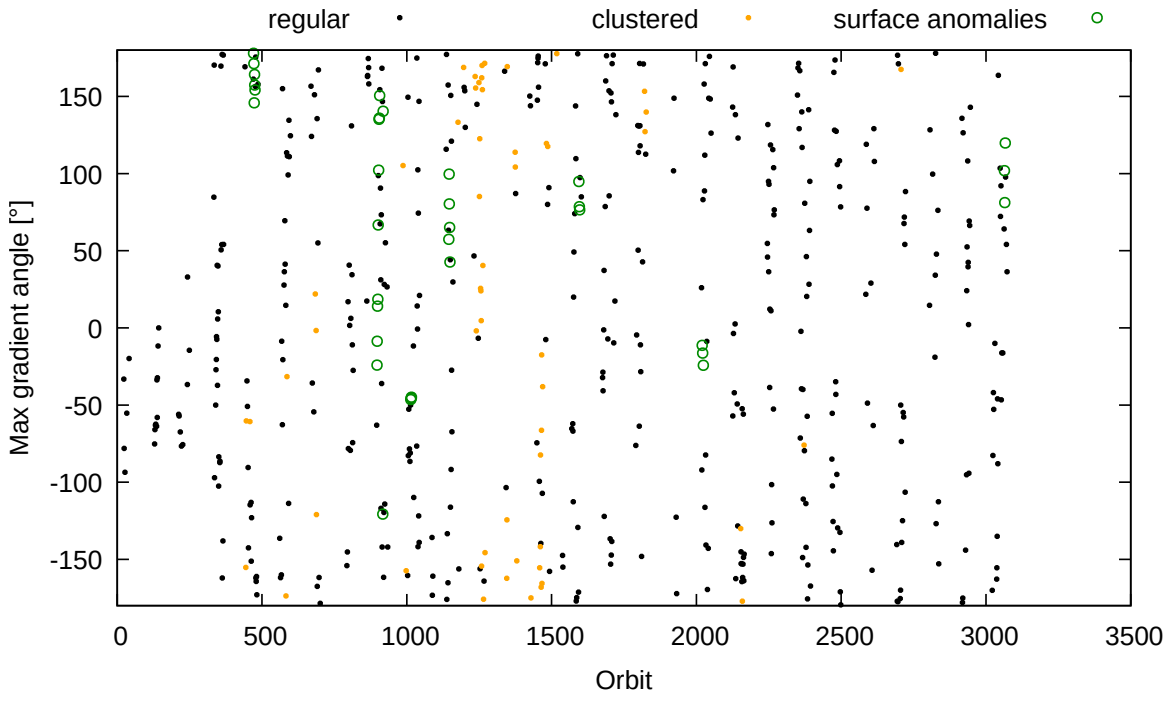

(b) Orientation

Figure 2.45.: Distribution of the AFF correction gradient over the orbit number a and the angle for the plane of the maximal gradient value b

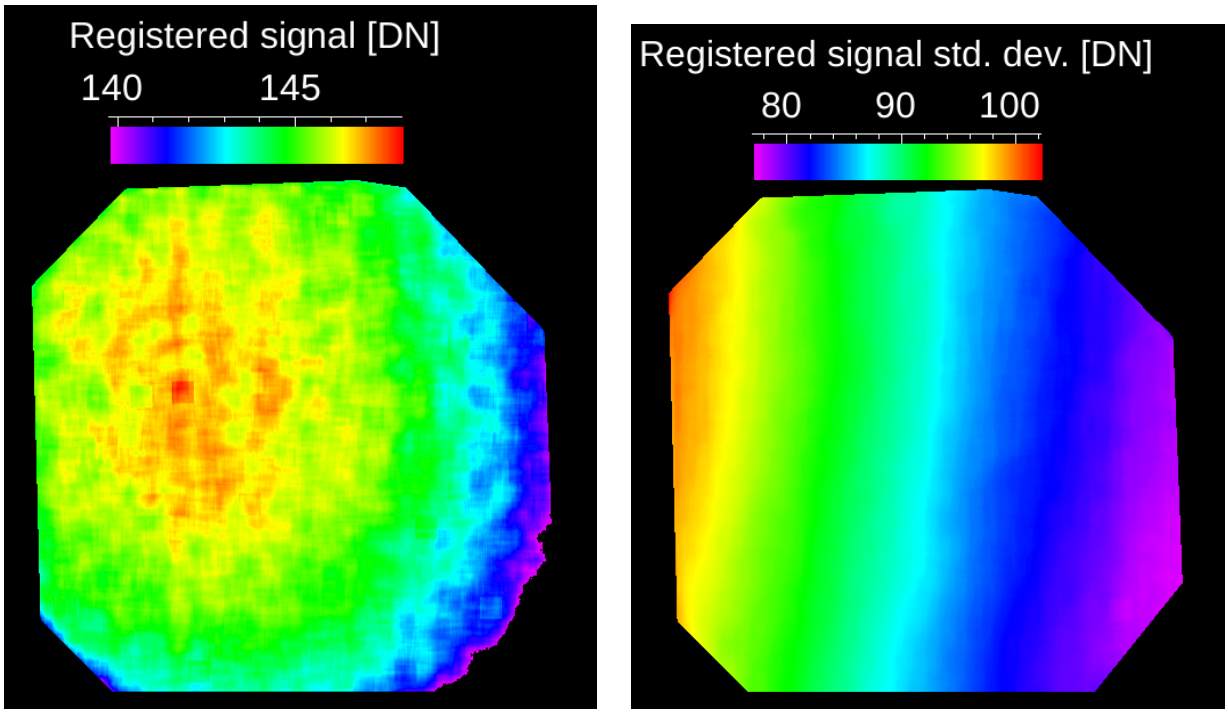

(a) (b)

Figure 2.46.: Averaged VMC surface image a and its standard deviation b composed from images after the low-pass filter used in this study to prepare images for correction

3. Producing segmented map of relative surface emissivity at $1\,\mu m$

3.1. Input data

The input data for this part of the project are the re-calibrated data set retrieved at the previous stage (see section 2.5).

3.1.1. Regional plains map

We have used the geological map from [14] provided us by M. Ivanov in form of image (not in ASCII form) in Mollweide projection (fig. 3.1b). All geological units has painted black-greyish borders besides the colour code that causing the problem to distinguish between them using the developed automatic procedure of plains decoding. Solution: selection of base plains from the map were done manually. For current study we decided to use as basic units the tree types of plains which were formed at the same geological period: regional plains (lower and upper units) and shield plains. We firstly selected only plains from the map by automatic way (see fig. 3.2a), and then manually carefully united the plains, removed black-greyish borders line and other kinds of geological units. We added the additional space between selected plains and Tesseras, impact craters and rift zones to be in a safety place since this regions could be theoretically changed from the time of Magellan mission on the base of which data the geological map was build. The resulted map of selected plains presented fig. 3.2b. Despite of a lot of time spending with this topic, such a method resulted to the most accurate selection suitable to our purposes. For further calculation we have re-projected this map from Mollweide projection to Mercator projection (see fig. 3.4).

3.2. Algorithms of Venus emissivity map producing

3.2.1. Multidimensional minimisation using individual VMC images

The method tries to adjust parameters of the atmospheric model to minimize divergence between emissivity values, computed for same reference locations from various VMC images. We work with data of low quality extracting information with lots of unknown variables, and a number of parameters need to be restored from the same measurement. As a result of the project, we should retrieve information about whether such a method (reference to geologically homogeneous objects) can be used to analyze data from planned missions, for example, observations to be made by VenSpec/EnVision. When there is no enough spectrum-spread measurements to restore all the properties of the atmosphere, required to perform radiative transfer modelling, an alternative approach, able to calibrate the atmospheric model right from the surface observations, would come of use. The algorithm components are following:

Input data: Individual VMC images.

Input parameters: model for latitudinal distribution of clouds, reference region and its average emissivity, model for temporal behaviour of the detector sensitivity.

Algorithm steps: fitting all the models, minimising deviation between retrieved and assumed average emissivity within the reference region.

Output data map of the relative surface emissivity, map of atmospheric opacity variations.

The advantages of this method:

- It gives the most accurate solution possible.

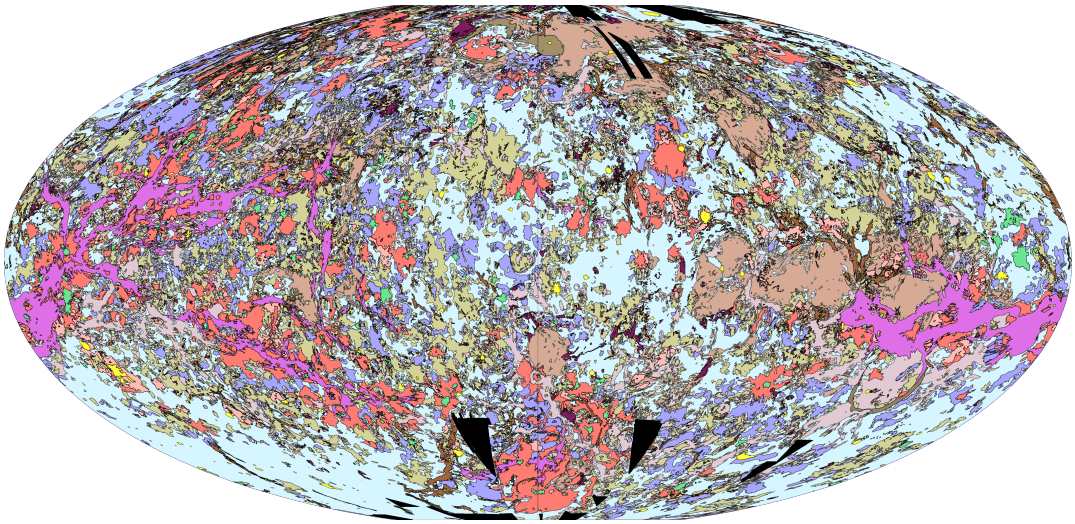

(a)

(b)

Figure 3.1.: Geological map of Venus in Mollweide projection retrieved from Dr. Ivanov [14]

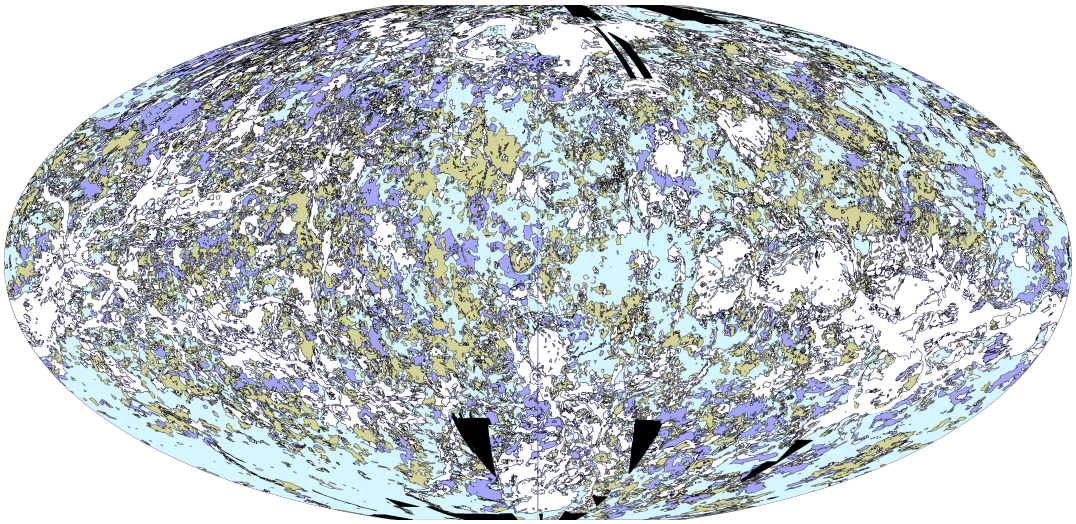

(a) Three kinds of plains marked with different colours

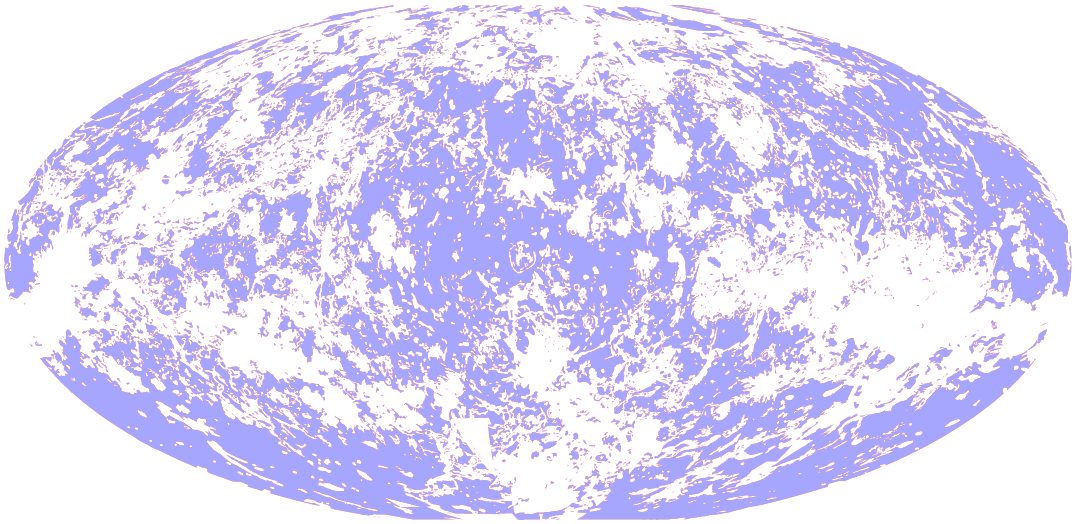

(b) Three kinds of plains merged together

Figure 3.2.: Selected plains regions from the geological map retrieved from Dr. Ivanov [14]. Mollweide projection

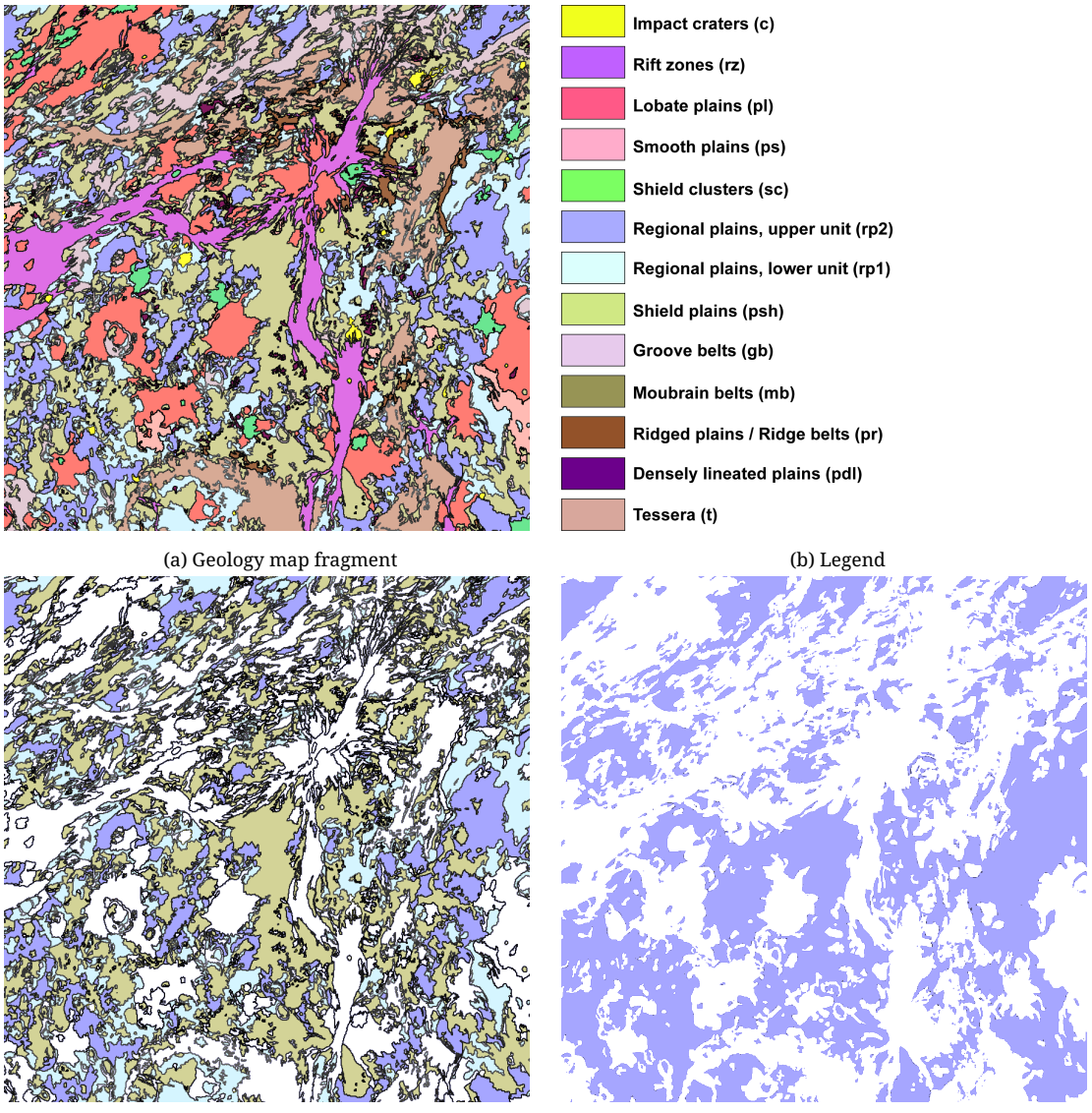

(a) Geology map fragment

(b) Legend

(c) Three plains fragment

(d) Joined plains fragment

Figure 3.3.: Demonstration of marked borders lines between the geological units. Geological map fragments for the same region in tree forms that demonstrate the original marks from [14], and processed by us data: only tree plains kind with mapped black borders came from original map (fig. 3.3c). Resulted merged plains with no borders lines shown at fig. 3.3d

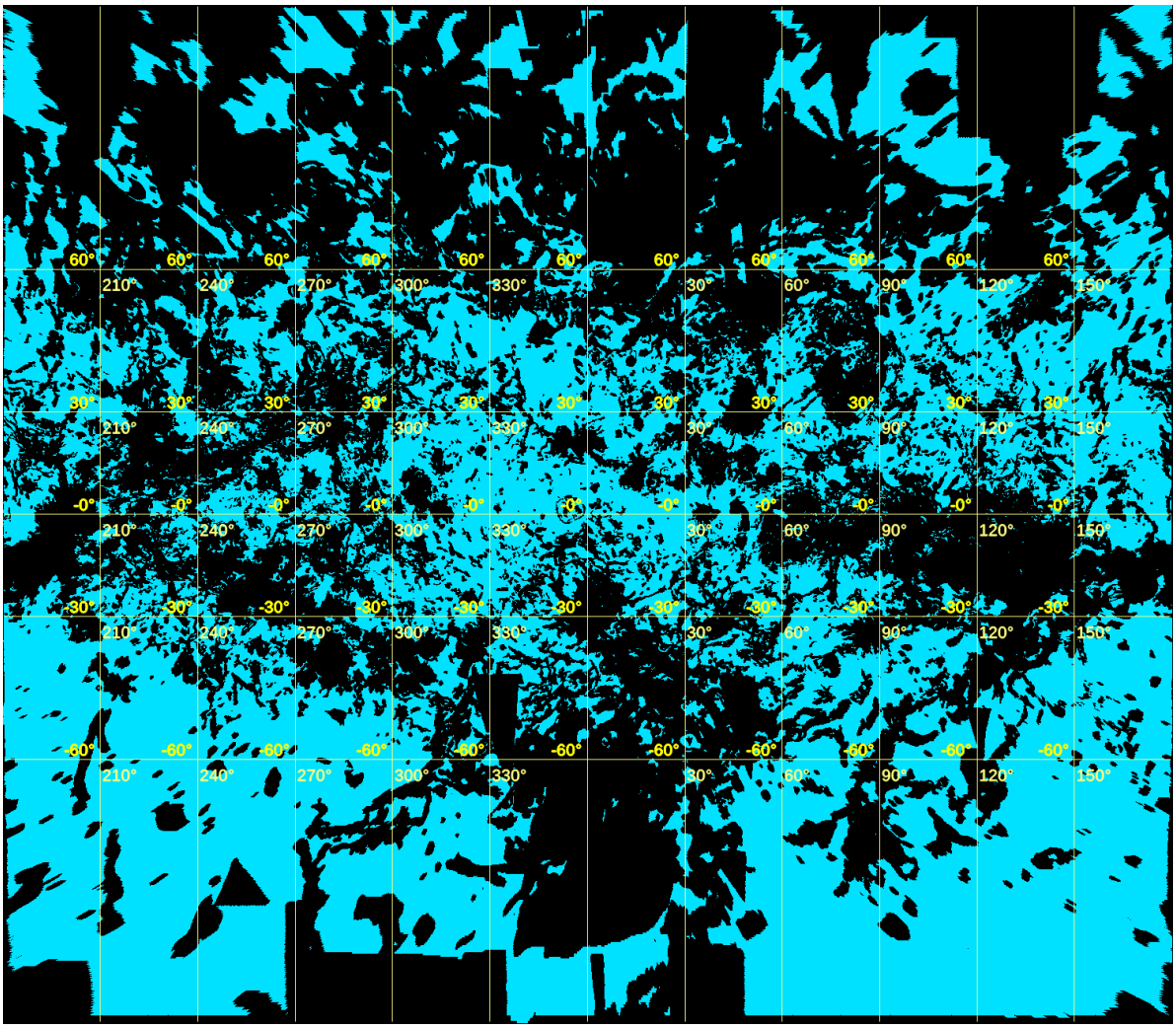

Figure 3.4.: Geology map of selected plains in Mercator projection

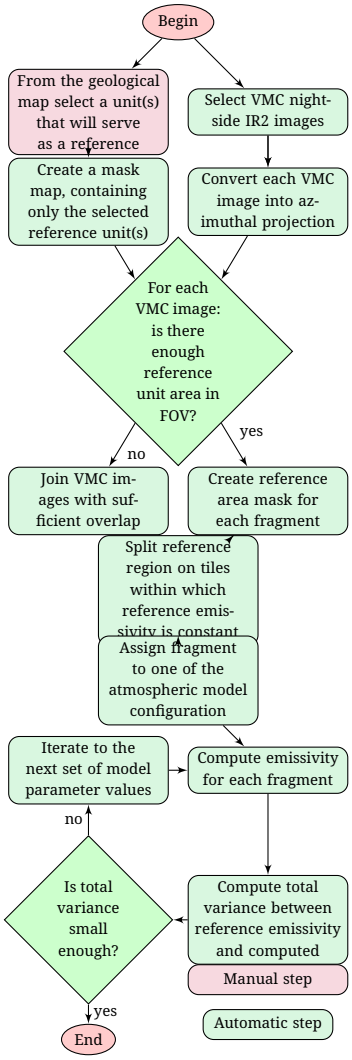

Figure 3.5.: General scheme of the emissivity retrieval with the multidimensional minimisation

- Simultaneously estimates variability of the cloud opacity.
- It should give an important conclusion for analysis of the future missions data: whether it is suitable to use the geological unit properties in when precise atmospheric model is not available and can't be deduced from the observations.

Limitations:

- This method is sophisticated and requires much computer power and to solve the technical tasks to speed up the calculations when searching for the solution of multidimensional minimisation

3.2.2. Stitching orbital-wise mosaics

Rather than fitting together individual VMC images, this method operates with mosaics, composed of (almost) all the VMC images from a given orbit. For each of these mosaics a map of relative surface emissivity is computed, and these maps are then stitched to each other. The stitching is done varying the value of the reference emissivity for each orbit, which change is attributed to the change in total extinction in the atmosphere.

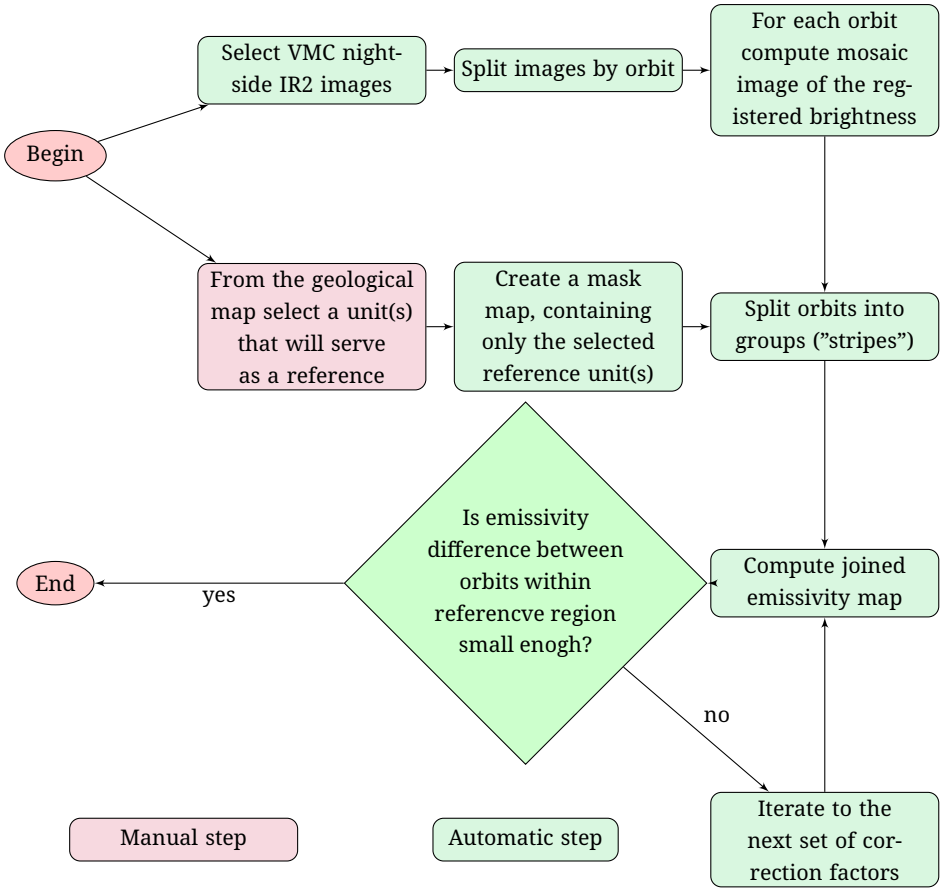

Figure 3.6.: General scheme of the emissivity retrieval via stitching the orbital-wise mosaics

Input data: Orbital-wise mosaics calculated from the re-processed VMC images.

Input parameters: atmospheric transmittance and reflectance, reference region and its assumed average emissivity

Algorithm steps: adjust registered brightness to minimize deviation between retrieved and assumed average emissivity in the reference region for each orbital mosaic, then stitch results together. The schematic algorithm is presented.

Output data map of the relative surface emissivity, map of atmospheric opacity variations.

It was planned to stitch as many as possible VMC mosaics together, until relative difference in surface emissivity between them exceeds the defined level of $10\,\%$. It was found, however, that the number of orbits that can be stitched this way, does not typically exceeds 5, and thus the total number of VMC orbits with surface observations (600) results in for up to 20 overlapping maps of the surface emissivity for a given point at the surface.

3.2.3. Stitching scaled orbital-wise mosaics and estimating the variability of atmosphere

To improve the situation we need to be able to stitch more orbital mosaics together, and decrease the total number of segments for the resulting map set. The main reason why the stitching does not allow to combine more mosaics is the change in atmospheric conditions between orbits. The changes are expected to be mainly driven by variability of the clouds, resulting in variability of their optical thickness. In the two streams approximation we use, that results in changes in atmospheric transmittance, reflectance, and the atmospheric point spread function. The changes in the transmittance and reflectance result in decrease of the apparent contrast with increase of τ, and increase of the point spread function size. Accounting for the point spread function changes is rather complex and is omitted.

Basing on the formulae for deriving reflectance and transmittance from average contrast ratio we can adjust contrasts in VMC mosaics (the emissivity retrieval method ignores the absolute value of brightness to overcome VMC calibration uncertainty) to relate them to a selected value of τ. That procedure yields average for orbit optical thickness difference and allows to match retrieved emissivity maps with higher accuracy then via adjusting the reference emissivity value.

Input data: Orbital-wise mosaics calculated from the re-processed VMC images.

Input parameters: atmospheric transmittance and reflectance values for a range of cloud optical thickness, reference region and its assumed average emissivity

Algorithm steps: adjust contrasts in the reference region to make them match atmospheric model with the lowest τ, apply the derived adjustment to the whole mosaics and use those adjusted brightness maps to compute surface emissivity, then stitch results together.

Output data map of the relative surface emissivity, map of atmospheric opacity variations.

3.2.4. Inhomogeneity of the $1\,\mu m$ surface emissivity of the regional plains

It was found that emissivity of basic surface — plains at different planets regions — varies for more than $10\,\%$. That was surprising since in radar wavelength all kinds of planes looks uniformly equal. What can be a cause for the apparent inhomogeneity of the $1\,\mu m$ surface emissivity of the regional plains, while their properties at the radar wavelengths are much more homogeneous? Indeed, at at $1\,\mu m$ we sound a few microns of the top layer. It is difficult to say for sure that this is a dust cover. It is probable there is a lot of fine micron-size particles on the surface. Another possibility is the chemical weathering layer. The chemical weathering affects several top microns, that most probable for nonporous material. But if the weathering leads to formation of phases (minerals), which specific density is different from that of primary minerals, this should produce microfractures that opens the way for the weathering agent to penetrate deeper and to work further. The observed emissivity anomalies could indicate age difference between units, similar to the analysis of VIRTIS $1\,\mu m$ images on Idunn Mons.

Sounding at radar wavelengths provides information about the layer which thickness of three wavelengths, that in case of Magellan is $30\,cm$ to $40\,cm$. The VMC sounding provides information about several μm thick layer. It shows presence or absence and amount of the surface dust which is quite movable by movements of the near-surface air. Photometers of the Venera-9 and Venera-10 landers registered slight change of illumination which was interpreted as dust uplift due to air perturbance by the landing spacecraft and rather fast sedimentation of this dust. Comparisons of TV images of some part of the Venera-13 lander taken subsequently in time showed gradual disappearance of dust initially seen on this lander part. So, one may expect rather inhomogeneous distribution of dust on the Venus surface changeable in time.

3.2.5. Changing the approach to building the regional emissivity maps

Due to the complications appeared during the work that caused changing the planned scientific approach to a more sophisticated one, and due to a failing in retrieving the results by this method to date of last ESA-MPS meeting (November 22, 2022), taking into account the project closure delay, it was proposed that instead of global map, the regional maps of surface emissivities for groups of orbits could be produced. These would be fairly self-consistent, although it was noted that between such orbit groups, there would still be variabilities that are not linked to emissivity variability but would be due to cloud variability and/or instrument degradation. Such kind of geological maps could be still in high demand of interest and could be useful for comparative studies of various geologic units: volcanic plains and flows v.s. tessera, among different units of volcanic plains, among different volcanic flows, radar-dark haloes v.s. their surroundings, to search for differences in IR emissivity within the same geologic units as a function of altitude.

Results retrieved for segmented regional emissivity maps are described in section 3.4 and stored at PSA Guest Storage Facility and could be downloaded via FTP.

3.3. Common part of the algorithm of relative surface emissivity calculation at 1 µm

3.3.1. Method of emissivity map retrieve

Emissivity is an important parameter characterizing composition and morphology of the surface. For geological analysis of the VMC images we will deduce and compare emissivity values ε of two given regions (points). To simplify matters, by "emissivity" we will mean the ratio of thermal flux from the point of the surface to the flux from a black body having the temperature of the atmosphere at given altitude:

$$\varepsilon = \frac{I}{I_P}, \tag{3.1}$$

and

$$I_P \propto \frac{2hc^2}{\lambda^5} \frac{1}{e^{\frac{hc}{\lambda kT}} - 1},$$

where h — Planck constant, T is the absolute temperature, λ is the wavelength of emitted radiation, k is the Boltzmann constant, and c is the speed of light. In case of thermodynamic equilibrium between the surface, the atmosphere, and their thermal emission, ε from eq. (3.1) is the true emissivity of the surface. Any of the descent probes and landers had not observed any hazes near the surface. Presence of the haze would be a sign of turbulence and absence of thermodynamic equilibrium. In the special case of presence of a fresh hot lava spot on the surface, there is no such an equilibrium, naturally. But since we do not want to determine emissivity of the lava, but want just detect high flux, this is not a problem.

Brightness in the VMC night-side images depends on

1) temperature of the surface,
2) emissivity (and reflectivity) of the surface,
3) extinction and scattering in the atmosphere, and, naturally,
4) how the camera transforms illumination intensity into images.

To deduce emissivity value from the brightness, it is needed to measure or model all the other effects and quantities. It is believed that the temperature in the lower atmosphere changes only with altitude, and does not depend strongly on spatial coordinates [28]. Thus, altitude maps are needed for the analysis. Extinction and scattering in the atmosphere can be modelled and scaled to fit observations (section 3.3.1.1). However, atmosphere parameters obtained for one region must be applicable to other points. To achieve that, optical properties of the atmosphere shall not change significantly between the given point and reference area. The most variable parameter (in both time and spatial dimensions) is the optical thickness of the clouds. The typical wind speed at the level of lower clouds (the most optically thick ones) is hundreds meters per second. Thus, one can expect that if there are no changes in the total clouds optical thickness between two consecutive VEx orbits (24 h) there are no changes on spatial scale of ~ 1000 km also. Since the plane of every next VMC orbit is shifted by $\approx 1.5°$ of longitude to the previous one, the images from these orbits significantly overlap. For mosaics in the same projection the surface features are in same places and thus all contrasts on images of their ratio are due to changes in atmospheric properties.

3.3.1.1. Radiative transfer in the Venus atmosphere

On its way to the camera through the atmosphere the light is affected by absorption and scattering, caused by gas (especially by the dense hot one in the very lower part of the atmosphere) and by particles in clouds and hazes. Absorbed energy, naturally, is emitted by the absorbers back into the system. However, temperature of cloud particles is 100 K to 200 K and thus their emission at 1 µm is negligible. The temperature of gas in lower atmosphere is the same as that one of the surface. But the density of the gas is not high enough to produce a continuous spectrum. Thus, emission in transparency "windows" is weak. Scattering occurs from particles in the clouds (hazes) and from density fluctuations and molecules in gas. Both scattering processes do not change the wavelength.

In the 1-µm transparency "window" the light travels through gaseous lower atmosphere with $\tau \approx 1.3$ [17], and then through the clouds with $20 \lesssim \tau \lesssim 40$ [38]. Unfortunately, transparency "windows" are not free from absorption completely:

far wings of the CO_2 and H_2O absorption bands are strong enough to be seen in the very low, dense and hot part of the atmosphere. It is extremely complicated to measure this absorption in the far wings in a laboratory. Known estimates are not accurate enough, and the amount of the absorption has to be determined from the NIR observations itself [like in *e.g.* 9].

In principle, it is possible to perform radiative transfer modelling for geometry of a given VMC image. Results of the modelling might be compared with the image. However, direct modelling of each VMC image is very time consuming. In addition, signal-to-noise ratio (SNR) of a single image is low. Thus, results of the modelling has to be compared with the VMC surface mosaics. It is not obvious, however, how to perform modelling for mosaics' geometry. As such, the following simplified model was used. As observations in nadir geometry are used, approach with point spread function can be used. Let us note, that this approach is applicable only if radiation flux on top of the atmosphere is orthotropic. One can naturally expect this from such a optically thick atmosphere. This point spread function describes atmospheric blurring. Let's construct our model from the following processes: *1*) absorption in lower atmosphere; *2*) scattering in lower atmosphere; *3*) reflection (mainly from clouds) back to the surface; *4*) reflection from the surface; *5*) scattering and absorption in clouds and hazes. To model item *1* approach, that will be described in section 3.3.1.2, is used. To model items *2* and *5* and to get a reflection coefficient of the atmosphere for the radiation coming from the surface (item *3*) the Monte-Carlo based radiative transfer (RT) code is used (see section 3.3.1.3). For item *4* Lambertian law is used and albedo $a = 1 - \varepsilon$ approximation is used, that is true in case of thermodynamic equilibrium between the surface and radiation field. Reflections between the surface and the atmosphere (items *3* and *4*) are modelled using two-stream approximation.

Assuming that both surface emissivity and atmospheric transmittance do not strongly vary within the scale of point spread function[1], emission intensity at a point with horizontal coordinates (x, y) at the top of the atmosphere can be expressed by the formula:

$$I(x,y) = \frac{t(x,y)\varepsilon(x,y)}{1-(r(x,y)(1-\varepsilon(x,y)))} \cdot \\ \cdot \iint B\left[T_S(x',y')\right] \cdot F(x-x', y-y')dx'dy' \tag{3.2}$$

where $t(x,y)$ is the atmospheric transmittance, $r(x,y)$ is the atmospheric reflectance of surface radiation in backward direction (both depend on surface altitude), $\varepsilon(x,y)$ is the emissivity distribution of Lambertian surface, $B(T_S)$ is the Planck function of the surface temperature T_S, and F is the blurring function. In this formula the two-stream approximation is applied to a single layer atmosphere to account for attenuation; convolution with the blurring function describes smoothing contrasts. We note that both atmospheric transmittance and reflectance depend on surface topography. Mueller et al. [18] used a similar approach to analyse the VIRTIS surface images. The model surface temperature is equal to that of the atmosphere. The temperature in the lower atmosphere is assumed to have adiabatic lapse rate of $\approx 8.1\,\mathrm{K\,km^{-1}}$ [29].

3.3.1.2. Light absorption in Venus atmosphere

Since surface altitude variations (several km) are comparable with the atmosphere scale heigh, gaseous absorption changes significantly for landforms at different altitudes. Topography related variations of the atmospheric absorption we include in the transmittance t (eq. (3.2)). For a particular surface point we can express corrected coefficient t as $t_0 \cdot k_a e^{kH}$, where H is surface altitude.

To calculate gaseous absorption, we used approach as in Ignatiev et al. [11] (that uses the same form-factors for line wings as in Meadows and Crisp [16]). Radiative transfer model for these calculations is based on the DISORT code [34] and line parameters from the preliminary version of the Carbon Dioxide Spectroscopic Database (CDSD) for Venus, the CO_2 high-temperature database, and high-resolution transmission molecular absorption database (HITRAN). More detailed description and references are given in Ignatiev et al. [11].

Since there is no reliable information on absorption in the far wings of CO_2 and H_2O near $1\,\mu$m under Venus conditions (high temperature and pressure) there is no possibility to do precise enough calculations of the absorption coefficient. In our case computation gave $k_a = 1.0034$, and $k = 0.0317\,\mathrm{km^{-1}}$. Emissivity, obtained with these parameters and adiabatic lapse $-8.1\,\mathrm{K\,km^{-1}}$, shows linear correlation with altitude, that does not look realistic. Therefore the value of k was adjusted to achieve absence of correlation for plains terrains ($\approx 0.12\,\mathrm{km^{-1}}$).

[1] The full width of the point spread function at half maximum is ~ 100 km as it will be discussed below

3.3.1.3. Light scattering in Venus atmosphere

The optical thickness of the Venus atmosphere is 20 to 40 and scattering results in intensive blurring. From the numerous experiments on-board descent probes and from other observations it is know that cloud particles are sulfuric acid droplets. Their refractive index and size distribution are know quit well. All this makes possible precise modelling the scattering from these aerosols.

Naturally, there have to be time and spatial variations of clouds properties. The most significant ones take place in the lower clouds. Optical thickness of the clouds τ is much greater than 1 and therefore expected variations of τ do not change the width of the point spread function significantly. But changes of τ lead to changes in t and r (eq. (3.2)).

Since we adjust t for account the gaseous absorption, exact value of t is not that important. But uncertainties in r are not compensated in that way. We can not retrieve τ from observations. Differences in the out-of-the atmosphere flux in model, described by eq. (3.2), are negligible for τ values within the range 20 to 40 (around $1\,\%$).

We use the vertical structure of clouds and their optical properties from Tomasko, Doose, and Smith [38], Henyey-Greenstein phase function with asymmetry parameter $g = 0.78$ and single scattering albedo $w_0 = 0.9995$, and optical thickness for the Rayleigh scattering in the lower atmosphere $\tau = 1.3$ from Moroz [17]. Thermal emission of the surface is a product of the Plank function that strongly depends on surface temperature and therefore on altitude, and surface emissivity ε defined by mineralogical composition and surface material grain size.

These computations yield an image of the point spread function and values for t and r. Image of the point spread function is used to produce synthetic image of the surface, convolving the image of the surface brightness with the point spread function.

3.3.2. Calculating the surface emissivity maps

To obtain maps of the surface emissivity the VMC observations must be compared to the model images. Due to unknown cloud opacity and uncertainties in the VMC radiometric calibration we normalized the images by the value at a reference location(s), where the surface was assumed to be of basaltic composition.

The Monte Carlo radiative transfer simulations were used to determine the atmospheric blurring function, atmosphere transmittance and reflectance. The modelling gave the blurring function $F(x, y)$ with half-width of ≈ 50 km, which is in agreement with both apparent blurring of VMC images and previous results obtained by Hashimoto and Imamura [8].

The difference between our blurring functions and the one from Hashimoto and Imamura [8] could be caused by using the different phase function of atmospheric particles and different cloud models. Values of atmospheric reflectance r and transmittance t for selected atmosphere model (obtained from same simulations) are $r = 0.77$ and $t = 0.21$, for zero surface altitude. Also these calculations were used to check if outgoing flux on the top of the atmosphere is orthotropic, because eq. (3.2) is valid only in that case.

To calculate synthetic VMC images we used the Magellan topography derived from Magellan Radar Altimeter [6]. The topography data were converted into the maps of temperature and surface brightness distribution assuming thermal equilibrium with the atmosphere, constant lapse rate of $-8.1\,\mathrm{K\,km^{-1}}$ [29] and constant emissivity (exact emissivity value does not matter because of further normalization). Then synthetic VMC images were obtained by convolving the surface brightness distribution with the blurring function (eq. (3.2)).

In order to get rid of uncertainties in the VMC absolute calibration and cloud opacity, we normalized the measured images dividing them by the brightness at a reference location individually selected for each mosaic. From eq. (3.2) we can derive the following expression for the VMC normalized image V:

$$V(x,y) = \frac{t(x,y)\varepsilon(x,y)\left[1 - r(1-\varepsilon_0)\right]}{t(x_0,y_0)\varepsilon_0\left[1 - r(1-\varepsilon(x,y))\right]} \cdot \\ \cdot \frac{\iint B\left[T_s(x',y')\right] \cdot F(x-x', y-y')\,dx'dy'}{\iint B\left[T_s(x',y')\right] \cdot F(x_0-x', y_0-y')\,dx'dy'} \tag{3.3}$$

where ε_0 is the assumed surface emissivity at the reference location (x_0, y_0).

In addition, we considered a model case with constant surface emissivity. The expression for normalized model image is

derived in a similar way:

$$M(x,y) = \frac{t(x,y)}{t(x_0,y_0)} \cdot \\ \cdot \frac{\iint B\left[T_s(x',y')\right] \cdot F(x-x',y-y')\,dx'dy'}{\iint B\left[T_s(x',y')\right] \cdot F(x_0-x',y_0-y')\,dx'dy'} \tag{3.4}$$

All contrasts in the model image are due to temperature differences and not emissivity variations. From eqs. (3.3) and (3.4) we derive the following expression for the unknown surface emissivity distribution:

$$\varepsilon(x,y) = \frac{R(x,y)\varepsilon_0(1-r(x,y))}{1+r(x,y)\left[\varepsilon_0(1-R(x,y))-1\right]} \tag{3.5}$$

where

$$R(x,y) = \frac{V(x,y)}{M(x,y)}.$$

Thus eq. (3.5) allows us to derive spatial distribution of the surface emissivity from the ratio of the normalized VMC and model images and assumed emissivity ε_0 at a reference location. We make two remarks on eq. (3.5). First, it is applicable only to emissivity variations of spatial scale greater than the full width of the blurring function ($\approx$ 100 km, or $\approx$ 10 VMCpixels), which holds for large-scale surface features. Second, the distance between the reference site and the place where we determine emissivity should not exceed typical scale of deep cloud inhomogeneities ($\sim$ 1000 km). Both conditions are met in the areas analysed in this work.

3.4. Segmented emissivity map

3.4.1. Retrieving the surface emissivity from the camera images

To retrieve surface emissivity from the camera images we modeled radiative transfer in the atmosphere, using a hybrid approach, that combines Monte-Carlo-based simulations to retrieve optical properties of the atmosphere, and a two-streams approximation to model out of the atmosphere flux distribution. Initial assumptions were the adiabatic lapse rate (-8.1 K km^{-1}) in the lower atmosphere, basing on the Magellan GTDR, clouds and hazes structure following the Venus International Reference Atmosphere (VIRA) model. To calibrate gaseous absorption for the VMC IR2 channel, we considered regional plains at different altitudes. Assuming their age and composition are the same on average, we fit the absorption to remove altitudinal trend for retrieved emissivity values. Retrieved empirical solution turned out to work well for altitudes beyond the range used to calibrate the absorption (-1 to 1 km). Radiometric calibration of the VMC is uncertain, and therefore we retrieve only relative emissivity. In this study, the assumed mean emissivity for regional plains to be 0.5. All the other emissivity retrievals are related to that value. Details could be found in section 3.3.

The assumptions, explained above (lapse rate, optical thickness of the clouds) were used by us previously to analyse selected VMC orbits and locations [2, 4]. However we want to note that when we applied the same parameters to the whole VMC dataset, we found that synthetic images do not match observations, and that was studied.

3.4.2. Algorithm and retrieved results

The continuous emissivity map for the whole range of longitudes turned out to be hardly possible to be derived from the VMC data due to the poor knowledge of the VMC radiometric calibration and the inability to reconstruct the state of the atmosphere from observation in a single spectral channel. Thus it was decided to produce a few map segments, that together cover all the longitudes.

These would be fairly self-consistent, although it was noted that between such orbit groups, there would still be variabilities that are not linked to emissivity variability but would be due to cloud variability and/or instrument degradation. It was still assessed that this could be a useful dataset and could allow for the final milestones to be partially achieved.

We settled at 9-segment map, all segments are of the same longitudinal range ($40°$). We found no strong reason to put segment border at certain location, and therefore the first one begins at $0°$. There is no overlap between the segments. While VMC surface observations extends from (almost) the north pole down to $60°$ south (and sometimes even lower than

that), there are no much data to the south from $50°$S and observations at high north latitudes are made at such low altitude and high spacecraft speed that blurring, caused by that, greatly complicates analysis. Thus, the segments cover the latitude range from $50°$S to $60°$N.

The map segments were computed in the following way:

1. For each VMC orbit with surface observations we make a mosaic, consisting of all images from that orbit.
2. For each segment we create a list of VMC orbits that intersect with the segment.
3. Orbital-wise mosaic from each intersecting orbit is projected into the segment geometry, thus bringing all the segment orbits into the same geometry.
4. A map of reference area (section 3.1.1) is projected into the segment geometry as well, and a mask image is created.
5. Mosaics, whose intersection with the reference area is smaller than 0.1 of the total mosaic area, are rejected.
6. For each VMC orbital mosaic we find a factor that withing the non-masked parts of the VMC mosaics (*i.e.* images of the reference region) make the average brightness identical. The found set of factors are applied then to the whole orbital mosaics. This action follows from two assumptions we have to make: average emissivity in the reference region is constant for any reasonably large subset of the reference region, and that we neglect cloud inhomogeneity.
7. All the orbital mosaics are averaged.
8. An emissivity map is computed from the average VMC mosaic, as described in section 3.3.
9. To estimate emissivity retrieval error, the emissivity map is computed from each individual orbital mosaic.

The data set is a set of nine emissivity maps and the additional information as standard deviations and brightness distribution. Example of the produced emissivity map for segment 5 (longitudes $200°$ to $240°$E) and some additional information are presented in fig. 3.7 and fig. 3.8.

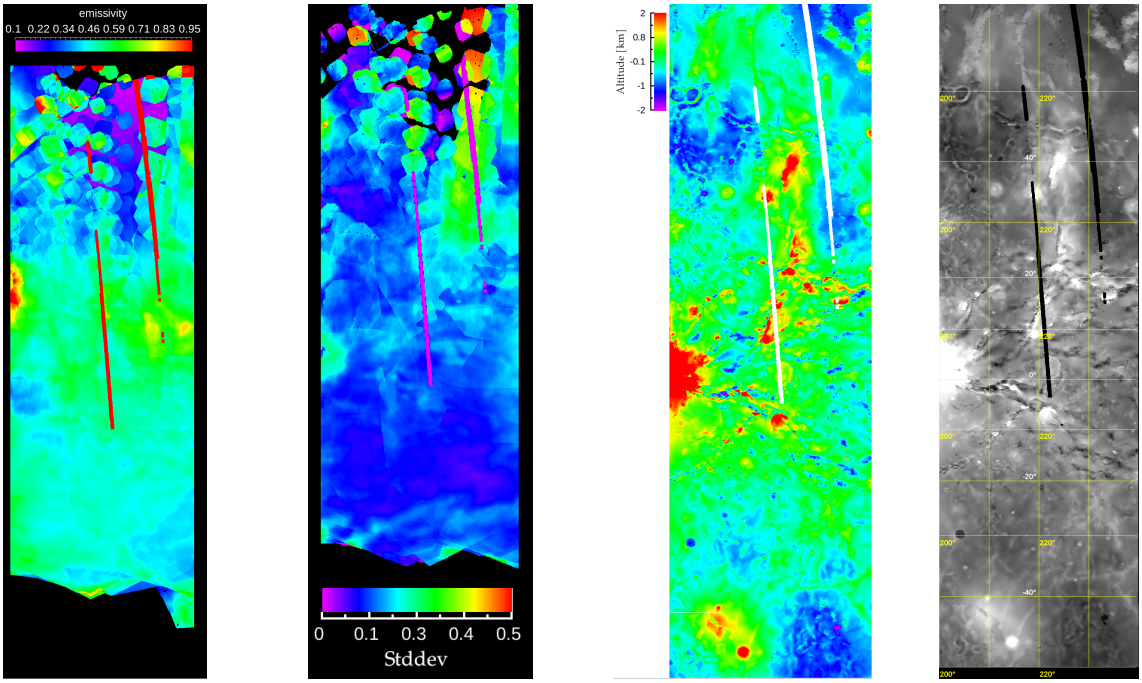

(a) Emissivity (b) Std dev norm (c) Magellan altimetry (d) Magellan altimetry

Figure 3.7.: Segment 5: Longitude 200-240 degrees. a relative emissivity map; b standard deviation; c Magellan altimetry (colour); d same as c but in gray scale

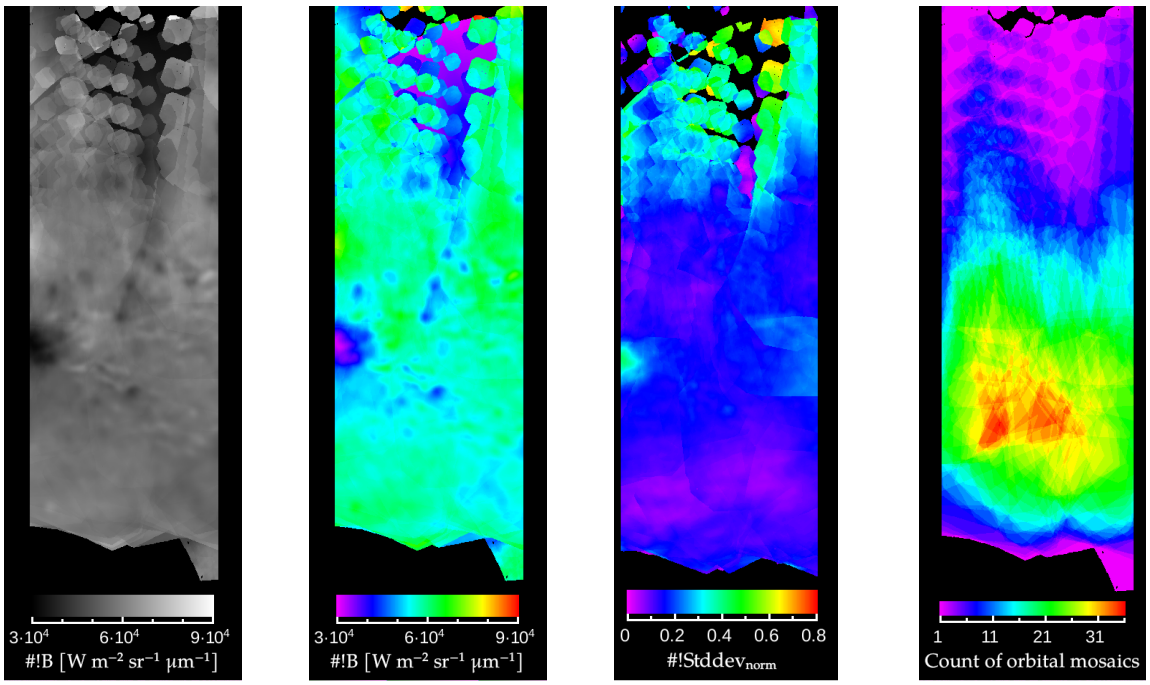

(a) B corrected (b) B corrected (c) B Stddev norm (d) B Count of orbits

Figure 3.8.: Segment 5: Longitude 200-240 degrees. Brightness distribution a in gray and b in colour scale, and statistical information: c standard deviation; d count of orbital mosaic

3.5. Data format and naming

The dataset ID is “VMC-NIR2-EMI_SGMNT-SCP”, where SCP = Surface and Cloud Properties (the name of the ESA granted project). The data set is a set of nine emissivity maps and the visualized additional information and are stored in GSF. Due to the complexities of the data and the capabilities of the used algorithm, the emissivity map consists of nine equal segments with the step by longitude $40°$. The format of the retrieved data archive is described in [30].

The data set consists of images in the PDS3 format (image files are uncompressed pixel arrays with attached labels in the PDS3 format) in files with the ”.img” extension, in-line with the format and naming of the historical Venus Express VMC data archive in the ESA Planetary Science Archive (PSA). The files can be read by any PDS3 compatible viewer (e.g. NASAView). Description of the metadata could be found in the standard documentation, *e.g.* the PDS objects and attributes used are fully compliant with the definitions given in the PDS3 reference (Appendices A and B in [20]) and the Planetary Science Data Dictionary [23]. Some details can also be found in this document in chapter B and chapter C.

4. Acknowledgements

These data were derived under the ESA Science Faculty programme (Surface and cloud properties from VMC/Venus Express observations, ESA contract number: 4000126833/18/NL/IB/gg).

The authors are grateful to ESA for the implementation of the Venus Express mission, to the teams at ESOC and ESAC for their professionalism in science planning and operations, and to the VMC Principal Investigators Dr. Wojciech J. Markiewicz and Dr. Dmitry V. Titov. The authors are grateful to the German Aerospace Center (DLR) for providing the VMC data processing and to the ESA Planetary Science Archive (PSA) for providing the VMC data (VMC data archive). The Venus Magellan SAR and GxDR data used in this work are available from the PDS geosciences node. The authors thank Dr. Mikhail A. Ivanov for providing the global geological map of Venus.

We thank Dr. Dmitry V. Titov for obtaining and supervising the ESA contract under which this work was conducted, for the ideas that formed the basis of the work, and for many productive discussions over many years of joint work within the VMC team. We thank Professor Dr. Alexander Bazilevsky for many years of fruitful collaboration within the VMC team and advice on the geology of Venus.

The authors would also like to thank the Max Planck Institute for Solar System Research (MPS), Germany, for long-term support of the VMC team and in particular this work; personally Dr. Andreas Nathues and the directors of the Planetary Department Professor Dr. Ulrich Christensen and Professor Dr. Thorsten Kleine.

A. Overview of instrument design, data handling process and product generation (from VMC-EAICD)

This information has been copied from [24] and placed here for the convenience of users of the data archive.

A.1. Instrument Design Overview

The VMC camera consists of one unit that houses the optics, CCD and readout electronics (CRE), digital processing unit (DPU), and power converter (POC). Figure A.1 shows the sketch of the VMC camera. The experiment consists of one unit with optics and focal plane mounted to the upper cover and a stack of electronic boards occupying the rest of the box. The size of PCBs is 80x80 mm. The walls of the camera are 3 mm thick to provide sufficient stiffness and radiation protection. Additional radiation shielding will be provided in the vicinity of the CCD.

The current baseline is to mount the camera on the +Y wall inside the spacecraft. Red dots on the +Y wall in the VMC sketch mark the mounting points of the camera. A Peltier cooler is attached to the CCD bottom. A thermal strap will take heat from the CCD to the spacecraft wall. The red star shows the thermal reference point (TRP), specified for the CCD and the electronics. In order to avoid moving parts (filter wheel) the camera is designed so that four objectives (channels) share a single CCD. The stray light protection is provided by external and internal baffles. The latter are also used to prevent optical cross-talk between the channels. Further information about the insturment and its operation can be found in [5].

A.2. Data handling process

All VMC data are processed at IDA, Braunschweig and DLR in Berlin, Germany. The data processing consists of the following steps:

- transfer of data from ESOC to IDA
- remove all transmission headers to get the original camera data
- decompress the data
- transfer data to DLR
- convert data into VICAR file format
- split data from different sensors to generate Level-1 files
- radiometric calibration of the data
- calculate footprints of every image file and get Level-2 files

The formats of the data levels 1 and 2 are described in [25] and [26], respectively.

All data processing steps at Deutsches Zentrum für Luft- und Raumfahrt (German Aerospace Center) (DLR) are performed in the Video Image Communication and Retrieval (VICAR) environment [19], a software package developed and maintained by NASA Jet Propulsion Laboratory (JPL) and used for the data processing of many planetary missions.

DLR developed specific VICAR modules for every processing step. The cognizitant persons for the specific task are listed in chapter 1.8.

Please, adress all questions and comments through the Data Processing Manager (thomas.roatsch@dlr.de).

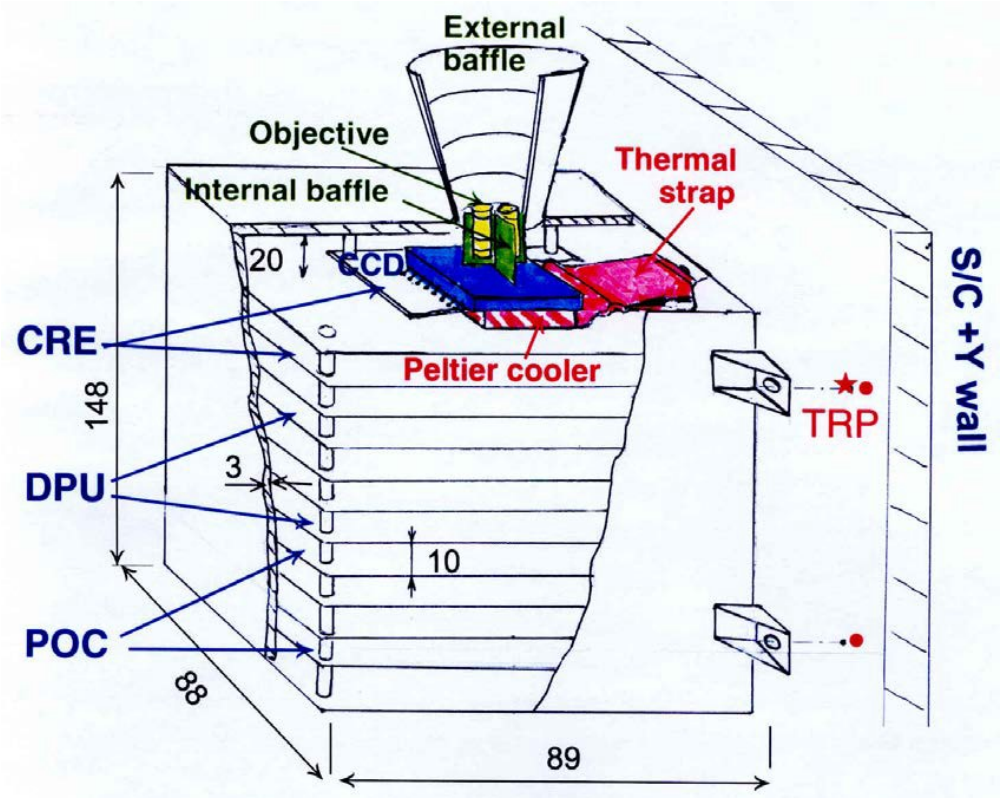

Figure A.1.: VMC sketch

A.3. Product generation

The VMC data are processed at Institute of Computer and Communication Network Engineering, Braunschweig, Germany (IDA) and DLR when they become available at European Space Operation Center (ESOC). Both level-1 and level-2 data are sent to the Principal Investigator (PI) and distributed to the Co-Investigator (CoI) team. The data will be checked by the team and improved versions of the data will be calculated if necessary. Another reason for new image version are improved SPICE kernels.

The final step of the product generation is the conversion from the VICAR format to Planetary Data System (PDS) format and the generation of the complete data sets. This step is also performed at DLR in Berlin about a month before the final delivery to PSA.

The final products will be sent to the PI and the CoIs who are in charge for the data validation. The data will be send from DLR to PSA after succesful validation and PI approval.

B. Archive format and content (from VMC-EAICD)

This information has been copied from [24] and placed here for the convenience of users of the data archive.

B.1. Format and conventions

B.1.1. Deliveries and archive volume format

The VMC data will be delivered to PSA every 6 months. Every delivery contains the data taken during a time period of 6 months. The delivery will be performed only via file transfer, no storage media like CD or DVD will be used. The Planetary Science Archive of European Space Agency (ESA) implemented the "Release" concept [14]: data is delivered as units (releases), which can be updated (revision). Two specific data elements are included to handle the release concept:

`RELEASE_ID`
`REVISION_ID`

RELEASE_ID defines the release number and REVISION_ID defines the revision number.

The data will be split in a couple of different releases to avoid file transfer problems with very huge files. The releases will also be compressed (using bzip2) to minimize the file transfer time.

Every release will be packed to one single file (only for the file transfer from DLR to PSA) using the UNIX tar command with the following options: tar cfv. The following file naming scheme (including release and revision number) will be used for the file transfer ot the releases: VMC_rel001rev000.tar.bz2

The VMC team delivers only radiometrically calibrated data since raw data are useless for the general public due to a couple of camera problems.

The uncalibrated (raw) data will be delivered to European Space Research and Technology Center (ESTEC) in VICAR format six months after the end of the nominal mission together with the radiometric calibration software. No special documentation will be written for these data and the software.

B.1.2. Data set ID formation

The data from the nominal mission belong to this dataset: `VEX-V-VMC-3-RDR-V3.0`

The data from the first mission extension (starting with orbit 550) belong to this dataset: `VEX-V-VMC-3-RDR-EXT1-V3.0`

The data from the second mission extension (starting with orbit 550) belong to this dataset: `VEX-V-VMC-3-RDR-EXT2-V3.0`

The data from the third mission extension (starting with orbit 550) belong to this dataset: `VEX-V-VMC-3-RDR-EXT3-V3.0`

The data from the fourth mission extension (starting with orbit 550) belong to this dataset: `VEX-V-VMC-3-RDR-EXT4-V2.0`

This name follows the standard PDS rules and contains the mission name, the instrument name, describes the level of processing (REDR) and the version number. It is currently not planned to deliver different versions. The `DATA_SET_ID` must be changed whenever it will become necessary to deliver different versions.

B.1.3. Data Directory Naming Convention

The VMC data are sorted by orbit in the DATA directory, each sub-directory will have the name oooo where oooo is the number of the orbit in which the data were taken.

B.1.4. Filename convention

The file naming convention is described in detail in [27]. The image files in the DATA directories follow this convention: `VOOOO_MMM_DD2.IMG`
where

OOOO 4 digit orbit number

MMM number of the image in this orbit

DD sensor name (can be N1, N2, VI, UV)

The '2 indicates the level of processing which is archived in PSA/PDS.

Please, note that all sensor data which were taken together will get the same image number.

B.2. Standards used in data product generation

B.2.1. PDS standard

All data apply to version 3.6 of the PDS Standards Reference, please see [21, 20] for details.

B.2.2. Time standards

All time information in the data follows the SPICE time standards. Please, see [10] for details. Within the data products themselves, the time standard used is ET (Ephemeris Time), which is a double precision number of seconds. The starting point for this time is the J2000 epoch. This epoch is Greenwich noon on January 1, 2000 Barycentric Dynamical Time. This ephemeris time is calculated from the Spacecraft Onboard Time using the appropriate SPICE routines and the time correlation packages which are provided by ESTEC as a SPICE Clock Kernel. Outside of the products themselves, there are a few instances in the VMC data sets where time flags are provided. The main time values are provided in the data product labels, which provide a start and stop time for the measurement, and a corresponding clock count from the spacecraft. Below, the standards used to define these values are described.

B.2.2.1. START_TIME and STOP_TIME

B.2.2.1.1. Formation The PDS formation rule for dates and time in UTC is: YYYY-MM-DDThh:mm:ss.fff

YYYY year (0000-9999)

MM month (01-12)

DD day of month (01-31)

T date/time separator

hh hour (00-23)

mm minute (00-59)

ss second (00-59)

fff fractions of second (000-999) (restricted to 3 digits)

This standard is followed for all START_TIME and STOP_TIME values in the products included in the VMC data sets.

B.2.2.2. SPACECRAFT_CLOCK_START_COUNT and SPACECRAFT_CLOCK_STOP_COUNT

The SPACECRAFT_CLOCK_START_COUNT and SPACECRAFT_CLOCK_STOP_COUNT values represent the on-board time counters (OBT) of the spacecraft and instrument computers. This OBT counter is given in the headers of the experiment telemetry source packets. It contains the data acquisition start time as 32- bit of unit seconds followed by 16-bit of fractional seconds. The time resolution of the fractional part is $2^{-16} = 1.52 \times 10^{-5}$ s. Thus, the OBT is represented as a decimal real number in floating-point notation with 5 digits after the decimal point.

A reset of the spacecraft clock is represented by an integer number followed by a slash, e.g. “1/” or “2/”.

Example:

```
SPACECRAFT_CLOCK_START_COUNT = "1/21983325.39258"
```

B.2.2.3. Reference Systems

The reference systems used for orbit, attitude, and target body follow the SPICE standards and are defined in the different SPICE kernels. Please, see [41, 10] for details.

All latitudes and longitudes are given in degrees, latitudes are planetocentric.

B.2.2.4. Other Applicable Standards

No other standards are used.

B.3. Data validation

The validation of these volumes is divided into two processes:

The first process is to check that the volumes are technically correct:

- Insure that the volume is complete, and has correct structure as defined in this document.
- Insure that dynamically generated file, such as index and catalog files are correct and complete.
- Insure that structure of each generated volume is PDS compliant

These steps will be performed using PSA Volume Verifier (PVV), the PVV developed by ESTEC [40].

The second process is to check that the image data contained in the data volumes are correct. This will be done by visual inspection by the PI and the CoIs (tbd). Specific tools for automated checks may be developed by the teams in charge for this step.

B.4. Content

B.4.1. Volume Set

There are no volume sets since the data will be delivered electronically. It is not planned to generate archives on any medium (like CD-ROM or DVD).

B.4.2. Data Sets

There are five datasets, one contains the data from the nominal mission, the second one (starting at orbit 550) contains the data from the first mission extension, the third one contains the data from the second mission extension, the fourth one contains the data from the third mission extension, and te fivth one contains the data from the fourth mission extension. Six one contains the data for nightside only re-calibrated via the procedure described in XX.

B.4.3. Directories

B.4.3.1. Root directory

The Root Directory contains the following standard PDS files:

```
AAREADME.TXT
ERRATA.TXT
VOLDESC.CAT
```

B.4.3.2. Calibration directory

There is no calibration directory for the data set VEX-V-VMC-3-RDR-V1.0, the data are already radiometrically calibrated. Information about the calibration can be found in `VMC_CALIBRATION_REPORT.PDF` and `VMC_INLIGHT_CALIBRATION_REPORT.TXT` in the DOCUMENT directory.

Information about the geometric calibration can be found in the SPICE instrument kernel which is distributed seperately by PSA.

B.4.3.3. Catalog Directory

The Catalog Directory contains the following standard PDS files:

```
CATINFO.TXT
DATASET.CAT
INST.CAT
INSTHOST.CAT
MISSION.CAT
PERSON.CAT
REF.CAT
```

This directory also contains the file `RELEASE.CAT` as described in [14]. This file is necessary to use the release concept developed by PSA.

B.4.3.4. Index Directory

B.4.3.4.1. Dataset Index File, index.lbl and index.tab The Index Directory contains the required PDS index files which are generated by PVV [40].

B.4.3.4.2. Geometric Index File, geoindex.lbl and geoindex.tab The Index Directory also contains the Geometric Index File as defined in [22].

The geometry index files contains the information for 100 points in the VMC image when at least a part of Venus is visible in the image. These 100 points are the same as in the label entries `FOOTPRINT_POINT_LATITUDE` and `FOOTPRINT_POINT_LONGITUDE` which describe the footprint of the image.

B.4.3.4.3. Other Index Files The data set also contains browse index files which are generated using PVV [40]. Browse images are still tbd, please see section B.4.3.5.

B.4.3.5. Browse Directory and Browse Files

It is still tbd if browse image are necessary. The original images data are already very small (512×512). This will be decided when a sufficient set of Venus data will be available.

B.4.3.6. Geometry Directory

This directory has the same structure as the DATA directory, the files are sorted by orbit number. The geometry files have the same filename as the image files, only the extension is changed to GEO. Each geometry file has five bands: INCIDENCE ANGLE, EMISSION ANGLE, PHASE ANGLE, LATITUDE, and LONGITUDE The unit for all five bands is DEGREE.

All external geometry information (orbit data, attitude data, etc.) can be found in the Venus Express SPICE data set. The SPICE data are released as seperate data sets and are necessary for the generation of higher data levels, SPICE kernels will not be available as separate release at the time of the first VMC data release, unfortunately.

The user of the VMC data has to get the SPICE kernels from the ftp server at ESTEC or from the ftp mirror at NAIF.

B.4.3.7. Software Directory

No software will be delivered.

Software to read the images and the geometry files is available at different locations, e.g.:

- IDL PDS Reader Library.
- PDS Image Readers a and b
- GIMP and Plug-in to load PDS images into GIMP.

B.4.3.8. Gazetter Directory

There is no Gazetter Directory.

B.4.3.9. Label Directory

There is no Label directory.

B.4.3.10. Document Directory

This directory contains the documentation for the VMC data sets. The content is:

DOCINFO.TXT the standard PDS info file.

VMC_EAICD.LBL the label for the Experimenter to Archive ICD

VMC_EAICD.PDF the Adobe PDF file of the Experimenter to Archive ICD

VMC_EAICD.TXT the Text file of the Experimenter to Archive ICD

VMC_ESA_SP.LBL the label for the VMC Instrument Description published in the ESA SP-13

VMC_ESA_SP.PDF the Adobe PDF file of the ESA SP-1325

VMC_LABEL.LBL the label for VMC_LABEL.PDF

VMC_LABEL.PDF a table summarizing the PDS label

VMC_NATURE.LBL the label for VMC_NATURE.PDF

VMC_NATURE.PDF an article from Nature summarizing the first scientific results from VMC

VICAR2.LBL the Label for the description of the VICAR labels

VICAR2.TXT Text file describing the VICAR label.

B.4.3.11. Extras Directory

There is no Extras Directory.

B.4.3.12. Data Directory

The Data Directory contains sub-directories for every orbit which is part of the data set, the directory names are the four digits orbit number. The contents of these sub-directories is described in section B.4.8.

B.4.4. Other Data Products

No Pre-Flight Data Products, Sub-System test data, and instrument calibration data will be delivered to PSA/PDS.

B.4.5. In-Flight Data Products

The VMC data archive contains all data which were taken in Venus orbit.

B.4.6. Software

The VMC processing software was developed in the VICAR environment [36]. VICAR was developed by NASA/JPL and was used for the processing of camera data from many planetary missions (e.g. Viking, Galeileo). The data processing team at DLR in Berlin developed specific modules to process the VMC data. These modules perform the following steps:

- remove all telemetry headers from the data
- sort the data by sensor and combine the image data with the housekeeping data
- decompression of the data
- radiometric calibration of the data
- apply additonal orbit dependent calibration files to reduce the data artefacts
- calculation of the footprints for every image

B.4.7. Documentation

The contents of the documentation directory is described in section B.4.3.10.

B.4.8. Derived and other Data Products

There are currently no plans to deliver derived and other data products. Also, no data based on the cooperation with other Venus Express teams will be delivered.

C. Detailed interface specifications (from VMC-EAICD)

This information has been copied from [24] and placed here for the convenience of users of the data archive.

C.1. Data Product Structure

The data structure consists of an ASCII PDS label, followed by an embedded ASCII VICAR label, followed by a block of binary image data. Inherent to the VICAR label is the possibility of an ASCII EOL label being appended after the binary data in order to handle label modifications. This EOL label is simply a continuation field for the main VICAR label, when there is no more space for expansion before the image data.

C.2. Label and header descriptions

C.2.1. PDS label

VMC data have an attached PDS label. A PDS label is object-oriented and describes the objects in the data file. The PDS label contains keywords for product identification. The label also contains descriptive information needed to interpret or process the data in the file.

PDS labels are written in Object Description Language (ODL [21]. PDS label statements have the form of ”keyword = value”. Each label statement is terminated with a carriage return character (ASCII 13) and a line feed character (ASCII 10) sequence to allow the label to be read by many operating systems. Pointer statements with the following format are used to indicate the location of data objects in the file:

```
^object = location
```

where the carat character (^, also called a pointer) is followed by the name of the specific data object. The location is the 1-based starting record number for the data object within the file.

C.2.2. PDS image object

An `IMAGE` object is a two-dimensional array of values, all of the same type, each of which is referred to as a sample. `IMAGE` objects are normally processed with special display tools to produce a visual representation of the samples by assigning brightness levels or display colors to the values. An `IMAGE` consists of a series of lines, each containing the same number of samples.

The required `IMAGE` keywords define the parameters for simple `IMAGE` objects:

LINES is the number of lines in the image.

LINES LINE_SAMPLES is the number of samples in each line.

LINES SAMPLE_BITS is the number of bits in each individual sample.

LINES SAMPLE_TYPE defines the sample data type.

The `IMAGE` object has a number of keywords relating to image statistics. These keywords will be present in all data, the statistics keywords are:

- MEAN
- MEDIAN

- MAXIMUM
- MINIMUM
- STANDARD_DEVIATION

Many variations on the basic `IMAGE` object are possible with the addition of optional keywords and/or objects. The `^IMAGE` keyword identifies the start of the image data and will skip over the VICAR label.

C.2.3. Keyword length limits

All PDS keywords are limited to 30 characters in length (Section 12.7.3 in PDS Standards Reference). Therefore, software that reads VMC PDS labels must be able to ingest keywords up to 30 characters in length.

C.2.4. Data type restrictions

In order to accomodate VICAR dual-labeled files, 16-bit data must be stored as signed data. Unsigned 16-bit data is not supported.

C.2.5. Interpretation of N/A, UNK, and NULL

During the completion of data product labels or catalog files, one or more values may not be available for some set of required data elements. In this case PDS provides the symbolic literals “N/A”, “UNK”, and “NULL”, each of which is appropriate under different circumstances.

- “N/A” (“Not Applicable”) indicates that the values within the domain of this data element are not applicable in this instance.
- “UNK” (“Unknown”) indicates that the value for the data element is not known and never will be.
- “NULL” is used to flag values that are temporarily unknown. It indicates that the data preparer recognizes that a specific value should be applied, but that the true value was not readily available. “NULL” is a placeholder

The following values are used for N/A and UNK in the image labels (as described in chapter 17 of the PDS standards reference [20]):

	Signed Integer (4 byte)	Real
N/A	-2147483648	-1.E32
UNK	2147483647	1.E332

C.2.6. VICAR label

For all data products, an embedded VICAR label follows the PDS label and is pointed to by the PDS pointer `^IMAGE_HEADER`. The VICAR label is also organized in an ASCII, `keyword = value` format, although there are only spaces between keywords (no carriage return/line feeds as in PDS). The information in the VICAR label is an exact copy of the information in the PDS label as defined in the next section. The VICAR label is not intended for the data user, it is only used DLR internal during the processing pipeline.

C.2.7. VICAR format

The reader is referred to the VICAR File Format document for details of the format. The following text is an excerpt which describes the basic structure:

> A VICAR file consists of two major parts: the labels, which describe what the file is, and the image area, which contains the actual image. The labels are potentially split into two parts, one at the beginning of the file, and one at the end. Normally, only the labels at the front of the file will be present. However, of the EOL keyword in the system label (described below) is equal to 1, then the EOL labels (End Of file Labels) are present. This

happens if the labels expand beyond the space allocated for them. The VICAR file is treated as a series of fixed-length records, of size RECSIZE (see below). The image area always starts at a record boundary, so there may be unused space at the end of the label, before the actual image data starts. The label consists of a sequence of ”keyword=value” pairs that describe the image, and is made up entirely of ASCII characters. Each keyword-value pair is separated by spaces. Keywords are strings, up to 32 characters in length, and consist of uppercase characters, underscores (“_”), and numbers (but should start with a letter). Values may be integer, real, or strings, and may be multiple (e.g. an array of 5 integers, but types cannot be mixed in a single value). Spaces may appear on either side of the equals character (=), but are not normally present. The first keyword is always LBLSIZE, which specifies the size of the label area in bytes. LBLSIZE is always a multiple of RECSIZE, even if the labels don’t fill up the record. If the labels end before LBLSIZE is reached (the normal case), then a 0 byte terminates the label string. If the labels are exactly LBLSIZE bytes long, a null terminator is not necessarily present. The size of the label string is determined by the occurrence of the first 0 byte, or LBLSIZE bytes, whichever is smaller. If the system keyword EOL has the value 1, then End- Of-file Labels exist at the end of the image area (see above). The EOL labels, if present, start with another LBLSIZE keyword, which is treated exactly the same as the main LBLSIZE keyword. The length of the EOL labels is the smaller of the length to the first 0 byte or the EOL’s LBLSIZE. Note that the main LBLSIZE does not include the size of the EOL labels. In order to read in the full label string, simply read in the EOL labels, strip off the LBLSIZE keyword, and append the rest to the end of the main label string.

C.3. Binary Data Storage Conventions

VMC data are stored as binary data. The data are stored in signed 16-bit integers. The PDS and VICAR labels are stored as ASCII text. The ordering of bits and bytes is only significant for pixel data; all other labeling information is in ASCII. All data are stored as Most Significant Byte first (”big-endian”, as used by e.g. Sun computers and Java)

C.4. PDS keyword table

The same keywords are used for all data. These keywords are described in the following table. Please, note that more keywords could become necessary if advanced onboard processing will be used. The decision about advanced onboard processing is delayed until arrival at Venus. Aditional geometry keywords, e.g. SPACECRAFT_ALTITUDE, can be calculated by the user using the SPICE kernels from the PSA web page ftp://ssols01.esac.esa.int/pub//data/SPICE/VEX/kernels/. The SPICE tutorials from the NAIF web page ftp://naif.jpl.nasa.gov/pub/naif/toolkit_docs/Tutorials/ contain detailed examples in different programming languages how to calculate these values.

FILE_NAME	usual default name of the output file; this entry allows the user to check for accidental renaming of files, filename without path	string	
DATA_SET_ID	The data_set_id element is a unique alphanumeric identifier for a data set or a data product.	string	VEX-V-VMC-2-EDR-V1.0 VEX-V-VMC-3-RDR-V1.0
DATA_SET_NAME	The data_set_name element provides the full name given to a data set or a data product.	string	
PRODUCER_ID	The producer_id element provides a short name or acronym for the producer or producing team/group of a dataset.	string	
PRODUCER_FULL_NAME	The producer_full_name element provides the full_name of the individual mainly responsible for the production of a data set.	string	
PRODUCER_INSTITUTION_NAME	The producer_institution_name element identifies a university, research center, NASA center or other institution associated with the production of a data set.	string	
DETECTOR_ID	identifies which of the ten CCD detectors was used for this particular image.	string	VEX_VMC_NIR-1, VEX_VMC_NIR-2, VEX_VMC_VIS, VEX_VMC_UV
INSTRUMENT_HOST_ID	The instrument_host_id element provides a unique identifier for the host where an instrument is located.	string	VEX
INSTRUMENT_HOST_NAME	full name of the spacecraft	string	VENUS_EXPRESS
INSTRUMENT_ID	The instrument_id element provides an abbreviated name or acronym which identifies an instrument.	string	VMC
INSTRUMENT_NAME	full name of an instrument	string	VENUS MONITORING CAMERA
INSTRUMENT_TYPE	The instrument_type element identifies the type of an instrument.	string	FRAMING CAMERA
MISSION_NAME	full name of mission	string	VENUS_EXPRESS
MISSION_ID	The mission_id element provides a synonym or mnemonic for the mission_name element.	string	VEX

MISSION_PHASE_NAME	The mission_phase_name element provides the commonly-used identifier of a mission phase.	string	
PROCESSING_LEVEL_ID	identifies the processing level of a data set; parameter must be updated after each processing step according to the program specification, DLR-Levels	int	1 or 2
PRODUCT_CREATION_TIME	The product_creation_time element defines the UTC system format time when a product was created.	string	
PRODUCT_ID	The product_id data element represents a permanent, unique identifier assigned to a data product by its producer.	string	
PRODUCT_TYPE	The PRODUCT_TYPE data element identifies the type or category of a product within a data set.	string	
RELEASE_ID	Number of the data release	int	
REVISION_ID	Number of the revision in a release	int	
VEX:SCIENCE_CASE_ID	Tbd	int	1, 2, ..., 9, 10
OBSERVATION_TYPE	Type of the observation this image belongs to.	string	tbd
SPACECRAFT_CLOCK_START_COUNT	Provides the value of the spacecraft clock at the beginning of a time period of interest.	string	
SPACECRAFT_CLOCK_STOP_COUNT	Provides the value of the spacecraft clock at the end of a time period of interest.	string	
IMAGE_TIME	Date and time of the middle of the image acquisition in UTC format ”YYYY- MM-DDTHH:MM:SS.MMMZ”		
START_TIME	Date and time of the start of the image acquisition in UTC format ”YYYY- MM-DDTHH:MM:SS.MMMZ”	string	
STOP_TIME	Date and time of the end of the image acquisition in UTC format ”YYYY- MM-DDTHH:MM:SS.MMMZ”	string	

ASCENDING_NODE_LONGITUDE	value of the angle of the xy-plane of the J2000 coordinate system to the ascending node computed from the spacecraft's position- and velocity vector at periapsis (not to be used during test and cruise)	°	real
MAXIMUM_RESOLUTION	highest resolution in an image	$\mathrm{m\,pix^{-1}}$	real
FOOTPRINT_POINT_LATITUDE	The footprint_point_latitude element provides the latitude of a point within an array of points along the border of a footprint, described as a polygon, outlining an imaged area on the planet's surface. Latitude values are planetocentric.	°	real (100)
FOOTPRINT_POINT_LONGITUDE	The footprint_point_longitude element provides the longitude of a point within an array of points along the border of a footprint, described as a polygon, outlining an imaged area on the planet's surface. Longitude values are planetocentric.	°	real (100)
ORBIT_NUMBER	number of the orbital revolution of the s/c around the target body (not to be used during test and cruise)		int
ORBITAL_ECCENTRICITY	value of orbit eccentricity computed from the spacecraft's position- and velocity vector at periapsis (not to be used during test and cruise)		real
ORBITAL_INCLINATION	value of the angle of inclination with respect to the xy-plane computed from the spacecraft's position- and velocity vector at periapsis		real
ORBITAL_SEMIMAJOR_ AXIS	value of orbit semi-major axis computed from spacecraft's position- and velocity vector at periapsis (not to be used during test and cruise)	km	real

PERIAPSIS_ALTITUDE	The PERIAPSIS_ALTITUDE element provides the distance between the spacecraft and the target body at periapsis. Periapsis is the closest approach point of the spacecraft to the target body in its orbit around the target body.	km	real	
PERIAPSIS_ARGUMENT_ANGLE	angle in the xy-plane of the J2000 coordinate system from the ascending node to periapsis (not to be used during test and cruise)	°	real	
PERIAPSIS_TIME	The PERIAPSIS_TIME element is the time, in UTC format ”YYYY-MM-DDThh:mm:ss[.fff]Z”, when the spacecraft passes through periapsis. Periapsis is the closest approach point of the spacecraft to the target body in its orbit around the target body. (not to be	time	string	
SPACECRAFT_ ORIENTATION	The spacecraft orientation element provides the orientation of a spacecraft in orbit or cruise in respect to a given frame. E.g. a non-spinning spacecraft might be flown in +Y or -Y direction in respect to the spacecraft mechanical build frame. This element shall be used in combination with the keyword spacecraft_orientation_desc that describes the convention used to describe the spacecraft orientation. The spacecraft orientation shall be given as a 3-tuple, one value for the x,y and z axes		real	
SPACECRAFT_POINTING_MODE	The spacecraft pointing element provides information on the pointing mode of the spacecraft. The definition of the modes and the standard values are given in the s/c pointing mode description element, that shall always accompany the keyword		string	{”NADIR”, ”ALONGTRACK”, ”ACROSSTRACK”, “INERT”}

RIGHT_ASCENSION	The right_ascension element provides the right ascension value. Right_ascension is defined as the arc of the celestial equator between the vernal equinox and the point where the hour circle through the given body intersects the Earth's mean equator (reckoned eastward).	°	real	
DECLINATION	The declination element provides the value of an angle, corresponding to latitude, used to fix position on the celestial sphere. Declination is measured positive north and negative south of the celestial equator, and is defined relative to a specified reference period or epoch.	°	real	
SPACECRAFT_SOLAR_DISTANCE	the spacecraft's distance to the Sun measured from its position vector at periapsis (not to be used during test and cruise)	km	real	
TARGET_NAME	name of the target body		string	VENUS, SKY
TARGET_TYPE	The target_type element identifies the type of a named target.		string	PLANET, STAR, SUN, COMET
DETECTOR_TEMPERATURE	Detector temperature	°C	real	
INST_CMPRS_NAME	flag indicating whether spacecraft onboard compression has been bypassed, in which case, the received data were uncompressed		string	NONE, tbd
INST_CMPRS_QUALITY	The compression index. A higher value means more compression		int	
INST_CMPRS_RATIO	mean compression rate for the entire image data represented in the file, this number is =1 for data collected in the bypass mode.		real	

BANDWIDTH	The bandwidth element provides a measure of the spectral width of a filter or channel. For a root-mean-square detector this is the effective bandwidth of the filter i.e., the full width having a flat response over the bandwidth and zero response elsewhere. For VMC this value is for the whole sensor (CCD+Optics).	nm	real
CENTER_FILTER_WAVELENGTH	The center_filter_wavelength element provides the mid_point wavelength value between the minimum and maximum instrument filter wavelength values. For VMC this value is for the whole sensor (CCD+Optics).	nm	real
EXPOSURE_DURATION	Integration time of the instruments CCD.	ms	real
MACROPIXEL_SIZE	The MACROPIXEL_SIZE element provides the sampling array size (e.g., 2x2, 4x4, 8x8), in pixels, that is used to reduce the amount of data an image contains by summing the values of the pixels, along the lines of the image.		int
LINE_FIRST_PIXEL	The line_first_pixel element provides the line index for the first pixel that was physically recorded at the beginning of the image array.		int
SAMPLE_FIRST_PIXEL	The sample_first_pixel element provides the sample index for the first pixel that was physically recorded at the beginning of the image array.		int
RADIANCE_OFFSET	The radiance_offset element provides the constant value by which a stored radiance is added. Note: Expressed as an equation: true_radiance_value = radiance_offset + radiance_scaling_factor * stored_DN_value.	$W\,m^{-3}\,sr^{-1}$	real

RADIANCE_SCALING_FACTOR	The radiance_scaling_factor element provides the constant value by which a stored radiance is multiplied. Note: Expressed as an equation: true_radiance_value = radiance_offset + radiance_scaling_factor * stored_DN_value	$W\,m^{-3}\,sr^{-1}$	real

C.5. Example PDS product label

```
DS_VERSION_ID                    = PDS3

/* FILE DATA ELEMENTS */

RECORD_TYPE                      = FIXED_LENGTH
RECORD_BYTES                     = 1024
FILE_RECORDS                     = 527
LABEL_RECORDS                    = 9

/* POINTERS TO DATA OBJECTS */

^IMAGE_HEADER                    = 10
^IMAGE                           = 16

/* PRODUCER IDENTIFICATION */

PRODUCT_CREATION_TIME            = 2015-07-08T14:42:58.000Z
PRODUCER_FULL_NAME               = "THOMAS ROATSCH"
PRODUCER_ID                      = DLR
PRODUCER_INSTITUTION_NAME        = "DEUTSCHES ZENTRUM FUER LUFT- UND
                                    RAUMFAHRT"
/* DATA DESCRIPTION AND IDENTIFICATION */

DATA_SET_ID                      = "VEX-V-VMC-3-RDR-V3.0"
DATA_SET_NAME                    = "VENUS EXPRESS VENUS VMC 3 V3.0"
DETECTOR_ID                      = "VEX_VMC_NIR-1"
FILE_NAME                        = "V0027_0003_N12.IMG"
INSTRUMENT_HOST_ID               = VEX
INSTRUMENT_HOST_NAME             = "VENUS EXPRESS"
INSTRUMENT_ID                    = VMC
INSTRUMENT_NAME                  = "VENUS MONITORING CAMERA"
INSTRUMENT_TYPE                  = "FRAMING CAMERA"
^INSTRUMENT_DESC                 = "INSTRUMENT_DESC.TXT"
MISSION_ID                       = VEX
MISSION_NAME                     = "VENUS EXPRESS"
MISSION_PHASE_NAME               = PHASE_0
PROCESSING_LEVEL_ID              = 3
PRODUCT_ID                       = "V0027_0003_N12.IMG"
PRODUCT_TYPE                     = RDR
RELEASE_ID                       = 0002
REVISION_ID                      = 0000

/* TIME RELATED INFORMATION */

SPACECRAFT_CLOCK_START_COUNT     = "1/0038280589.61713"
SPACECRAFT_CLOCK_STOP_COUNT      = "1/0038280591.61705"
IMAGE_TIME                       = 2006-05-18T01:29:51.000Z
START_TIME                       = 2006-05-18T01:29:50.000Z
STOP_TIME                        = 2006-05-18T01:29:52.000Z

/* ORBITAL INFORMATION */
```

```
ASCENDING_NODE_LONGITUDE          = 107.31
ORBIT_NUMBER                      = 27
ORBITAL_ECCENTRICITY              = 0.84
ORBITAL_INCLINATION               = 89.94
ORBITAL_SEMIMAJOR_AXIS            = 39468.3
PERIAPSIS_ALTITUDE                = 272.88
PERIAPSIS_ARGUMENT_ANGLE          = 101.22
PERIAPSIS_TIME                    = 2006-05-18T01:35:34.000Z
MAXIMUM_RESOLUTION                = 978.213 <m/pixel>
FOOTPRINT_POINT_LATITUDE          = (48.635,49.9316,52.0902,53.2923,54.1916
                                    ,54.8531,55.4254,55.6957,55.9501,
                                    56.4185,56.8422,57.2734,57.6274,57.9561
                                    ,58.4437,58.7209,58.9823,59.2594,
                                    59.7151,60.0548,60.4408,60.985,60.9426,
                                    60.8617,60.774,60.6642,60.5973,59.1002,
                                    53.2725,52.8007,52.5397,52.2574,51.949,
                                    51.607,51.2202,50.7685,50.5073,50.2113,
                                    49.8641,49.4295,48.7826,49.0445,48.7958
                                    ,48.4251,49.0377,48.7556,48.2925,
                                    48.9478,48.593,49.0731,48.7494,48.1438,
                                    48.8365,48.3135,48.8738,48.3501,48.8671
                                    ,48.2904,48.8156,48.0654,48.7104,
                                    49.0325,48.5253,48.886,48.1239,48.6582,
                                    48.9448,48.2103,48.6491,49.1004,48.4869
                                    ,48.7538,49.0965,48.3815,48.6258,
                                    48.9244,49.1155,48.2154,48.6016,48.6634
                                    ,48.38,49.2237,49.0674,48.8118,48.6027,
                                    49.2742,48.962,48.7121,49.3026,48.8591,
                                    48.3349,49.1464,48.8335,49.3305,49.0523
                                    ,48.5507,49.1807,48.7396,49.2482,
                                    48.635)
FOOTPRINT_POINT_LONGITUDE         = (147.053,147.313,147.785,148.071,
                                    148.298,148.489,148.661,148.816,148.967
                                    ,149.257,149.534,149.797,150.052,
                                    150.298,150.65,150.878,151.101,151.312,
                                    151.731,152.027,152.416,152.965,153.691
                                    ,154.545,155.281,156.14,156.631,157.387
                                    ,159.113,159.196,159.24,159.285,159.331
                                    ,159.38,159.432,159.488,159.518,159.55,
                                    159.586,159.626,159.679,159.628,159.491
                                    ,159.359,159.162,159.024,158.892,
                                    158.698,158.559,158.376,158.234,158.097
                                    ,157.912,157.769,157.591,157.445,157.27
                                    ,157.121,156.949,156.796,156.627,
                                    156.459,156.302,156.136,155.97,155.809,
                                    155.645,155.473,155.314,154.989,154.811
                                    ,154.651,154.327,154.136,153.977,
                                    153.654,153.326,153.107,152.62,151.595,
                                    151.047,150.958,150.599,150.224,150.024
                                    ,149.93,149.545,149.337,149.24,148.83,
                                    148.574,148.52,148.297,148.197,147.978,
                                    147.718,147.646,147.394,147.305,
```

```
                                   147.053)
SPACECRAFT_ORIENTATION             = (0.50444,0.274316,0.818713)
^SPACECRAFT_ORIENTATION_DESC       = "VEX_ORIENTATION_DESC.TXT"
SPACECRAFT_POINTING_MODE           = INERT
^SPACECRAFT_POINTING_MODE_DESC     = "VEX_POINTING_MODE_DESC.TXT"

/* TARGET IDENTIFICATION */

/* TARGET IDENTIFICATION */

TARGET_TYPE                        = LIMB
TARGET_NAME                        = VENUS
RIGHT_ASCENSION                    = 101.29
DECLINATION                        = -17.88
SPACECRAFT_SOLAR_DISTANCE          = 1.0894e+08

/* SCIENCE OPERATIONS INFORMATION */

VEX:SCIENCE_CASE_ID                = "7"
VEX:SCIENCE_CASE_ID_DESC           = "See information in
                                     DOCUMENT/VEX_SCIENCE_CASE_ID_DESC.TXT"
OBSERVATION_TYPE                   = AD006A
^OBSERVATION_TYPE_DESC             = "OBSERVATION_TYPE_DESC.TXT"

/* INSTRUMENT INFORMATION */

EXPOSURE_DURATION                  = 1999.87 <ms>
INST_CMPRS_NAME                    = NONE
INST_CMPRS_RATIO                   = 1.0
INST_CMPRS_QUALITY                 = 0
MACROPIXEL_SIZE                    = 1
LINE_FIRST_PIXEL                   = 1
SAMPLE_FIRST_PIXEL                 = 1
DETECTOR_TEMPERATURE               = 9.33334 <degC>

/* RADIOMETRIC DATA INFORMATION */

RADIANCE_OFFSET                    = 0.0 <W*m**-3*sr**-1>
RADIANCE_SCALING_FACTOR            = 913.059 <W*m**-3*sr**-1>

/* DATA OBJECT DEFINITIONS */

OBJECT                             = IMAGE
  INTERCHANGE_FORMAT               = BINARY
  LINES                            = 512
  LINE_SAMPLES                     = 512
  SAMPLE_TYPE                      = MSB_INTEGER
  SAMPLE_BITS                      = 16
  BANDS                            = 1
  BAND_STORAGE_TYPE                = BAND_SEQUENTIAL
  MAXIMUM                          = 7500
  MEAN                             = 3575.06
  MINIMUM                          = 4006
```

```
  STANDARD_DEVIATION              = 3055.8
END_OBJECT                        = IMAGE

/* IMAGE HEADER DATA ELEMENTS */

OBJECT                            = IMAGE_HEADER
 HEADER_TYPE                      = VICAR2
 INTERCHANGE_FORMAT               = ASCII
 BYTES                            = 6144
 ^DESCRIPTION                     = "VICAR2.TXT"
END_OBJECT                        = IMAGE_HEADER
END
```

Bibliography

[1] Kevin H Baines et al. “The Atmospheres of the Terrestrial Planets: Clues to the Origins and Early Evolution of Venus, Earth, and Mars”. In: *Comparative Climatology of Terrestrial Planets*. Ed. by Stephen J. Mackwell et al. Vol. 1. Tucson: Univ. of Arizona Press, 2013, pp. 137–160.

[2] A. T. Basilevsky et al. “Geologic interpretation of the near-infrared images of the surface taken by the Venus Monitoring Camera, Venus Express”. In: *Icarus* 217.2 (2012), pp. 434–450. ISSN: 0019-1035. DOI: 10.1016/j.icarus.2011.11.003. URL: http://www.sciencedirect.com/science/article/pii/S0019103511004222.

[3] A. T. Basilevsky et al. “Possible Felsic Summit of Tuulikki Mons, Venus: Evidence from 1-Micron Surface Emissivity and Magellan-Viewed Morphology”. In: (The Woodlands, USA, Mar. 19–23, 2012). Vol. 43. #1092. 2012.

[4] A.T. Basilevsky et al. “Venus crater-related radar-dark parabolas and neighboring terrains: A comparison of 1-μm emissivity and microwave properties”. In: *Icarus* (2019). ISSN: 0019-1035. DOI: 10.1016/j.icarus.2019.01.009. URL: http://www.sciencedirect.com/science/article/pii/S0019103518302203.

[5] Björn Fiethe. *Venus Monitoring Camera Flight User Manual*. VMC-IDA-MA-SF000-001_1. May 2004.

[6] P. G. Ford and G. H. Pettengill. “Venus topography and kilometer-scale slopes”. In: 97.E8 (1992), pp. 13103–13114. ISSN: 0148-0227. DOI: 10.1029/92JE01085.

[7] *Guest Storage Facility*. URL: https://www.cosmos.esa.int/web/psa/psa_gsf.

[8] G. L. Hashimoto and T. Imamura. “Elucidating the rate of volcanism on Venus: Detection of lava eruptions using near-infrared observations”. In: *Icarus* 154.2 (2001), pp. 239–243. ISSN: 0019-1035.

[9] Rainer Haus and Gabriele Arnold. “Radiative transfer in the atmosphere of Venus and application to surface emissivity retrieval from VIRTIS/VEX measurements”. In: 58.12 (2010), pp. 1578–1598. ISSN: 0032-0633. DOI: 10.1016/j.pss.2010.08.001. URL: http://www.sciencedirect.com/science/article/B6V6T-50PJWX8-2/2/5368f341d2146ba3%2019c711ab0131e651.

[10] D. Heather, A. Venet, and Vazquez J. *Planetary Science Archive PVV User Manual*. SOP-RSSD-UM-004. Oct. 2004.

[11] N. I. Ignatiev et al. “Altimetry of the Venus cloud tops from the Venus Express observations”. In: 114.E9 (2009), E00B43. ISSN: 0148-0227.

[12] Nikolay I. Ignatiev. *VMC in-flight calibration report*. Tech. rep. Max Planck Institute for Solar System Research, 2008.

[13] Nikolay I. Ignatiev. *VMC in-flight calibration report*. Tech. rep. Max Planck Institute for Solar System Research, Nov. 2012.

[14] Mikhail A. Ivanov and James W. Head. “Global geological map of Venus”. In: 59.13 (2011), pp. 1559–1600. ISSN: 0032-0633. DOI: 10.1016/j.pss.2011.07.008. URL: http://www.sciencedirect.com/science/article/pii/S0032063311002297.

[15] W. J. Markiewicz et al. “Venus Monitoring Camera for Venus Express”. In: 55.12 (2007). The Planet Venus and the Venus Express Mission, Part 2, pp. 1701–1711. ISSN: 0032-0633. DOI: 10.1016/j.pss.2007.01.004. URL: http://www.sciencedirect.com/science/article/pii/S0032063307000086.

[16] V. S. Meadows and D. Crisp. “Ground-based near-infrared observations of the Venus nightside: The thermal structure and water abundance near the surface”. In: 101.E2 (1996), pp. 4595–4622. ISSN: 0148-0227.

[17] V. I. Moroz. “Estimates of visibility of the surface of Venus from descent probes and balloons”. In: 50.3 (2002), pp. 287–297. ISSN: 0032-0633.

[18] N. Mueller et al. “Venus surface thermal emission at 1 μm in VIRTIS imaging observations: Evidence for variation of crust and mantle differentiation conditions”. In: 113.E5 (2008), E00B17. ISSN: 0148-0227.

[19] *Navigation and Ancillary Information Facility (NAIF)*. URL: http://pds-naif.jpl.nasa.gov/.

[20] *PDS3 Standards Reference*. URL: https://pds.nasa.gov/datastandards/pds3/standards/.

[21] *Planetary Data System Preparation Workbook, Part 1*. Version 3.1. JPL. D-7669, Feb. 1995.

[22] *Planetary Science Data Archive Technical Note – Geometry and Position Information*. SOP-RSSD-TN-010. ESA RSSD Planetary Missions Division. 2004.

[23] *Planetary Science Data Dictionary*. URL: https://pds.nasa.gov/datasearch/subscription-service/SS-20200707.shtml.

[24] T. Roatsch. *Experimenter to (Science) Archive Interface Control Document (EAICD)*. VMC-DLR-TN-002. June 2015. URL: https://archives.esac.esa.int/psa/ftp/VENUS-EXPRESS/VMC/VEX-V-VMC-3-RDR-V3.0/DOCUMENT/VMC_EAICD.PDF.

[25] T. Roatsch. *Venus Express - VMC Level-1 Product Description*. VMC-DLR-TN-002. Feb. 2006.

[26] T. Roatsch. *Venus Express - VMC Level-2 Product Description*. VMC-DLR-TN-003. Feb. 2006.

[27] T. Roatsch. *Venus Express VMC Data Products Naming Convention*. VMC-DLR-TN-001. Feb. 2006.

[28] A. Seiff. "Thermal structure of the atmosphere of Venus". In: *Venus*. Ed. by D. M. Hunten et al. Vol. 1. Tucson: Univ. of Arizona Press, 1983, pp. 215–279.

[29] A. Seiff et al. "Models of the structure of the atmosphere of Venus from the surface to 100 kilometers altitude". In: 5.11 (1985). Ed. by G.M. Keating A.J. Kilore V.I. Moroz, pp. 3–58. ISSN: 0273-1177. DOI: 10.1016/0273-1177(85)90197-8. URL: http://www.sciencedirect.com/science/article/pii/0273117785901978.

[30] E. Shalygin, O. Shalygina, and A.G. Straume. *VEX-VMC-MPS-NIR2-NS-RCI-EMI_SGMNT-GSF-PUG*. 2025.

[31] E. V. Shalygin et al. "Active volcanism on Venus in the Ganiki Chasma rift zone". In: 42.12 (2015), pp. 4762–4769. ISSN: 1944-8007. DOI: 10.1002/2015GL064088.

[32] E. V. Shalygin et al. "Geologic interpretation of the near-infrared images of area SW of Beta Regio taken by the Venus Monitoring Camera". In: *EGU General Assembly Conference* (Vienna, Austria, May 2–7, 2012). Vol. 14. #6314. 2012.

[33] O. S. Shalygina et al. "Optical properties of the Venus upper clouds from the data obtained by Venus Monitoring Camera on-board the Venus Express". In: 113–114.0 (Aug. 2015), pp. 135–158. ISSN: 0032-0633. DOI: 10.1016/j.pss.2014.11.012. URL: http://www.sciencedirect.com/science/article/pii/S0032063314003481.

[34] K. Stamnes et al. "Numerically stable algorithm for discrete-ordinate-method radiative transfer in multiple scattering and emitting layered media". In: 27.12 (1988), pp. 2502–2509.

[35] H. Svedhem et al. "Venus Express — The first European mission to Venus". In: 55.12 (2007). The Planet Venus and the Venus Express Mission, Part 2, pp. 1636–1652. ISSN: 0032-0633. DOI: 10.1016/j.pss.2007.01.013. URL: http://www.sciencedirect.com/science/article/pii/S0032063307000050.

[36] *The VICAR Image Processing System*. URL: http://www-mipl.jpl.nasa.gov/external/vicar.html.

[37] Dmitrij V. Titov et al. "Morphology of the cloud tops as observed by the Venus Express Monitoring Camera". In: *Icarus* 217.2 (2012), pp. 682–701. ISSN: 0019–1035. DOI: 10.1016/j.icarus.2011.06.020.

[38] M. G. Tomasko, L. R. Doose, and P. H. Smith. "The absorption of solar energy and the heating rate in the atmosphere of Venus". In: 5.9 (1985), pp. 71–79. ISSN: 0273-1177. DOI: 10.1016/0273-1177(85)90272-8.

[39] *VMC calibration report*. Tech. rep. Version 1/2. VMC-MPAE-RP-SS011-001. Max Planck Institute for Solar System Research, Aug. 4, 2008.

[40] J. Zender. *Planetary Science Archive Experiment Data Release Concept Technical Proposal*. SOP-RSSD-TN-015. Oct. 2004.

[41] J. Zender. *Venus Express Archive Generation, Validation and Transfer Plan*. ESA-VEX-PL- 001. ESA. June 2004.